



TECHNISCHE
UNIVERSITÄT
WIEN
Vienna University of Technology

Unterschrift des Betreuers

DIPLOMARBEIT

Dynamische ^{31}P MR Spektroskopie: Vergleich von verschiedenen Ergometern, magnetischen Feldstärken und Lokalisierungsmethoden

ausgeführt am Atominstitut
der Technischen Universität Wien

in Zusammenarbeit mit der Medizinischen Universität Wien
(Exzellenzzentrum für Hochfeld-Magnetresonanz)

unter der Anleitung von
Prof. DI. Dr. Gerald Badurek und
DI Dr. Ladislav Valkovič als verantwortlich mitwirkenden Universitätsassistenten

durch

Monika Kipfelsberger
Döblinger Hauptstraße 7a/2/51
1190 Wien

Wien, 14.05.2014

Unterschrift der Verfasserin



TECHNISCHE
UNIVERSITÄT
WIEN
Vienna University of Technology

MASTER'S THESIS

**Dynamic ^{31}P MR spectroscopy: Comparison of
different ergometers, magnetic field strengths and
localization methods**

performed at the Institute of Atomic and Subatomic Physics
of the Vienna University of Technology

in cooperation with the Medical University of Vienna
(MR Centre of Excellence)

under the guidance of
Prof. DI. Dr. Gerald Badurek and
DI Dr. Ladislav Valkovič as responsible contributing university assistant

by

Monika Kipfelsberger
Döblinger Hauptstraße 7a/2/51
1190 Wien

Vienna, 14.05.2014

Signature of Author

Erklärung zur Verfassung der Arbeit

Monika Kipfelsberger
Döblinger Hauptstraße 7a/2/51
1190 Wien

Hiermit erkläre ich, dass ich diese Arbeit selbständig verfasst habe, dass ich die verwendeten Quellen und Hilfsmittel vollständig angegeben habe und dass ich die Stellen der Arbeit - einschließlich Tabellen und Abbildungen -, die anderen Werken oder dem Internet im Wortlaut oder dem Sinn nach entnommen sind, auf jeden Fall unter Angabe der Quelle als Entlehnung kenntlich gemacht habe.

Wien, 14.05.2014

Unterschrift Verfasserin

Acknowledgements

I would like to thank my supervisor at the MR Centre of Excellence, PhD. DI Ladislav Valkovič, for his helpfulness whenever I needed support and the perfect organization of the performed studies. Another thank goes to my supervisor Prof. Badurek for his straightforward way of doing. I also want to acknowledge the volunteers of all studies and the financial support in form of a research scholarship funded by the Medical University of Vienna.

For the moral support I would like to thank my parents, my siblings, my boyfriend, his family and my close friends. Last but not least I want to thank especially my parents for the possibility to study in Vienna and for the financial support in all the years of university.

Abstract

Dynamic phosphorus magnetic resonance spectroscopy (^{31}P -MRS) with high temporal resolution enables, through measurement of phosphocreatine (PCr) recovery after exercise, a non-invasive evaluation of mitochondrial capacity of the skeletal muscle *in vivo*. The aim of this master thesis is the comparison of different parameters that can possibly influence the results of ^{31}P -MRS investigation on muscle metabolism. To this end, three independent studies were performed at two MR sites.

First study deals with the impact of ergometer type, coil diameter and magnetic field strength within the same group of subjects. Measurements of the calf muscle exercise in eleven subjects on a 3T MR system with home-made mechanical ergometer and on 3T and 7T MR systems equipped with commercial pneumatic ergometer were performed at three different workloads. Higher magnetic field strength improves the data quality (higher SNR, better fitting accuracy), increasing reliability, but no significant differences were found in the metabolic parameters between magnetic field strengths. In the inter-institution comparison, significant differences were found in the concentration of PCr measured at rest and in the depletion of PCr causing significant difference in mitochondrial capacity (Q_{\max}) at low workload. From this study it can be concluded that metabolic parameters measured by dynamic ^{31}P -MRS do not depend upon used magnetic field strength. However, same workload and same protocols for measurement and evaluation are important for comparison of data acquired with different ergometers, especially when effects of very mild exercise are examined.

Second study is dedicated to evaluate the depth resolved surface coil MRS (DRESS) as a non-echo based localization method for dynamic ^{31}P -MRS at 7T. Two dynamic examinations of plantar flexions at 25% of maximal voluntary contraction, one without spatial localization and one with the DRESS slap positioned obliquely over the gastrocnemius medialis, were conducted in fourteen volunteers. Significant differences in metabolic parameters were found between the non-localized and DRESS localized data. Splitting of the inorganic phosphate (Pi) signal was observed in several non-localized data sets consisting of a mixture of signals from several muscles, but in none of the DRESS-localized data sets. In conclusion, the DRESS localization scheme yields good spatial selection and provides muscle specific insight into oxidative metabolism even at relatively low exercise load.

Third study targeted on the comparison of single voxel localization through slice selective localization by adiabatic selective refocusing (semi-LASER), with DRESS and surface coil localization. Five volunteers performed three dynamic examinations on plantar flexions, one with each localization method, at the same workload. Signal from gastrocnemius medialis acquired by DRESS and semi-LASER localization shows a higher PCr depletion, a trend towards lower τ and lower pH at the end of exercise in comparison to non-localized acquisition. Since the relatively long echo time needed for semi-LASER limits the quantification of J-coupled spin systems (e.g., ATP), a calculation of Q_{\max} is not possible. The results suggest a favored application of semi-LASER than DRESS when higher anatomical and physiological specificity is needed with the advantage of DRESS in calculation of Q_{\max} .

Kurzfassung

Dynamische Phosphor-Magnetresonanzspektroskopie (^{31}P -MRS) mit hoher zeitlicher Auflösung erlaubt einen nicht-invasiven Einblick in die mitochondriale Kapazität von Skelettmuskeln *in vivo* durch Messung der Regeneration von Phosphokreatin (PCr) nach Muskelbetätigung. Das Ziel dieser Diplomarbeit ist der Vergleich verschiedener Parameter, die möglicherweise einen Einfluss auf die mit ^{31}P -MRS gemessenen Ergebnisse von Muskelmetabolismus haben. Zu diesem Zweck wurden drei unabhängige Studien an zwei MR-Forschungsstandorten durchgeführt. Die erste Studie befasst sich mit der Auswirkung von Ergometerart, Spulendurchmesser und magnetischer Feldstärke innerhalb derselben Probandengruppe. Es wurden Messungen des Wadenmuskels mit drei verschiedenen Muskelbelastungen an elf Probanden in einem 3T MR-System mit einem selbstgebauten mechanischen Ergometer und in einem 3T und 7T MR-System mit einem kommerziellen pneumatischen Ergometer durchgeführt. Höhere Magnetfeldstärke verbessert die Datenqualität (größeres SNR, bessere Fitting-Genauigkeit) und daher die Zuverlässigkeit, dennoch wurden keine signifikanten Unterschiede in den metabolischen Parametern zwischen den Magnetfeldstärken festgestellt. Bei dem Vergleich zwischen den Instituten wurden signifikante Unterschiede in der PCr-Konzentration in Ruhe und im Abbau von PCr gefunden. Dies führt zu einem signifikanten Unterschied in mitochondrialer Kapazität (Q_{\max}) bei niedriger Muskelbelastung. Aus dieser Studie kann geschlussfolgert werden, dass metabolische Parameter gemessen mit ^{31}P -MRS nicht von der Magnetfeldstärke abhängen. Jedoch ist es für den Vergleich von Daten, die mit verschiedenen Ergometern aufgenommen wurden, wichtig, gleiche Muskelbelastung und gleiches Mess- und Auswertungsprotokoll zu verwenden. Dies gilt besonders bei der Untersuchung von Ergebnissen mit sehr niedriger Muskelbelastung.

Die zweite Studie widmet sich der Bewertung von DRESS (depth resolved surface coil MRS) bei 7T als eine Lokalisierungsmethode für dynamische ^{31}P -MRS, die nicht echo-basiert ist. Es wurden zwei dynamische Messungen von Plantarflexionen (eine nicht örtliche und eine mit schief über Gastrocnemius Medialis positionierten DRESS-Streifen lokalisierte Messung) bei vierzehn Probanden mit 25% der maximal erreichbaren Kontraktion durchgeführt. Signifikante Unterschiede in den metabolischen Parametern zwischen nicht-lokalisierten und DRESS-lokalisierten Daten wurden gefunden. Eine Aufspaltung des Phosphatsignals (Pi) wurde in mehreren nicht-lokalisierten Datensätzen beobachtet, jedoch in keinen der DRESS-lokalisierten Datensätzen. Schlussendlich erbringt die DRESS-Lokalisierungsmethode eine gute örtliche Markierung und liefert muskelspezifischen Einblick in den oxidativen Metabolismus sogar bei relativ niedriger Muskelbelastung.

Die dritte Studie visiert den Vergleich von Lokalisierung durch ein Volumenelement (Voxel) durch „slice selective localization by adiabatic selective refocusing“ (semi-LASER) mit DRESS- und Oberflächenspulenlokalisierung an. Fünf Probanden führten drei dynamische Messungen von Plantarflexion, je eine pro Lokalisierungsmethode, mit der gleichen Muskelbelastung durch. Das Signal von Gastrocnemius Medialis erhalten durch DRESS- und semi-LASER-Lokalisierung zeigt einen größeren Abbau von PCr und einen Trend zu kleineren τ und kleineren pH am Ende der Muskelbetätigung im Vergleich zur nicht-lokalisierten Erfassung. Aufgrund der relativ langen Echozeit von semi-LASER ist die Quantifizierung von J-gekoppelten Spinsystem (z.B. ATP) begrenzt und daher eine Berechnung von Q_{\max} nicht möglich. Die Ergebnisse empfehlen eine bevorzugte Anwendung von semi-LASER bei dem Bedarf von hoher anatomischer und physiologischer Spezifität, DRESS hat jedoch den Vorteil von möglicher Q_{\max} -Berechnung.

List of used symbols, parameters and abbreviations

1D-ISIS	one-dimensional image-selected in vivo spectroscopy
ADP	adenosine diphosphate
AFP	adiabtic full passage
AMARES	advanced method for accurate, robust and efficient spectral fitting
ATP	adenosine triphosphate
B₀	static magnetic field
B₁	magnetic field perpendicular to B ₀
BIR	<i>B</i> ₁ -independent rotation
BMI	body mass index
BOLD	blood oxygenated-level dependent
CK	creatine-kinase
Cr	Creatine
CRLB	Cramér-Rao lower bounds
CSA	chemical shift anisotropy
CSDE	chemical shift displacement error
CSI	chemical shift imaging
¹³C	carbon-13
δ	chemical shift
DRESS	Depth-Resolved Surface Coil Spectroscopy
ΔE	the energy difference between two energy states
FID	free induction decay
fMRI	functional magnetic resonance imaging
FWHM	full width at half maximum
γ	gyromagnetic ratio
GABA	gamma-aminobutyric acid
GPC	glycerophosphocholine
GPE	glycerophosphoethanolamine
HF	high frequency
¹H	hydrogen
LASER	localization by adiabatic refocusing
M₀	macroscopic magnetization

MR	magnetic resonance
MRI	magnetic resonance imaging
NMR	nuclear magnetic resonance
MRS	magnetic resonance spectroscopy
MRSI	magnetic resonance spectroscopy imaging
MRT	magnetic resonance tomography
MVC	maximum voluntary contraction
ν	Larmor frequency
NAD	adenine dinucleotide
NADP	nicotinamide adenine dinucleotide phosphate
non-loc	surface coil localization
NTP	nucleotide triphosphate
³¹P-MRS	phosphorus magnetic resonance spectroscopy
³¹P	phosphorus
PCr	phosphocreatine
PDE	phosphodiester
Pi	inorganic phosphate
PME	phosphomonoester
ppm	parts per million
Q_{max}	oxidative capacity/flux
RF	radio frequency
σ	shielding constant
SAR	specific absorption rate
semi-LASER	Slice-Selective Localization by Adiabatic Selective Refocusing
SNR/ut	signal-to-noise ratio per unit
τ	phosphocreatine recovery time constant
TE	echo time
TE*	acquisition delay
TI	inversion time
TR	repetition time
T₁	longitudinal relaxation time
T₂	transverse relaxation time
T₂*	effective transverse relaxation
VOI	voxel of interest
V_{PCr}	initial recovery rate of phosphocreatine

Contents

1	Preface	1
2	Fundamentals of Magnetic Resonance	3
2.1	Classical Description	3
2.2	Quantum Mechanical Description	5
2.3	Macroscopic Magnetization	7
2.4	Excitation and Detection	8
2.5	Bloch Equations	9
2.6	Relaxation Times	12
2.7	RF Pulses	13
2.8	Sequences	15
2.9	Shimming	20
2.10	High Field MR	20
3	Fundamentals of MR-Spectroscopy	23
3.1	Chemical Shift	24
3.2	Spin-spin Coupling	25
3.3	Phosphorus-31 NMR Spectroscopy	28
3.4	Chemical Conversion during Muscle Activation	29
3.5	Dynamic ³¹ Phosphor MRS	31
3.6	Exercise-induced Linewidth Changes in NMR Spectra	32
4	Fundamentals of used Localization Methods	35
4.1	Slice-Selective Localization by Adiabatic Selective Refocusing (semi-LASER)	36
4.2	Depth-resolved Surface Coil Spectroscopy (DRESS) Localization	37
5	Aim of the Thesis	39
6	Methods	41
6.1	Region of Interest: Posterior Leg	41
6.2	Study participants	42
6.3	Used Equipment	42
6.4	Coil map evaluation	43
6.5	Exercise Protocol	44

6.6	NMR Pulse Sequences	45
6.7	Data Postprocessing in jMRUI	47
6.8	Further Calculations	47
7	Results	51
7.1	Comparison between different magnetic field strengths and ergometers at two institutes	51
7.2	Comparison of non-localized vs. DRESS localization method	59
7.3	Comparison of DRESS vs. semi-LASER localization vs. non-localized method	63
8	Discussion	65
8.1	Comparative multicenter study between different magnetic field strengths and ergometers	65
8.2	Comparative study of non-localized vs. DRESS localization method	69
8.3	Comparative study of DRESS vs. semi-LASER localization vs. non-localized method	71
9	Conclusion	75
	Bibliography	77
	List of Figures	84
	List of Tables	88
A	Detailed results - Multicenter Study	91
B	Detailed results - Nonloc/DRESS Study	105
C	Detailed results - DRESS/semi-LASER/nonloc Study	109

Preface

The anatomy of the human body was mostly unknown in the previous history of men before the last century due to religious and moral reasons. Nowadays, it is obvious how the inside of the body looks like due to technical inventions like the computer tomograph, ultrasound or magnetic resonance tomography (MRT). Nuclear magnetic resonance (NMR) technique is one of the most widely used and versatile methods in biological sciences. Milestones of the MRT was the mathematical background found by Jean-Baptiste Fourier (~1800), the work with magnetic fields done by Nikola Tesla (~1900), the physical discovery of the nuclear spin by Felix Bloch and Edward Purcell (1946) and finally the technical realization of the MRT by Paul Lauterbur (1973).

Magnetic resonance imaging (MRI) is the most prominent section concerning MRT in clinical praxis, but magnetic resonance spectroscopy (MRS) is another useful application of MR, which can identify and quantify metabolites inside the body. Next to the most common hydrogen proton MRS, phosphor nuclei can also be chosen for MRS. Dynamic phosphorus MR-spectroscopic (^{31}P -MRS) examinations during muscle exercise allow non invasive assessment of changes in the concentrations of phosphocreatine (PCr) and inorganic phosphate (Pi), which are associated with the energy consumption in muscle. Different pathological conditions, e.g. insulin resistance [1], peripheral artery disease [2] [3] or neuromuscular disorders, different medication, e.g. long-term zidovudine therapy for HIV patients, as well as training may alter the mitochondrial content in the muscle responsible for energy consumption. ^{31}P -MRS may also be used for evaluation of fiber type composition in the human muscle, adenosine triphosphate (ATP) turnover during muscle contraction and determination of intracellular pH [4].

In this master thesis, a bi-centric study was performed to assess the impact of different equipment used on the muscle metabolic parameters measured by dynamic ^{31}P -MRS within the same group of subjects. Second and third study deals with the comparison of different localization methods at ultra-high field MR (i.e., 7T). Each method proposed in this thesis was carefully planned, prepared and tested *in vivo* on healthy volunteers and the obtained spectra were evaluated and interpreted. Clinical relevance of these studies was demonstrated through performed tests and literature referencing.

Fundamentals of Magnetic Resonance

NMR is the study of the magnetic properties and energies of nuclei. When nuclei are placed in a strong external magnetic field, absorption and emission of electromagnetic radiation can be observed. MRI holds a great relevance and potential for clinical and research purposes due to the ability to noninvasively display high-resolution anatomy images. Its versatility and accuracy in soft tissue imaging is unmatched by any other individual imaging modality and therefore MRI is very sensitive to certain pathologies. NMR is based on the concept of nuclear spin. Every nuclei possesses a spin, that implies the nuclei is spinning around itself. [5] [6] [7] [8]

2.1 Classical Description

Before going into details of quantum physics some relations from classical physics will be introduced which will simplify further explanations. “Although classical physics is incapable of describing the quantum mechanical spin, it can be used to create a familiar frame of reference in which the existence of a spin angular momentum can be visualized.” [5]

Linear or rotational motion of an object of mass m and velocity v has a corresponding linear or rotational momentum p :

$$\mathbf{p} = m\mathbf{v} \quad (2.1)$$

Momentum can be seen as the tendency for an object to continue its motion. The momentum only changes when a force \mathbf{F}

$$\mathbf{F} = \left(\frac{d\mathbf{p}}{dt} \right) = m\mathbf{a} \quad (2.2)$$

is applied (according to Newton’s second law; \mathbf{a} = acceleration).

During a rotational motion, consider the object moving with a constant velocity about a fixed

point at a distance r . This motion can be described with an angular momentum vector:

$$\mathbf{L} = \mathbf{r} \times \mathbf{p} \quad (2.3)$$

The magnitude of \mathbf{L} is mvr and its direction is perpendicular to the plane of motion. Angular momentum can be changed when an external torque is applied (analogy: linear momentum can be changed with force). The external torque \mathbf{T} (or rotational force) is defined as:

$$\mathbf{T} = \mathbf{r} \times \mathbf{F} = \mathbf{r} \times \left(\frac{d\mathbf{p}}{dt} \right) = \left(\frac{d\mathbf{L}}{dt} \right) \quad (2.4)$$

where r is the distance over which the force has to be delivered.

When the object carries an electrical charge, a current loop occurs and therefore a magnetic field is generated, which is characterized by the magnetic dipole moment $\boldsymbol{\mu}$, which is defined in general as current times area. For an object with mass m and charge e rotating at constant rotational velocity v about a fixed point at distance r , the magnetic moment $\boldsymbol{\mu}$ results in:

$$\boldsymbol{\mu} = \left[\frac{ev}{2\pi r} \right] \pi r^2 \quad (2.5)$$

With $\mathbf{L} = m\mathbf{v}r$, a fundamental relation between magnetic moment and angular moment can be obtained:

$$\boldsymbol{\mu} = \left(\frac{e}{2m} \right) \mathbf{L} = \gamma \mathbf{L} \quad (2.6)$$

where γ is the (classical) gyromagnetic ratio. When the rotating object is located in an external magnetic field \mathbf{B}_0 , the loop will feel a torque given by:

$$\mathbf{T} = \boldsymbol{\mu} \times \mathbf{B}_0 \quad (2.7)$$

Combining equations 2.4, 2.6 and 2.7 results in:

$$\left(\frac{d\boldsymbol{\mu}}{dt} \right) = \gamma \boldsymbol{\mu} \times \mathbf{B}_0 \quad (2.8)$$

Since the amplitude of $\boldsymbol{\mu}$ is constant, the differential equation in formula 2.8 reveals the fact that $\boldsymbol{\mu}$ changes its orientation relative to \mathbf{B}_0 , i.e. $\boldsymbol{\mu}$ rotates (precesses) about \mathbf{B}_0 . The interaction with an external magnetic field is called Zeeman interaction. The precession of $\boldsymbol{\mu}$ about \mathbf{B}_0 can be described by:

$$\left(\frac{d\boldsymbol{\mu}}{dt} \right) = \boldsymbol{\mu} \times \boldsymbol{\omega}_0 \quad (2.9)$$

Looking at equations 2.8 and 2.9, the Larmor frequency results:

$$\boldsymbol{\omega}_0 = \gamma \mathbf{B}_0 \quad (2.10)$$

or

$$\nu_0 = \left(\frac{\omega_0}{2\pi} \right) = \left(\frac{\gamma}{2\pi} \right) B_0 \quad (2.11)$$

The spin of a nuclei can be visualized as a spinning top with the exception that a spinning top decelerates and stops when no energy is given to it. The spin of a nuclei never stops. When an external force is applied on the spinning top (e.g., gravitation force) and tries to change the position of the rotation axis, there is an evasive movement of the spinning top, the so called precession movement. The same happens to the spin when placed into the external magnetic field \mathbf{B}_0 . The magnetic field \mathbf{B}_0 acts like the external force and because of \mathbf{B}_0 all spins are oriented along the magnetic field performing a precession movement. The precession movement occurs with the Larmor frequency ω_0 (e.g. hydrogen protons in 1.5 Tesla: $\omega_0 = 63.9$ MHz; hydrogen protons in terrestrial magnetic field: $\omega_0 \approx 1$ kHz). [5] [9]

“A magnetic moment in an external magnetic field also has an associated magnetic energy defined as:

$$E = -\boldsymbol{\mu} \cdot \mathbf{B}_0 = -\mu B_0 \cos \theta \quad (2.12)$$

where θ is the angle between the magnetic moment $\boldsymbol{\mu}$ and the external magnetic field \mathbf{B}_0 . Equation 2.12 indicates that the magnetic energy is minimized when $\boldsymbol{\mu}$ is parallel with \mathbf{B}_0 ($\theta = 0^\circ$) and maximized when $\boldsymbol{\mu}$ is antiparallel with \mathbf{B}_0 ($\theta = 90^\circ$). According to equation 2.12, the classical magnetic moment may assume any orientation ($0^\circ \leq \theta \leq 180^\circ$), with energy varying between $+\mu B_0$ and $-\mu B_0$.

Therefore, even though classical mechanics can create a familiar picture of the relation between angular momentum, magnetic moment and Larmor frequency, it cannot explain how the general resonance condition for spectroscopy, $\Delta E = h\nu$, relates to the magnetic energy associated with the magnetic moment. A quantum mechanical treatment is necessary to obtain information about the interaction of electromagnetic waves and nuclear spins.“ [5]

2.2 Quantum Mechanical Description

In quantum mechanics the angular momentum of elementary particles is limited to discrete values, i.e. the angular momentum \mathbf{L} is quantized and its amplitude equals:

$$L = \left(\frac{h}{2\pi} \right) \sqrt{I(I+1)} \quad (2.13)$$

where I is the spin quantum number, which can only be integral or half-integral and h is the Planck’s constant. For a full description of \mathbf{L} the direction is also needed. It is specified by a second quantum number m , which can only have certain discrete orientations with respect to a given direction and a maximum amount of $2I + 1$ values ($m = I, I - 1, I - 2, \dots, -I$). The component of angular moment in z direction is:

$$L_z = \frac{h}{2\pi} m \quad (2.14)$$

By analogy with equation 2.7, elementary particles also have a magnetic moment:

$$\boldsymbol{\mu} = \gamma \mathbf{L} \quad (2.15)$$

where γ is again the gyromagnetic ratio. “Since the angular momentum is quantized, the magnetic moment will also be quantized.” [5] The component of the magnetic moment along the longitudinal z axis is given by:

$$\mu_z = \gamma \left(\frac{h}{2\pi} \right) m \quad (2.16)$$

Combining the classical description of the magnetic energy (equation 2.12) with the quantum mechanical formulation of magnetic moment gives:

$$E = -\mu_z B_0 = -\gamma \left(\frac{h}{2\pi} \right) m B_0 \quad (2.17)$$

Since m is a discrete quantum number, the energy levels are therefore also quantized. For a particle with $I = 1/2$ (e.g., hydrogen (^1H) or phosphorus (^{31}P) atom), there are two energy levels ($m = -1/2$ and $m = 1/2$) and following energy difference is resulting (see also figure 2.1):

$$\Delta E = \gamma \left(\frac{h}{2\pi} \right) B_0 = h\nu_0 \quad (2.18)$$

with

$$\nu_0 = \frac{\gamma}{2\pi} B_0 \quad (2.19)$$

With an applied magnetic field perpendicular to μ_z oscillating with a frequency ν_0 and with the energy equal to the magnetic energy given in equation 2.18 the resonance phenomenon in NMR can be achieved. As one can see the formula for the Larmor frequency is the same for the classical and the quantum mechanical calculation (equations 2.11 and 2.19). [5]

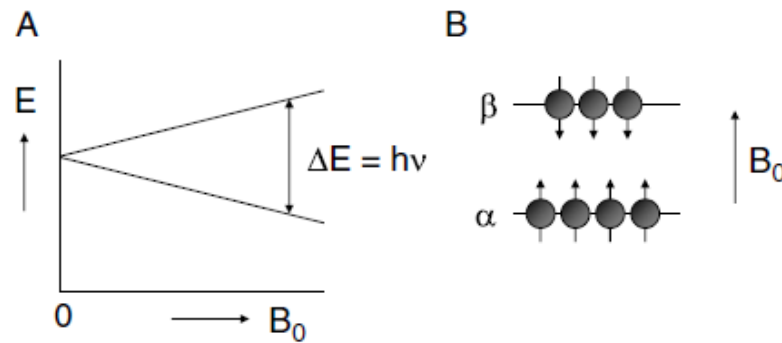


Figure 2.1: (A) The nuclear spin energy for a spin-1/2 nucleus as a function of the external magnetic field strength B_0 . (B) The lower energy level (α spin state) corresponds to magnetic moments parallel with B_0 , while spins in the higher energy level (β spin state) have an antiparallel alignment with B_0 . [5]

2.3 Macroscopic Magnetization

Figure 2.2A shows the precession of a magnetic moment around an external magnetic field in a classical view. Quantization of magnetic moment and magnetic energy can be seen. According to quantum mechanics the angle θ between μ and B_0 is defined as:

$$\cos \theta = \frac{m}{\sqrt{I(I+1)}} \quad (2.20)$$

For a nucleus with a spin $I = 1/2$ and therefore two energy levels $m = \pm 1/2$ there are two different angles $\theta = \pm 54.74^\circ$. These two states are often referred to as α and β spin states.

Considering now a macroscopic sample with many spins, there will be a small difference in the population of these spin states that can be calculated using the Boltzmann equation:

$$\left(\frac{n_\alpha}{n_\beta}\right) = e^{\Delta E/kT} = e^{h\nu/kT} \quad (2.21)$$

where n_α is the number of spins in the α (low energy) state and n_β is the number of spins in the β (high energy) state, k is the Boltzmann constant and T is the absolute temperature. With a simplification ($\frac{h\nu}{kT} \ll 1$) and truncation of a Taylor series it results in:

$$\left(\frac{n_\alpha}{n_\beta}\right) = 1 + \left(\frac{h\nu}{kT}\right) \quad (2.22)$$

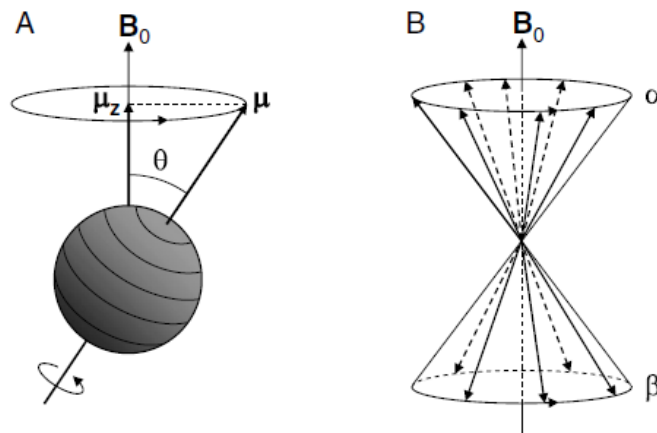


Figure 2.2: (A) A nuclear spin precessing in an external magnetic field B_0 . The spin magnetic moment μ precesses about B_0 , in which the orientation θ and the amplitude (along z) μ_z are quantized. (B) In a macroscopic ensemble of nuclear spin-1/2, the spins distribute themselves among two possible orientations according to the Boltzmann equation. [5]

For a macroscopic sample with one million nuclear spins of ^1H at 37°C ($T = 310.15\text{ K}$) and in a magnetic field of 9.4 T , corresponding to $\nu = 400\text{ MHz}$, the population difference between α and β spin states is only 31 spins ($= 0.0031\%$).

The total net magnetic moment \mathbf{M} (i.e. the magnetization) of a macroscopic sample is the sum over all individual magnetic moments $\boldsymbol{\mu}$. As in figure 2.2B can be seen, there is no net component of \mathbf{M} in the transverse xy plane. However, there is a net component in the z direction due to the population difference. At thermal equilibrium the magnitude of the longitudinal magnetization M_0 is:

$$M_0 = \sum_{i=1}^n \mu_i = n_\alpha \mu_z + n_\beta \mu_z = \gamma \left(\frac{h}{4\pi} \right) (n_\alpha - n_\beta) \quad (2.23)$$

Using $\frac{h\nu}{kT} \ll 1$ and $n = n_\alpha + n_\beta =$ total number of nuclear spins, the population difference ($n_\alpha - n_\beta$) is given by:

$$(n_\alpha - n_\beta) \approx \left(\frac{n h \nu}{2kT} \right) \quad (2.24)$$

The resulting amplitude of the macroscopic magnetization vector at equilibrium is:

$$M_0 = \left(\frac{\gamma h}{2\pi} \right)^2 \left(\frac{n B_0}{4kT} \right) \quad (2.25)$$

From equation 2.25 several features concerning the sensitivity of NMR can be deduced: The macroscopic magnetization M_0 is proportional to the square of the gyromagnetic ratio. Since $\gamma \propto \nu_0$, nuclei resonating with high frequency result in relatively intense NMR signal. Hydrogen has the highest γ of the commonly known nuclei, and has therefore the highest relative intensity. This fact, together with its high abundance make hydrogen the most used nuclei in NMR. Due to the proportionality of M_0 and B_0 there is a trend towards the use of higher magnetic field strengths which now typically range from 1.5 T to 17.5 T (or up to circa 11.7 T for experimental *in vivo* applications). The reverse proportionality of temperature and macroscopic magnetization cannot be used for *in vivo* applications. [5]

2.4 Excitation and Detection

Once placed into strong magnetic field B_0 , a macroscopic magnetization of nuclei is generated. In thermal equilibrium all spins are orientated in accordance with the Boltzmann distribution, therefore, there is no phase coherence in the transverse plane and the net longitudinal magnetization is a static vector. Further interaction can be achieved with an electromagnetic radio frequency pulse (RF-pulse) that rotates the net longitudinal magnetization towards or onto the transverse plane. For the existence of a resonance condition, the frequency of the RF-pulse has to be equal to the Larmor frequency. The pulse oscillating in the RF range (MHz), i.e. $B_{1max} \cos(\omega t)$, is applied for a finite time T and turned off again. During the RF pulse, magnetization will precess about B_0 and B_1 . The initially longitudinal magnetization in the z axis experiences a torque from the applied B_1 field in the xy plane, which results in a rotation of M_0

towards this plane. When the applied B_1 field is long enough, M_0 can be completely excited onto the transverse plane (90° excitation, see figure 2.3A) or even inverted to the $-z$ axis (i.e. 180° inversion RF-pulse). In addition, because of the RF pulse, the spins come into a state of phase coherence giving rise to transversal magnetization - the measurable magnetization. For the sake of completeness it is mentioned that during this excitation process electromagnetic radiation with the Larmor frequency is emitted and can be detected with a coil using Faraday's induction law. [5] [10]

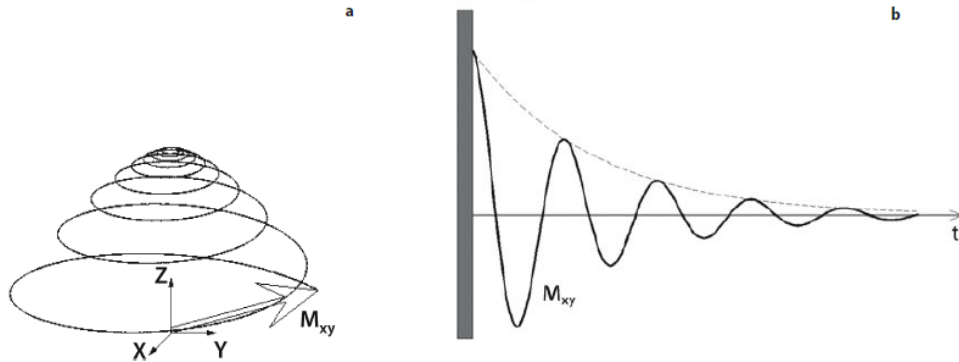


Figure 2.3: (A) After a RF pulse M_0 rotates back in its thermal equilibrium. The magnetization vector can be described by a helix. The transverse component M_{xy} produces measurable electromagnetic radiation. (B) Gray bar represents the RF-pulse; the so generated MR-signal (measurable with a coil perpendicular to the z axis) is called “free induction decay“ (FID) and is an exponential damped oscillation. [10]

2.5 Bloch Equations

Equations 2.4 and 2.7 reveal that a magnetic moment μ placed in a magnetic field B experiences a torque proportional to the time derivative of the angular momentum. Looking at the sum of all magnetic moments, the expression of motion of a single magnetic moment can be generalized for the total magnetization:

$$\frac{d\mathbf{M}(t)}{dt} = \mathbf{M}(t) \times \gamma \mathbf{B}(t) \quad (2.26)$$

where $B(t)$ may include time-varying components additionally to the static magnetic field B_0 . In thermal equilibrium (no time-varying magnetic fields) there are no x and y components but only a constant z component:

$$\frac{dM_z(t)}{dt} = 0 \quad (2.27)$$

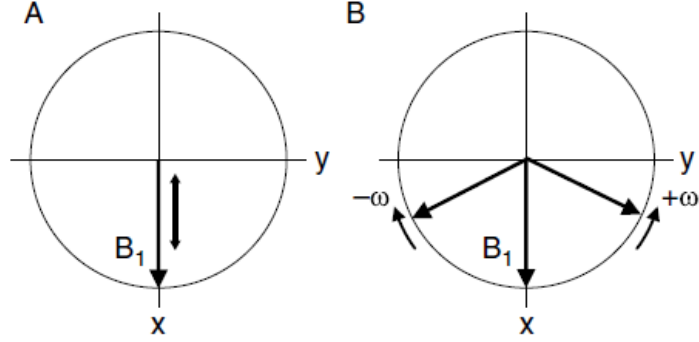


Figure 2.4: Decomposition of a linear oscillating magnetic field (A) into two rotating magnetic fields (B) with frequencies $-\omega$ and ω , respectively. [5]

“The magnetic component of a RF field that is linearly polarized along the x axis in the laboratory frame can be written as:

$$\mathbf{B}_1(t) = 2B_{1max} \cos \omega t [\mathbf{x}] \quad (2.28)$$

where B_{1max} is the maximum amplitude of the applied field, ω is the angular transmitter of carrier frequency on the RF field and $[\mathbf{x}]$ represents a unit vector along the x axis. The linearly polarized field can be decomposed into two circularly polarized fields rotating in opposite direction about the z axis (see figure 2.4) according to:

$$\mathbf{B}_1(t) = B_{1max} (\cos \omega t [\mathbf{x}] + \sin \omega t [\mathbf{y}]) + B_{1max} (\cos \omega t [\mathbf{x}] - \sin \omega t [\mathbf{y}]) \quad (2.29)$$

Only the field rotating in the same sense as the magnetic moment interacts significantly with the magnetic moment. The counter rotating field influences the spins to the order $(B_1/2B_0)^2$, which is typically a very small number known as the Bloch-Siegert shift. Since under most conditions the counter rotating field can be ignored, the linearly polarized RF field (formula 2.29) is then equivalent to a rotating magnetic field given by:

$$\mathbf{B}_{1x}(t) = B_{1max} (\cos \omega t [\mathbf{x}] - \sin \omega t [\mathbf{y}]) = B_{1x} \cos \omega t + B_{1y} \sin \omega t \quad (2.30)$$

A similar expression can be derived for \mathbf{B}_{1y} .“ [5]

Expanding the equation 2.26 for two magnetic fields \mathbf{B}_0 and \mathbf{B}_1 , the Bloch equations in the laboratory frame of reference in the absence of relaxation can be derived as:

$$\frac{dM_x(t)}{dt} = \gamma [M_y(t) B_0 - M_z(t) B_{1y}] \quad (2.31)$$

$$\frac{dM_y(t)}{dt} = \gamma [M_z(t) B_{1x} - M_x(t) B_0] \quad (2.32)$$

$$\frac{dM_z(t)}{dt} = \gamma [M_x(t) B_{1y} - M_y(t) B_{1x}] \quad (2.33)$$

The process of return to thermal equilibrium after a perturbation is called relaxation. The components M_x , M_y and M_z relaxate in an exponential manner:

$$\frac{dM_x(t)}{dt} = -\frac{M_x(t)}{T_2} \quad (2.34)$$

$$\frac{dM_y(t)}{dt} = -\frac{M_y(t)}{T_2} \quad (2.35)$$

$$\frac{dM_z(t)}{dt} = -\frac{M_z(t) - M_0}{T_1} \quad (2.36)$$

A detailed explanation of the relaxation time constants T_1 and T_2 can be found in section 2.6.

Combining equations 2.31- 2.36 yields the complete Bloch equations in the laboratory frame:

$$\frac{dM_x(t)}{dt} = \gamma [M_y(t) B_0 - M_z(t) B_{1y}] - \frac{M_x(t)}{T_2} \quad (2.37)$$

$$\frac{dM_y(t)}{dt} = \gamma [M_z(t) B_{1x} - M_x(t) B_0] - \frac{M_y(t)}{T_2} \quad (2.38)$$

$$\frac{dM_z(t)}{dt} = \gamma [M_x(t) B_{1y} - M_y(t) B_{1x}] - \frac{(M_z(t) - M_0)}{T_1} \quad (2.39)$$

The laboratory frame is a fixed Cartesian frame fixed with respect to the laboratory. More convenient is a frame with a new set of Cartesian axes (x' , y' and z') rotating about the static magnetic field \mathbf{B}_0 with frequency ω . The z and z' axes of the laboratory and rotating frames, respectively, are collinear with \mathbf{B}_0 . The magnetization in the rotating frame is:

$$M'_x = M_x \cos \omega t + M_y \sin \omega t \quad (2.40)$$

$$M'_y = M_y \cos \omega t - M_x \sin \omega t \quad (2.41)$$

$$M'_z = M_z \quad (2.42)$$

As a consequence the Bloch equations in the rotating frame can be calculated using equations 2.37- 2.42 and the definitions of B'_{1x} and B'_{1y} in 2.30.

In a frame rotating with a frequency equal to the frequency of \mathbf{B}_1 , \mathbf{B}_1 appears static. Figure 2.5A depicts the generation of transverse magnetization for $\omega = \omega_0$. The magnetization simply precesses about the applied \mathbf{B}_1 field towards the transverse plane, since the vectors are drawn in the rotation frame of reference. In comparison to figure 2.4, which shows the same situation in the laboratory frame, a rotating frame is much clearer.

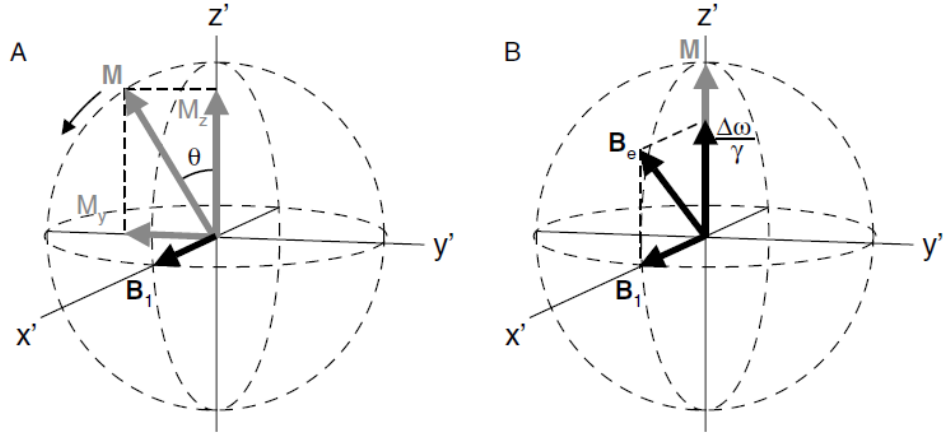


Figure 2.5: Magnetic field vectors encountered in the rotating frame of reference $x'y'z'$ during excitation. (A) On-resonance: The effective, external magnetic field vector equals the magnetic field vector B_1 along x' . The longitudinal magnetization experiences a torque and will rotate towards the transverse plane through an angle θ . (B) Off-resonance: the frequency of the magnetic field B_1 no longer equals the Larmor frequency, resulting in an additional magnetic field vector $\Delta\omega/\gamma$ along z' . The effective magnetic field B_e then equals the vector sum of B_1 and $\Delta\omega/\gamma$. The longitudinal magnetization will experience a torque from this effective field, resulting in a more complex rotation about B_e . [5]

For the case $\omega \neq \omega_0$ the precessional motion of the magnetization ($\omega_0 = -\gamma B_0$) seems to be reduced to a value $\omega_0 - \omega$. It is, therefore, convenient to define an effective magnetic field B_e , which is the vector sum of $(\omega_0 - \omega)/\gamma$ and B_1 , since the magnetization precesses about the effective field. The magnitude of B_e is given by:

$$B_e = |B_e| = \sqrt{B_1^2 + \left(\frac{\omega_0 - \omega}{\gamma}\right)^2} \quad (2.43)$$

On-resonance (i.e. when the frequency of the applied RF pulse ω equals the Larmor frequency ω_0) the equation 2.43 reduces to $B_e = B_1$. In the event of a nonvanishing off-resonance vector (i.e. $\omega \neq \omega_0$), the effective magnetic field B_e is tilted from the transverse plane. The magnetization will precess about B_e , leading to a more complex rotation when compared with the on-resonance situation, as illustrated in figure 2.5B. [5]

2.6 Relaxation Times

The relaxation time constants T_1 and T_2 describe the movability of the molecules in a tissue respectively the quantum mechanics interactions of nuclei with their surrounding.

The longitudinal T_1 relaxation is a process, in which energy is transferred from the spins to the

surrounding 'molecule lattice' (therefore also called spin-lattice relaxation time). T_1 relaxation is the slower relaxation and the T_1 relaxation time declares the time after a RF-pulse in which 63% of longitudinal magnetization M_{z0} in equilibrium has reappeared:

$$M_z(t) = M_{z0} \left(1 - e^{-\frac{t}{T_1}}\right) \quad (2.44)$$

After three T_1 times already 95% of M_{z0} is reached.

The transverse T_2 relaxation is an entropy-process, since spins exchange energy between themselves (no net energy transfer) causing a decrease in phase coherence, i.e. an increase in global chaos or entropy (therefore also called spin-spin relaxation time). T_2 is the faster relaxation and the T_2 relaxation time declares the time after a RF-pulse, in which 37% of transverse magnetization M_{T0} (at the time of excitation) is still existing:

$$M_T(t) = M_{T0} \cdot e^{-\frac{t}{T_2}} \quad (2.45)$$

After three T_2 times only 5% of M_{T0} still exists.

Dephasing of the spins in the xy plane is also caused by a different reason: For a synchronized precession, i.e. Larmor frequency of all spins are equal, an absolutely homogenous magnetic field B_0 would be necessary. This is not possible due to the technical limitations of constructed tomographs with magnetic fields in this order of strength as well as the magnetic properties of the examined sample. The sample is responsible for local magnetic field changes, that are especially high in the regions where the magnetic properties change, e.g., in tissue border areas. In these regions the spins dephase faster than in other regions; the time constant of the exponential signal decrease is called T_2^* or "effective transverse relaxation rate" and typically takes from 10 to 100 ms in human tissue in clinical MRI scanners (1.5 T). [5] [10] [11] [12] [13]

2.7 RF Pulses

There are three basic types of RF pulses: excitation pulses, inversion pulses and refocusing pulses.

An excitation pulse tips the magnetization vector away from the direction of the main magnetic field B_0 . As described in chapter 2.4 magnetization aligned only with B_0 does not create any MR signal, since there exists no transversal component of magnetization. The standard excitation pulse is implemented by switching on (i.e., pulsing) the RF field modulation envelope, denoted by B_1 , for a short time. This range is short enough so that T_1 and T_2 relaxation during the pulse typically can be neglected.

Excitation pulses are characterized by their flip angle, the angle between the direction of the main magnetic field, and the magnetization vector immediately after the excitation pulse is terminated (for more detailed information about flip angle see chapter 2.8). Standard RF pulses obey following relationship between B_1 and the flip angle:

$$\theta = \gamma \int_0^T B_1(t) dt \quad (2.46)$$

where T is the pulse width and γ is the gyromagnetic ratio.

Typically a flip angle θ in the range of $5\text{-}70^\circ$ is used for gradient echo pulse sequences and a flip angle of $\theta = 90^\circ$ is set in spin echo pulse sequences (see chapter 2.8). Slice-selective excitation pulses consist of a slice-selection gradient¹ to produce an excited section, or slice of magnetization. The flip angle can vary across the selected slice, which results in a distribution of transverse magnetization when plotted versus either position or frequency. This distribution is called the slice-selective profile. An ideal slice profile consists of a uniform flip angle within the desired slice and a flip angle of $\theta = 0^\circ$ outside, but the ideal slice profile cannot be achieved in practice because it requires an excitation pulse of infinite duration.

Inversion pulses nutate the magnetization vector from the direction of the magnetic field B_0 to the negative B_0 direction. Although an inversion pulse rotates the magnetization vector by 180° , the flip angle can be slightly larger or smaller either by design or due to system imperfections. A non- 180° pulse can still function as an inversion pulse, as long as the z-component of the magnetization vector is negative at the end of the pulse. The selectivity of an inversion pulse is determined by both its pulse width and pulse shape. Inversion pulses with amplitude modulated pulses are usually frequency selective, whereas pulses with constant RF amplitude (i.e., rectangular pulses) are typically nonselective.

A refocusing pulse rotates dispersing spin isochromats about an axis in the transverse plane to achieve a rephasing (or refocusing) of the magnetization vectors at a later time. The refocused magnetization is known as spin echo (for more detailed explanation of phase dispersion and spin echo see chapter 2.8). Refocusing RF pulses commonly have a flip angle of $\theta = 180^\circ$, where the transverse magnetization is optimally refocused and the largest spin echo signal is produced. [14]

Adiabatic pulses are a special kind of RF pulses that can excite, refocus or invert magnetization vectors uniformly, even in the presence of a spatially nonuniform B_1 field. Unlike nonadiabatic RF pulses, adiabatic pulses do not obey the conventional relationship between the flip angle and the B_1 field amplitude (equation 2.46).

Instead, the flip angle of an adiabatic pulse depends on how the B_1 field varies its amplitude as well as modulation frequency (or the phase) during the pulse. By properly manipulating the modulation functions, spins that experience different B_1 fields can be excited with the same flip angle, as long as the amplitude of the B_1 modulation envelope exceeds a certain threshold. This property gives adiabatic pulses their excellent robustness to variations in B_1 field. [14]

In nonadiabatic RF pulses, the full band of spectral frequencies is excited simultaneously in a static B_0 field with the use of a pulsed B_1 field, where typically the carrier frequency of the pulse remains constant and is applied at the center of the spectral region of interest. Adiabatic pulses are pulses with variation of the carrier frequency with time during the pulse. [15]

The original meaning of an adiabatic process contains no input or output of heat within a system. Transformed to MR pulses, an adiabatic process is the fast frequency sweep in the resonance frequency region, resulting in a negligence of relaxation phenomena. „In analogy to the classical

¹The gradient is an additional magnetic field to B_0 with the same direction which is a spatial linearly varying weak magnetic field that is superimposed to the static temporal and spatial strong magnetic field of B_0 . Through this additional magnetic field a separation of the Larmor-frequencies of the hydrogen protons depending on its position can be accomplished. [10] [12]

continuous wave experiment, the different spectral components are rotated in succession during the adiabatic frequency sweep. When the total sweep time is short relative to T_1 , the transient response of the spin system can be induced, which allows observation of NMR phenomena (e.g. FIDs or echos) related to the pulsed method. In a sweep of either B_0 (classical experiment) or RF pulse frequency (adiabatic experiment) from one side of resonance to the other, the net rotation of the magnetization vector \mathbf{M} is highly insensitive to changes in B_1 amplitude. This desirable property has led to the common use of adiabatic pulses in NMR experiments performed with surface coils.

Across the spectral bandwidth of interest, spins with different precession frequencies (isochromats) are sequentially rotated as the frequency sweep $\omega_{RF}(t)$ approaches the resonance frequency ω_0 of each isochromat. With some types of adiabatic pulse, such as adiabatic full passage (AFP, see figure 4.2), the bandwidth $\Delta\Omega$ is dictated solely by the range of the frequency sweep. For the spins precessing within this frequency band, the flip angle will be uniform, provided that the orientation of the effective magnetic field changes slower than the rotation of \mathbf{M} about this effective field. This requirement, which is known as the adiabatic condition, can be satisfied by using a sufficiently high B_1 amplitude or by a slow frequency sweep. With the latter method, $\Delta\Omega$ can be arbitrarily wide, even when using low peak RF power, provided that the pulse length T_p can be sufficiently long. The ability to achieve uniform flip angles over broad bandwidths with low B_1 amplitude is a unique feature of these adiabatic pulses. With conventional constant-frequency pulses, $\Delta\Omega$ is always inversely proportional to T_p , whereas $\Delta\Omega$ and T_p are independent parameters in certain types of adiabatic pulses. The ability to invert magnetization uniformly across wide bandwidths with arbitrarily low B_1 amplitude has led to a major advance in broadband decoupling with minimal sample heating in high resolution NMR applications. With these broadband pulses, *in vivo* NMR can also benefit from reduced peak RF power requirements and the ability to minimize voxel displacement for different chemical shifts.“ [15]

2.8 Sequences

A pulse sequence is a preselected set of defined simple or complex RF and gradient pulses, that is usually repeated many times during a scan. The time interval between the pulses and the amplitude and shape of the gradient waveforms will control NMR signal reception and affect the characteristics of the MR images. Differences in T_1 , T_2 and proton density (i.e., the number of ^1H nuclei) in various tissues create differences in tissue image contrast. Two key parameters - repetition time (TR) and echo time (TE) - are key to the weighting of the acquired MR signal on relaxation times and, therefore, creation of the desired image contrast. [16] [17]

TR is the repetition time between two RF pulses. If the TR is too short, the magnetization can relax back only partially and the generated MR-signal is smaller [10]. A 90° pulse reduces the longitudinal magnetization to zero, after which it is allowed to recover through T_1 relaxation according to equation 2.44 to $M_z(TR) = M_{z0}$ for $TR > 5T_1$. The amplitude of the transverse magnetization is $M_{xy} = M_z \sin \alpha = M_0$. Even though there is a full excitation, the experiment is not optimal in terms of signal per unit of time, because the majority of scan time is used to wait for recovery of the longitudinal magnetization.

Another solution is the excitation with smaller flip angle and shorter TR to improve the signal-

to-noise ratio per unit of time (SNR/ut). The optimal nutation angle (known as Ernst angle) for maximum signal per unit time is given by:

$$\alpha_{opt} = \arccos \left(e^{-\frac{TR}{T_1}} \right) \quad (2.47)$$

But theoretical calculations and phantom measurements according to Chmelik et al. [18] showed that, if the Ernst angle condition is fulfilled, the SNR/ut is improved only by approximately 10% whereas the setup preparations needed to find and define the amplitude for such angle take additional time. Chmelik et al. also showed that SNR/ut is optimal for $TR = 1.2 T_1$ with a 90° pulse.

The relation 2.47 is illustrated in figure 2.6. With long TR, the exponential term vanishes and the optimal flip angle is 90° . On the other hand, with shorter TR, the nutation angle gets smaller in order to reduce the saturation of longitudinal magnetization and to maximize the acquired signal. The reduced saturated longitudinal magnetization is then available for the next excitation even when TR is very short. [5]

There are three basic sequences: the inversion recovery, the spin echo and the gradient echo sequence [9]. Modifications of these sequences and new approaches using the principles of these sequences are the majority of all sequences used in NMR. In this chapter, the inversion recovery and the spin echo sequence are explained in more detail:

The inversion recovery sequence is the 'gold-standard' for determination of T_1 relaxation times. It consists of two pulses and two delays. After a long TR for full signal recovery, an inversion pulse (180°) inverts the longitudinal magnetization from $+z'$ axis to $-z'$ axis. The magnetization can only partially recover during an inversion recovery delay time (called inversion time TI), before it is excited onto the transverse plane by a 90° excitation pulse. After the signal acquisition, the sequence can be repeated, starting with recovery of longitudinal magnetization during the repetition time TR.

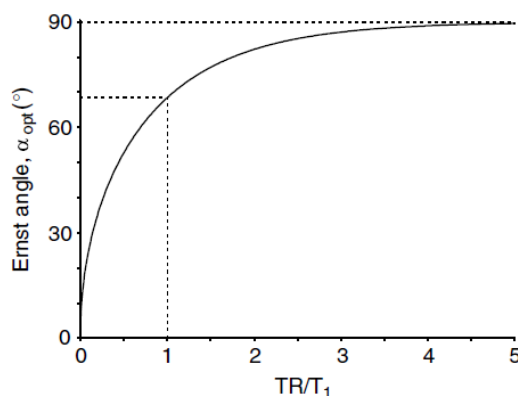


Figure 2.6: Relation between optimal Ernst angle (in degrees) and the ratio of repetition time TR to the T_1 relaxation time. [5]

“The signal intensity $M_z(t)$ during the recovery period t following the 180° inversion pulse can be described by:

$$M_z(t) = M_0 - (M_0 - M_z(0)) e^{-\frac{t}{T_1}} \quad (2.48)$$

where $M_z(0)$ is the longitudinal magnetization at $t = 0$, immediately following the inversion pulse.“ [5] For a perfect inversion pulse $M_z(0) = -M_0$ is valid. T_1 can be obtained by acquiring NMR spectra or images at different TI between 0 and $5T_1$. If $TI = 0$, the longitudinal magnetization is fully excited to the $-y'$ axis by a 90° pulse along the $-x'$ axis since the longitudinal magnetization could not recover at all. On the other hand, for $t = 5T_1$, the longitudinal magnetization can fully recover to the $+z'$ axis before the 90° pulse and therefore the magnetization is fully excited to the $+y'$ axis.

Figure 2.7A illustrates inversion recovery spectra as a function of the recovery time t , figure 2.7B is the estimation of T_1 with the results of Figure 2.7A and equation 2.48. Zero-crossing of the longitudinal magnetization at time t_{null} is given by $T_1 \ln 2$ and can provide a crude estimate of T_1 .

The inversion recovery sequence is the most robust technique for the estimation of T_1 with an inherent insensitivity toward B_0 and B_1 magnetic field inhomogeneities. A disadvantage of this technique is the experimental duration, since it is dictated by the return of thermal equilibrium of magnetization following excitation. Therefore, faster sequences were developed, e.g., the saturation recovery where the 180° is replaced by a 90° pulse. At time $t = 0$ the longitudinal magnetization is zero, irrespective of the signal recovery prior to excitation, therefore saturation recovery does not require a long repetition time and the temporal resolution can be increased. [5] [9]

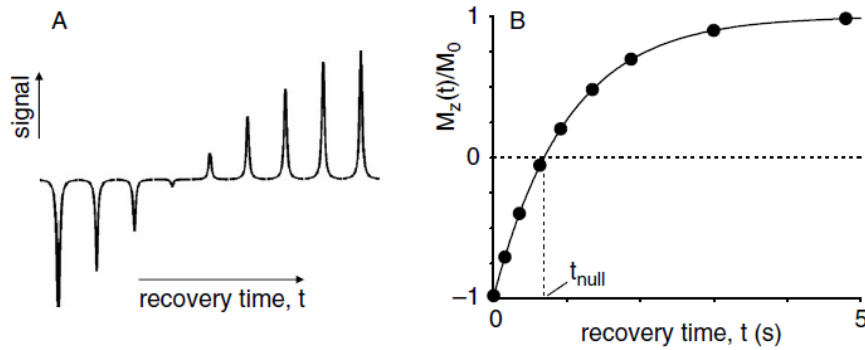


Figure 2.7: Inversion recovery method for determination of T_1 relaxation time: (A) After 180° excitation, longitudinal magnetization relaxes back to its thermal equilibrium value with a T_1 relaxation time constant. Excitation of this signal at different time points results in spectra representing a discrete sampling of the T_1 recovery curve. (B) Fitting of the results of (A) with equation 2.48. Zero-crossing of the longitudinal magnetization at time t_{null} , given by $T_1 \ln 2$, provides a crude estimate of T_1 . [5]

The spin echo sequence deals with phase coherence whose existence is finite due to T_2^* relaxation. The T_2^* relaxation consists of intrinsic T_2 relaxation and dephasing by macroscopic and microscopic magnetic field inhomogeneity. Phase coherence is generated with a RF pulse, but because of T_2^* relaxation, no information about T_2 can be gained directly. However, it is possible to separate the contribution of T_2 and magnetic field inhomogeneity by generating so-called spin-echoes.

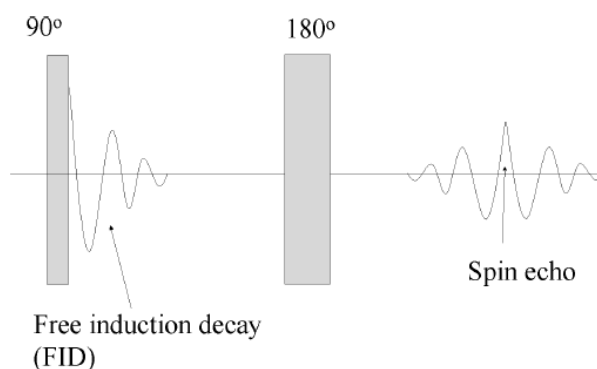


Figure 2.8: The free induction decay occurring after the initial 90° excitation exhibits rapid signal loss via T_2^* dephasing. The 180° pulse leads to a formation of the spin-echo whose amplitude is restored. The amplitude at echo time TE is attenuated by T_2 decay mechanism. [13]

Figure 2.8 shows the simplest sequence called Hahn sequence: The first 90° pulse (irradiated along the $-x'$ axis) excites the longitudinal magnetization from the $+z'$ axis to the y -axis. After this pulse the transverse magnetization vanishes with T_2^* , i.e. magnetization starts losing coherence (the spins dephase), see figure 2.9. This can be described with a visualization: Due to magnetic field inhomogeneities, some spins have a greater Larmor frequency, are „faster“ and, therefore, have covered a greater distance than the “slower“ spins with a smaller Larmor frequency, similar to runners on track, causing differences in the phase based on spatial position and local magnetic field variations. The phase $\phi(\mathbf{r})$ acquired by spins at position \mathbf{r} is given by

$$\phi(\mathbf{r}) = \gamma \Delta B_0(\mathbf{r}) \frac{TE}{2} \quad (2.49)$$

where $\Delta B_0(\mathbf{r})$ represents the magnetic field inhomogeneity between the nominal magnetic field across the entire sample (B_{nom}) and the magnetic field at position \mathbf{r} ($B_0(\mathbf{r})$). After half of the set spin echo time (TE), a second pulse (180° pulse) reverses the direction of all magnetization vectors, leading to a resetting of the acquired phase from $+\phi(\mathbf{r})$ to $-\phi(\mathbf{r})$. Going back to the visualization, after the 180° pulse the “fast“ spins have to cover a bigger distance to come back to the original point, similar to runners with different constant velocities that turn around. Since the magnetic field inhomogeneities have not changed, the frequencies of the spins stay the same, the “fast“ spins catch up with the “slower“ spins (the spins rephase) and at TE after the first RF pulse they are all in phase again and an echo can be detected. The visualization of the runners with different velocities is not fully correct, since the 180° pulse does not change

the orientation of the movement (runners turn around) but changes the orientation of the spins (runners are set to a position where any advance results in a deficit).

The signal decrease observed in the spin-echo sequence is caused exclusively by inherent T_2 relaxation. The spin-echo sequence can be used to measure the T_2 relaxation time by performing several experiments in which the echo time is varied, as illustrated in figure 2.10. The corresponding spectra can be fitted to an exponential curve

$$M_{xy}(TE) = M_{xy}(0) e^{-\frac{TE}{T_2}} \quad (2.50)$$

to obtain the relaxation time constant T_2 . [5] [9] [10] [13]

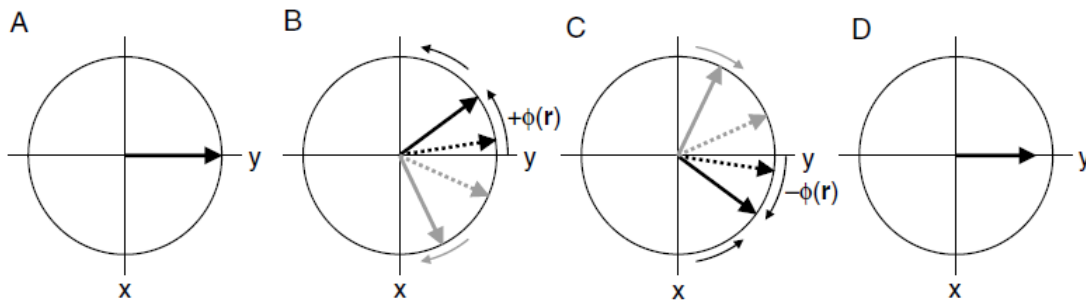


Figure 2.9: (A) After the excitation, (B) the spins dephase in the transverse plane during the first half of TE due to B_0 magnetic field inhomogeneity and frequency offsets. (C) The refocusing 180° pulse mirrors all magnetization vectors along the y axis and the spins rephase during the second half of TE due to the same B_0 magnetic field inhomogeneity and frequency offsets. (D) At the echo time TE the rephasing is complete and a spin-echo is formed. The signal has decayed due to T_2 relaxation. [5]

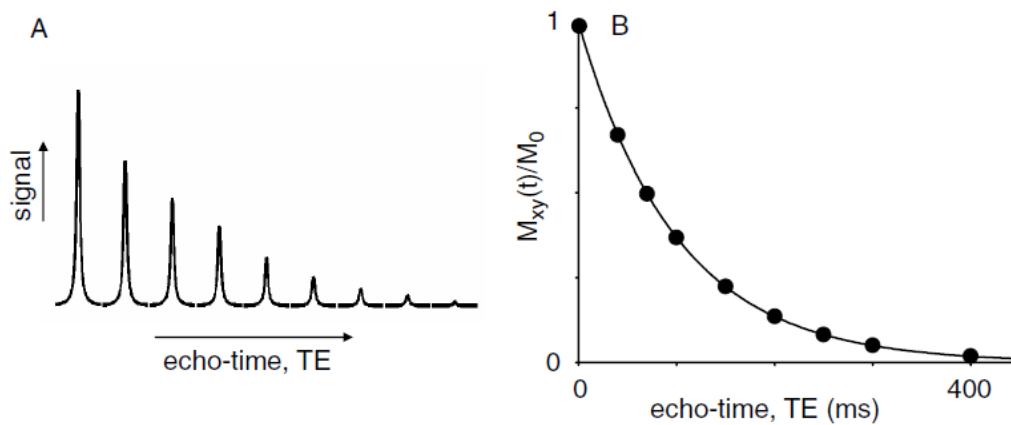


Figure 2.10: Spin echo method for determination of T_2 relaxation: (A) NMR spectra obtained at different echo times. (B) Fitting of the results of (A) with equation 2.50. [5]

2.9 Shimming

The optimization of B_0 field homogeneity is called shimming and is critical to obtain high spectral resolution as well as to avoid image artifacts. Homogeneity of the magnetic field decreases as soon as a sample is placed in the magnetic field due to its magnetic properties. Reduced homogeneity is more pronounced in MRS where it leads to increased linewidth, reduced sensitivity, and consecutively poorer spectral quality. Compensation of these local magnetic field inhomogeneities can be achieved by small adjustments to the static magnetic field by using external shim coils to make the field in the volume of interest as uniform as possible.

The shimming is carried out automatically for MRI, but usually performed manually for MRS. [10] [19]

2.10 High Field MR

Due to the proportionality of M_0 and B_0 (greater number of spins orient along the main axis) as explained in chapter 2.3 there is a trend towards the use of higher magnetic field strengths to gain a more intense NMR signal. However, the increase of magnetic field strength has an impact not just on the signal, but also on the SNR.

Noise of the MR signal can be caused by imperfections of the MR signal (e.g., thermic noise of RF-coils, non-linearity of the signal amplifier), the operation of image processing and movements of the subject (e.g., heart beat, breathing). In general, SNR is depending on slice thickness, bandwidth, field of view, size of image matrix, number of measurements, image parameters (TR, TE, flip angle), magnetic field strength and choice of emitting and receiving coil. The SNR dependence of different factors is given by:

$$SNR \propto \frac{B_1 B_0^2 \sqrt{n}}{\sqrt{4kT \Delta\nu (R_{coil} + R_{sample})}} \quad (2.51)$$

where B_1 is the RF magnetic field, B_0 is the static magnetic field, n is the number of averages, T is the temperature, $\Delta\nu$ is the bandwidth, k is the Boltzmann constant, and R_{coil} and R_{sample} are the coil and sample resistance, respectively. This equation shows that thermal noise at very low magnetic field strength (< 0.3 T) is primarily defined by the resistance of the coil, which is proportional to $\sqrt{B_0}$. Therefore, the overall SNR is proportional to $B_0^{7/4}$. Conversely, as B_0 increases (> 0.3 T), resistance of the sample eventually exceeds that of the coil and from this follows: [9] [20] [21]

$$SNR \propto B_0 \quad (2.52)$$

Besides SNR, increasing magnetic field strength influences also the relaxation times, especially T_1 . It has been shown that „relaxation in ^1H -MRS is dominated by magnetic dipole - dipole interactions. Therefore in ^1H -MRS the T_1 relaxation times are increasing with B_0 . However, for ^{31}P -MRS, both dipolar relaxation and chemical shift anisotropy (CSA) are the two major, competing relaxation mechanisms. In contrast to dipolar interaction, the contributions of CSA to $1/T_1$ and $1/T_2$ relaxation rates are proportional to the gyromagnetic ratio (γ), B_0^2 , the

asymmetry of the magnetic shielding (σ), and the molecular correlation time (τ_C).

CSA contributions can, therefore, be expected to become increasingly important with increasing B_0 . Phantom studies indicate that CSA is the dominant mechanism for nucleotide triphosphate (NTP) at higher B_0 , while dipolar interaction dominates T_1 relaxation at lower fields and for more symmetric molecules such as phosphocreatine (PCr) and inorganic phosphate (Pi).“ [22] Bogner et al. [22] showed that T_1 and T_2 times for ^{31}P metabolites of the human calf muscle decrease with increasing field strength from 3T to 7T.

In addition to the improved SNR and shortened relaxation times in high-field MR, there are additional improvements in ^{31}P -MRS: The linewidth broadening of the phosphate resonance peak in increased field strength is not linearly correlated with the field strength and is smaller than the magnitude of field strength increase. Bogner et al. [22] expected the linewidth to increase with $\approx B_0^2$, but observed an increase from 7 Hz to 11 Hz (or $\approx 72\%$). „Moreover, increasing field strength linearly increases the chemical shift dispersion of *in vivo* ^{31}P -MRS. The combination of these two facts (i.e. large increase in chemical shift dispersion and relatively small increase in linewidth broadening) improves the ^{31}P spectral resolution at 7T.“ [23]

Fundamentals of MR-Spectroscopy

Along with the big development of magnetic resonance imaging in the last two decades, *in vivo* MRS is also becoming an important research tool with clinical applications [24]. MRS offers the unique ability to detect chemical composition and important metabolites noninvasively [9] [19]. In addition to being dependent on physical factors that influence the local magnetic field (see section 2.6), the NMR signal is also dependent on the local chemical environment of the nuclei. In principle, molecules can thus be considered to have a “spectral” signature, with resonances at different frequencies within a few parts per million (ppm) at intensities reflecting the abundance of spins in that environment. [13]

Hydrogen (^1H), also called proton NMR spectroscopy is very prominent, since the hydrogen nucleus is, besides the abundance of the hydrogen isotope tritium, the most sensitive nucleus for NMR in terms of intrinsic NMR sensitivity (high gyromagnetic ratio) and high natural abundance (> 99.9%). Since nearly all metabolites contain hydrogen, *in vivo* ^1H NMR spectroscopy is a powerful technique to observe, identify and quantify a large number of biologically important compounds in tissue. However, the concentration of the metabolites is so small in comparison to the concentration of bulk water, that the signals of metabolites can be neglected in imaging (with the exception of lipid signal from fat tissue). In ^1H MR spectra the signals of metabolites can also only be seen when there is a strong suppression of the water signal. Also other large signals like extracranial lipids can overwhelm small metabolite signals.

Next to hydrogen nuclei (^1H) phosphorus (^{31}P) and carbon-13 (^{13}C) nuclei are commonly used for MRS. “Even though the number of relevant nuclei are limited, each nucleus provides a wealth of information, since a large number of metabolites can be detected simultaneously. ^1H MRS allows the detection of a number of important neurotransmitters, such as glutamate, gamma-aminobutyric acid (GABA) and aspartate and related compounds, like glutamine, as well as the end product of glycolysis, lactate. ^{13}C MRS offers the possibility to study noninvasively the fluxes through important metabolic pathways, like the tricarboxylic acid cycle, *in vivo*. ^{31}P MRS provides information about energetically important metabolites, intracellular pH, magnesium concentration and reaction fluxes.” [5] Since the integrated resonance area is directly proportional to the concentration of the compounds, MRS is a quantitative technique.

This chapter will review different aspects of MRS, like chemical shift, scalar coupling constants and the application of MRS in this master thesis.

3.1 Chemical Shift

When a macroscopic sample contains only one type of nuclear spin, it has one resonance frequency given by the Larmor Equation (equation 2.10). “If the frequency of nuclear spins were solely determined by the resonance condition of this equation, NMR spectroscopy would be of minor importance in chemistry and medicine. Nuclei of the same element (or isotope) even in different molecules would resonate at the same frequency because of their identical gyromagnetic ratio. Fortunately, however, the resonance frequency ω not only depends on the gyromagnetic ratio γ and the external magnetic field B_0 , but is also highly sensitive to the chemical environment of the nucleus under investigation.” [5] This is the so-called chemical shift caused by shielding (screening) of nuclei from the external magnetic field by electrons surrounding them. Electrons will rotate about B_0 in an opposite sense to the proton spin precession. This precession involves motion of charge and therefore there will be an associated magnetic moment μ_e additionally to the nuclear magnetic moment. The electron magnetic moment opposes B_0 and reduces the magnetic field that is effecting the nucleus. The effective magnetic field B at the nucleus is:

$$B = B_0 (1 - \sigma) \quad (3.1)$$

σ is the shielding constant depending on the chemical environment of the nucleus, which is dimensionless and normally expressed in ppm. The equation of the Larmor frequency (equation 2.11) can be modified in the following way:

$$\nu = \frac{\gamma}{2\pi} B_0 (1 - \sigma) \quad (3.2)$$

The frequencies of the metabolite signals are measured in Hertz but expressed in ppm to avoid different values for different magnetic field strengths. An absolute quantification in Hz would be, therefore, less reproducible.

As an example, the difference of frequency between the water (4.7 ppm) and N-Acetylaspartat (2.0 ppm) signal in a magnetic field of 1.5 Tesla can be calculated with:

$$(2.0 \text{ ppm} - 4.7 \text{ ppm}) \cdot 42.58 \text{ MHz/T} \cdot 1.5 \text{ T} = -172 \text{ Hz} \quad (3.3)$$

42.58 MHz/T corresponds to the magnetogyric ratio of the hydrogen nucleus. The N-Acetylaspartat signal is in 1.5 T therefore by a frequency of 172 Hz lower than the water signal. Using a relative comparison with ppm, another signal than the interested one serves as reference signal. By convention the chemical shift is defined as

$$\delta = \frac{\nu - \nu_{ref}}{\nu_{ref}} \cdot 10^6 \quad (3.4)$$

where ν is the frequency of the investigated compound and ν_{ref} the frequency of the reference compound. The reference compound should have a chemical inertness and a chemical

shift that is independent of external variables like shift reagents, temperature or ionic strength. The resonance signal of the reference compound should be well separated from all other resonances. For ^{31}P -MRS PCr is commonly used as reference signal (0.00 ppm).

The recent development and the increasing number of high field MR tomographs is positive for the MRS, since the chemical shift is proportional to the magnetic field strength (see chapter 2.10. Higher magnetic field strength leads to an increased spectral resolution and a sharper edge of the spectral peaks. Therefore clear separation of metabolites, indistinguishable at lower fields is possible. [5] [9]

3.2 Spin-spin Coupling

Additionally to the splitting of the resonance frequency into different frequencies due to chemical shift, in high-resolution MRS the splitting of resonances into several smaller lines can be observed. This phenomenon is referred to as scalar coupling, J coupling or spin-spin coupling. Nuclei with magnetic moments can influence each other besides dipolar coupling (interactions between spins directly through space) also through scalar coupling (interactions between spins through electrons in chemical bonds). In dipolar interactions there is no net interaction between nuclei since rapid molecular tumbling averages the dipolar interactions to zero. However, interactions through chemical bonds do not average to zero.

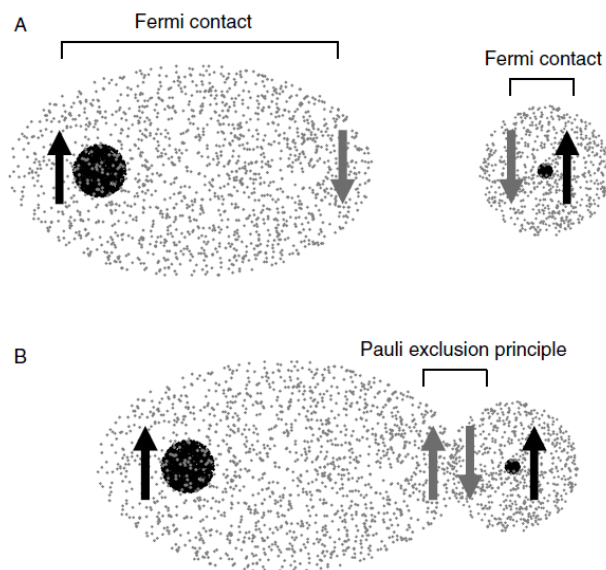


Figure 3.1: Spin-spin interactions involved with scalar coupling. (A) Isolated atoms: The Fermi contact energetically favors antiparallel orientation between nuclear and electronic spins. (B) Chemical bonds: The Pauli principle demands that the electron spin are in an antiparallel orientation thereby potentially forcing nuclear and electron spins in an energetically higher parallel orientation (depending on the nuclear spin state). [5]

In figure 3.1A there is an isolated proton and an isolated carbon-13 atom. „Electrons in s-orbitals have a finite probability of being at the nucleus, giving rise to a hyperfine interaction between nuclear and electronic spins. The Fermi contact governs the interaction between the nuclear and electron spins and (energetically) favors an antiparallel over a parallel arrangement. In terms of energy level diagrams, the two separate (two-level) ^1H and ^{13}C energy level diagrams can be combined into one diagram (figure 3.2A) with four energy levels, corresponding to the four nuclear spin combinations. The four allowed energy level transitions (for which the spin quantum number m changes by ± 1) give rise to two resonance frequencies, ν_H at the proton frequency and ν_C at the carbon-13 frequency.“ [5]

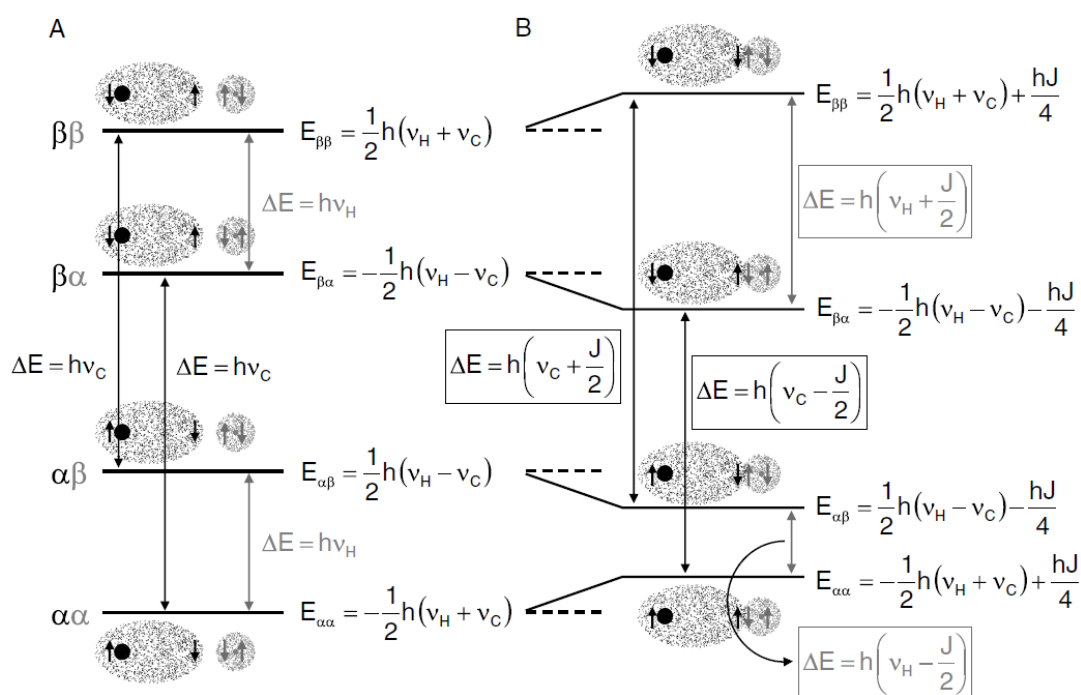


Figure 3.2: (A) Energy level diagram for two isolated carbon-13 and proton nuclei: Two carbon-13 transitions with the same frequency ν_C and two proton transitions with the same frequency ν_H giving rise to singlet resonances in the carbon-13 and proton NMR spectra, respectively. (B) Energy level diagram for a $^{13}\text{C}-^1\text{H}$ 'molecule' with a covalent bond between the carbon-13 and proton nuclei (nuclear spins affect each other through the bonding electrons). The $\alpha\alpha$ and $\beta\beta$ spin state (i.e. the nuclear spin for both ^{13}C and ^1H is in the α and β state, respectively) becomes energetically less favorable as one of the two nuclear-electronic spin orientations is forced to be parallel, whereas in the $\alpha\beta$ and $\beta\alpha$ spin states all spin orientations can be antiparallel. The same energy-level perturbations now give rise to two carbon-13 transitions with different frequencies $\nu_C + J/2$ and $\nu_C - J/2$ and two protons transitions with different frequencies $\nu_H + J/2$ and $\nu_H - J/2$. [5]

When the proton and the carbon-13 nuclei are covalently bound, the Pauli exclusion principle demands that the electron spins are antiparallel. When both nuclear spins are antiparallel to the external magnetic field B_0 (i.e. the high-energy $\beta\beta$ state), the two electrons now cannot be antiparallel to the nuclear spins, leading to an energetically less favorable state (see figure 3.1B). „The $\beta\beta$ energy level increases by an amount proportional to $^1J_{HC}/4$ where $^1J_{HC}$ is the one-bond, heteronuclear scalar coupling constant. Similar arguments can be used to describe the energy increase for the $\alpha\alpha$ state. However for the $\alpha\beta$ and $\beta\alpha$ states the electron spins can be antiparallel to the nuclear spins leading to an energetically more favorable situation. The energy level diagram for a scalar coupled two-spin system still only allows four transitions, but they now correspond to four different frequencies at $\nu_H + ^1J_{HC}/2$ and $\nu_H - ^1J_{HC}/2$ on the proton channel and at $\nu_C + ^1J_{HC}/2$ and $\nu_C - ^1J_{HC}/2$ on the carbon-13 channel (see figure 3.2B). Each of the resonances has been divided into two new resonances of equal intensity separated by $^1J_{CH}$, giving rise to the MR spectrum shown in figure 3.3. Similar arguments can be used to explain scalar coupling over two or three chemical bonds. While scalar coupling constants over one and three chemical bonds are typically positive, the scalar coupling constant over two chemical bonds is typically negative as can easily be deduced following arguments identical to those used for figure 3.1. Because the basis of scalar coupling relies on magnetic interactions between electron spins and distant nuclear spins, the scalar coupling constant rapidly decreases with increasing number of chemical bonds and can typically be ignored for four or more bonds. The scalar coupling constant is independent of the applied external magnetic field, since it is based on the fundamental principle of spin-spin pairing and is therefore expressed in Hz.“ [5]

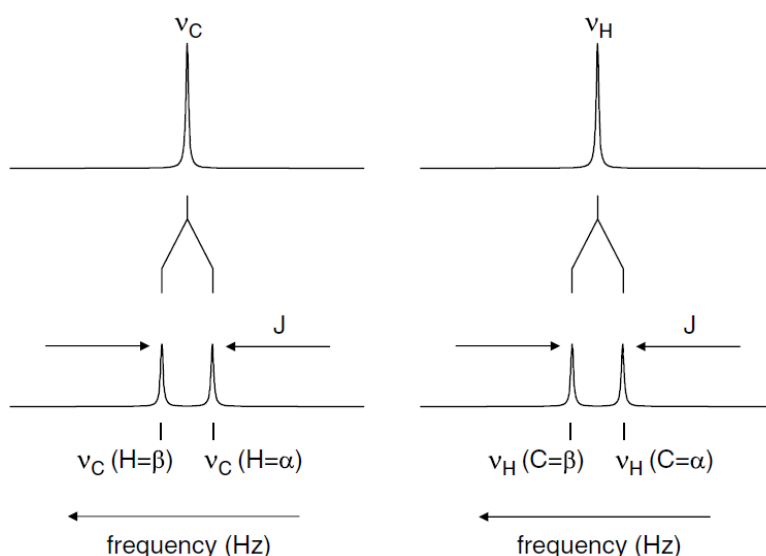


Figure 3.3: Scalar coupling between carbon-13 and proton nuclei leads to a splitting of the singlet resonances into so-called doublet resonances. The resonances at the lower and higher frequencies are associated with energy level transitions, in which the nuclear spin of the scalar-coupling partner is in the α and β spin-state, respectively. [5]

J coupling as can be seen in figure 3.3 is only valid when the frequency difference between the two scalar-coupled spins is much larger than the scalar coupling between them. The described example has a frequency difference of several tens of MHz while the heteronuclear scalar coupling is less than 200 Hz. When the condition $|\nu_A - \nu_X| \gg J_{AX}$ holds, the two-spin AX spin system is referred to as a weakly coupled spin system and the corresponding NMR spectrum referred to as a first-order spectrum. However, for many homonuclear interactions the frequency difference $|\nu_A - \nu_B|$ is of the same order of magnitude as the homonuclear scalar coupling constant J_{AB} , referred to as strongly coupled spin systems. In a strongly coupled spin systems the two spin states $\alpha\beta$ and $\beta\alpha$ become mixed and the simple four-resonance-line spectrum becomes more complicated. [5]

3.3 Phosphorus-31 NMR Spectroscopy

“The relatively high sensitivity of phosphorus NMR (circa 7% of protons), together with a 100% natural abundance allows the acquisition of high-quality spectra within minutes. Furthermore, the chemical shift dispersion of the phosphates found *in vivo* is relatively large (~30 ppm), resulting in excellent spectral resolution even at low (clinical) magnetic field strengths. Phosphorus NMR is very useful, because with simple NMR methods it is capable of detecting all metabolites that play key roles in tissue energy metabolism. Furthermore, biologically relevant parameters such as intracellular pH may be indirectly deduced.” [5]

Figure 3.4 shows a typical, localized, *in vivo* ^{31}P muscle tissue NMR spectrum. The exact chemical shift position of almost all resonances is sensitive to physiological parameters like ionic (e.g. magnesium) strength and intracellular pH. By convention, the PCr resonance is used as chemical shift reference (0.00 ppm). At pH of 7.2 and full magnesium complexation, the resonances of ATP appear at -7.52 ppm (α), -16.26 ppm (β) and -2.48 ppm (γ). Inorganic phosphate (Pi) has its resonance at 5.02 ppm. Resonance peaks can be split into several lines due to spin-spin coupling as can be seen in the ATP peaks in figure 3.4.

The dependence of chemical shift and different physiological parameters as mentioned before is caused by the fact that protonation (or complexation with magnesium) of a compound changes the chemical environment of nearby nuclei and hence changes their chemical shift. A slow chemical exchange between the protonated and unprotonated forms results in two separate resonance frequencies with the resonance amplitudes indicating the relative amounts. However, for most compounds observed with phosphorus NMR, there is a fast chemical exchange (relative to the NMR time scale) and only a single, average resonance is observed. The resonance frequency is now indicative of the relative amount of the protonated and the unprotonated form, and hence the pH can be described by the Henderson-Hasselbach equation:

$$pH = pK_A + \log \left(\frac{\delta - \delta_{HA}}{\delta_A - \delta} \right) \quad (3.5)$$

where δ is the observed chemical shift, δ_A and δ_{HA} the chemical shifts of the unprotonated and protonated forms of compound A, and pK_A the logarithm of the equilibrium constant for the acid-base equilibrium between HA and A.

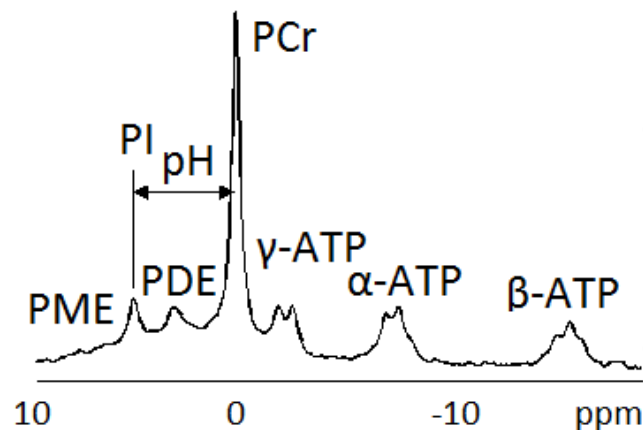


Figure 3.4: Typical *in vivo* ^{31}P NMR spectrum from a skeletal muscle at 1.5 Tesla (PME = phosphomonester, Pi = anorganic phosphate, PDE = phosphodiester, PCr = phosphocreatine, ATP = adenosine triphosphate). Intracellular pH can be calculated with the difference of frequency between PCr and Pi. The ATP molecule consists of atoms with three different chemical environments resulting in three different chemical shifts α , β and γ . The γ -ATP peak may also include contribution from β -adenosine diphosphate (ADP) nuclei, and the α -ATP peak may include contributions from α -ADP nuclei together with nicotinamide adenine dinucleotide (NAD) and nicotinamide adenine dinucleotide phosphate (NADP). The three ATP peaks are sometimes referred to as nucleotide triphosphates (NTP). In this spectrum, the spin-spin splitting of the γ and α ATP peaks into doublets and the β ATP peak into a triplet can be seen. [25] [26]

“Even though almost all resonances in ^{31}P NMR spectra have pH dependence, the resonance of inorganic phosphate (Pi) relative to PCr is most commonly used for several reasons. Its pK is in the physiological range (pK = 6.77), it is readily observed in most tissues (with muscles being a possible exception) and its chemical shift has a large dependence on pH.” [5] [27]

3.4 Chemical Conversion during Muscle Activation

Basis of every muscle activity is the ATPase-activity of the myosin heads, a protein, that is in combination with another protein, actin, responsible for the elastic and contractile properties of muscles [28]. The chemical energy of the hydrolysis of ATP is the instantaneous source of energy for the muscle contraction. Hydrolysed ATP is delivered constantly with such high efficiency that there does not occur a decrease of the ATP concentration (8.2 mM^1 [29]) during workload. ATP is a nucleotide, consisting of an adenine group, a ribose ring and a triphosphate unit (figure 3.5).

¹mM = millimol/liter

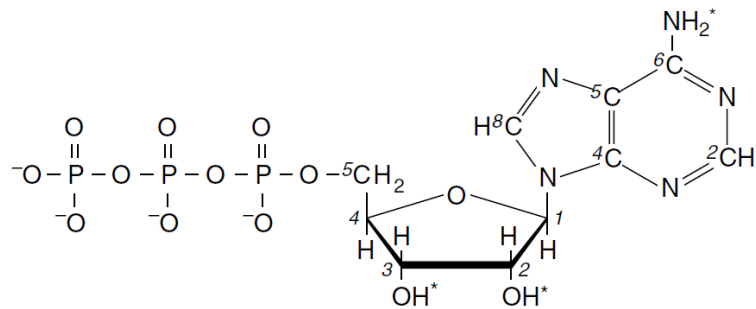


Figure 3.5: Chemical structure of ATP. [5]

There are three main mechanism of ATP regeneration in the muscle:

- ATP is regenerated out of phosphocreatine according to the Lohmann reaction (creatine kinase (CK) reaction), where PCr and Creatine (Cr) serve as an energy buffer: Phosphocreatine is split up into phosphate and creatine to convert ADP into ATP:



The ATP concentration stays constant until the PCr concentration drops from 20 mMol/kg at rest to 2.5 mMol/kg at exercise. This conversion works without oxygen consumption and lactat generation, meaning anaerobic-alactacid. On the other hand during a surplus of ATP, PCr and ADP can also be produced: When one phosphate group is donated to creatine in the creatine-kinase-catalyzed reaction to form phosphocreatine, ATP is converted to ADP.

- Through oxidative phosphorylation 36 Mol ATP/Mol glucose can be produced in the mitochondria. It is called 'oxidative phosphorylation' because the reaction starts with an oxidation, a loss of electrons, and there is a phosphorylation of ADP to form ATP. Energy delivering substrates are carbohydrates and lipids. This ATP supply is aerobic-alactacid. The ATP generated in the mitochondria cannot leave the mitochondria directly: According to the Lohmann reaction Pi is transferred to Cr and can enter the sarcoplasma in form of PCr. PCr is then used for regeneration of ATP out of ADP.
- ATP is generated during glycolysis where glucose is reduced. With reduction of glycogen 3 Mol ATP/Mol glucose can be produced, with reduction of free glucose only 2 Mol ATP/Mol glucose can be generated. This process is anaerobic and generates lactat (anaerobic-lactacid).

Once a muscle starts to be active, anaerobic regeneration of ATP is the only active mechanism since the oxidative phosphorylation takes time to adjust to the increased demand of ATP. Therefore PCr decreases according to the Lohmann reaction, while ATP stays constant. After the

end of exercise PCr is regenerated out of ATP with the reversed Lohmann reaction. The ATP needed for this reversed reaction is produced with the oxidative phosphorylation. The rate of ATP hydrolysis during exercise can increase 50 to 100-fold to the rest metabolic rate. The oxygen consumption increases also by 50 to 100-fold, since the oxygen consumption per ATP stays constant as long as ATP is exclusively produced out of oxidative phosphorylation. When the border of ATP production through oxidative phosphorylation is crossed, then ATP is generated out of glycogen reduction (anaerobic). This is only a short-term solution since the glycogen reserves are limited and the end product lactat is accumulated in the muscle fibers and in the blood plasma. This increase of lactat results in a decrease of pH. [5] [19] [30] [31] [32]

3.5 Dynamic ³¹P Phosphor MRS

Dynamic ³¹P MRS is a method established for direct measurement of the metabolic changes in the muscle during and after physical exercise to study the kinetics of energy metabolism *in vivo* [33].

Several approaches to measure, interpret and quantitatively analyze ³¹P-MRS observations of energy balance in the muscle during and after exercise have been proposed. In addition, it is possible to estimate the rates of glycogenolytic and aerobic ATP synthesis, i.e., oxidative capacity, employing protocols addressing various types of exercise, e.g., pure aerobic exercise under steady-state conditions or during work jumps, ischemic exercise, and mixed exercise.

Dynamic measurements of the initial rate of PCr depletion during pure aerobic work jumps yield an estimate of the total rate of ATP synthesis. [34]

The initial recovery rate of PCr (V_{PCr}) can be expressed as a recovery-time constant and is thought to reflect maximal ATP turnover from oxidative metabolism via the CK reaction at the end of exercise [33]. The muscle oxidative capacity (Q_{max}) can also be calculated. Because the PCr concentrations are proportional to the rate of oxygen consumption and the rate of PCr recovery represents the maximal rate of oxygen consumption, the PCr resynthesis rate after exercise represents Q_{max} . „However, the use of the PCr resynthesis rate as an index of muscle oxidative capacity can be applied only under a condition in which the intracellular pH does not significantly decline, because the rate varies not only due to the muscle oxidative capacity but also due to the intensity of exercise performed. It has been reported that high-intensity exercise induces a significant decrease in intracellular pH, which slows the rate of PCr resynthesis.“ [34] As described in chapter 3.3, an additional and important piece of information retrievable from ³¹P spectra is intracellular pH which can be deduced from the chemical shift of Pi relative to PCr [33].

Figure 3.6 shows a typical time course of ³¹P spectra: According to the Lohmann reaction (equation 3.6), during exercise, ATP concentration stays constant whereas PCr concentration decreases and Pi concentration increases. The level of depletion yields an estimate of the total rate of ATP synthesis and, therefore, about the difficulty of the exercise. With the PCr recovery time constant (τ) revealing the steepness of the PCr curve directly after the exercise, the initial recovery rate of PCr and, consecutively, oxidative flux can be deduced.

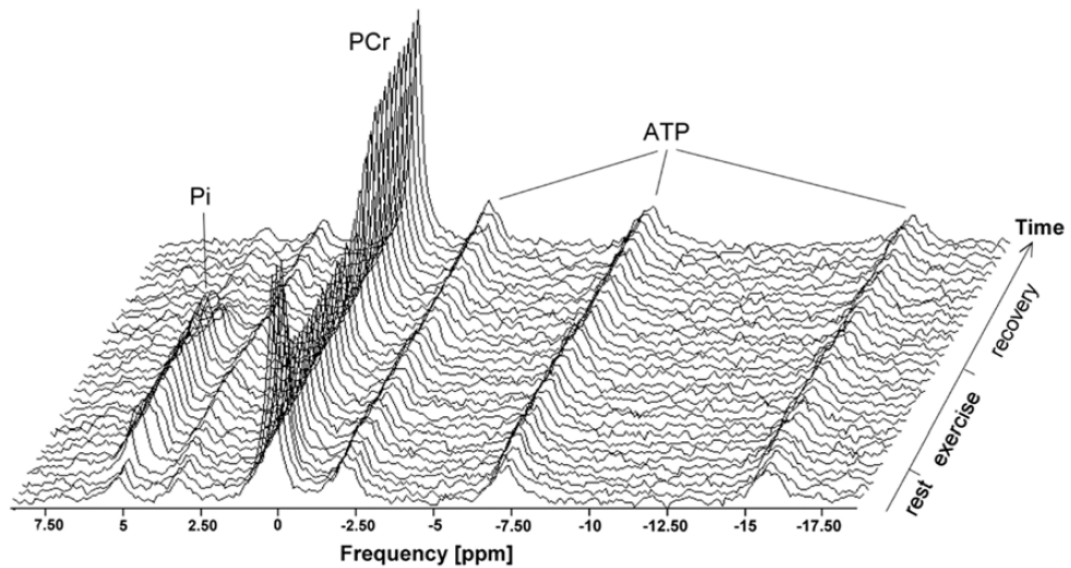


Figure 3.6: Time course of the ^{31}P spectra during rest, exercise and subsequent recovery. [35]

3.6 Exercise-induced Linewidth Changes in NMR Spectra

In dynamic ^{31}P -MRS data, changes in linewidth of PCr and Pi peaks can be commonly observed. Exercise-induced linewidth increase of intramyocellular PCr is related to myoglobin oxygenation, as one can observe a slow increase on start of exercise [36].

A general explanation can be done with BOLD (blood oxygenated-level dependent) contrast commonly used for functional MRI (fMRI) that is based on the same principle. The contrast arising from the BOLD effect occurs due to the combination of three key effects: First, changes in tissue activity are accompanied by local changes in blood oxygenation. Oxygenated hemoglobin contains no unpaired electrons and is therefore diamagnetic, which means the magnetic field in the oxygenated hemoglobin is lower than that outside. Deoxygenated hemoglobin contains four unpaired electrons per heme unit (there are four heme units per hemoglobin molecule) and is therefore paramagnetic. The magnetic field of deoxygenated hemoglobin is higher than that outside, and the field change is linearly proportional to the strength of the external magnetic field. The net effect is that the magnetic field inside blood vessels can be altered depending on the blood oxygenation level. The second key effect is the effect of spatial magnetic field distortion, such as that caused by a magnetic field gradient between inside and outside a blood vessel, on the magnetic relaxation times, particularly T_2 and T_2^* . Third, the increase in oxygen consumption occurs simultaneously with a local increase in blood flow. The increase in oxygen delivery exceeds the increase in oxygen demand, and the net change is an increase in blood oxygen level when tissue is active. [37]

Going back from BOLD contrast in fMRI to dynamic ^{31}P Phosphor MR spectroscopy, Andreisek et al. [38] explains the physiologic changes during exercise of the calf muscles: „During mus-

cle activity, increased oxygen consumption typically increases the oxygen extraction fraction, causing decreased T_2^* relaxation times. At the same time, increased inflow of fresh oxygenated blood counteracts the increased oxygen extraction fraction; once the oxygen supply caused by this inflow exceeds the increases in oxygen extraction fraction, T_2^* starts to increase. The muscle response also includes vasodilatation, which increases the overall capillary blood volume. An increased absolute amount of oxygenated blood in the arterial system of capillaries will increase the overall T_2^* , similar to overcompensation in oxyhemoglobin. At the same time, however, the volume of deoxyhemoglobin in the venous system of the capillaries increases as well, which results in a larger pool of blood with inhomogeneous signal, so the T_2^* contributions can increase, resulting in lower T_2^* signal. In addition to the vascular changes, an increasing amount of deoxygenated myoglobin during muscle activity can be observed, which compounds the effects of deoxygenated hemoglobin on T_2^* .“ Varghese et al. [39] shows the coupling of exercise induced changes in T_1 and T_2 in lower extremities and changes in blood flow.

Schmid et al. [40] deals with exercising calf muscle T_2^* changes resulting not only from alterations in capillary blood oxygenation and volume but most prominently from tissue water distribution. The study found a strong link between mitochondrial function, cellular energy metabolism, acid-base equilibrium and T_2^* during exercise and recovery. In particular, pH time courses apparently induce the observed T_2^* weighted signal time course. Osmotic effects of altered metabolite and acid-base equilibrium contribute to alterations in the water content. Increased metabolic activity such as glycogenolysis into lactate and PCr breakdown into Pi and PCr results in accumulation of metabolites to which the cell membrane is relatively impermeable. The accompanying osmotic pressure leads to water shift between intra- and extracellular compartments and hence to observable T_2 changes. [40]

This effect is seen in the spectroscopic linewidth since it is inversely proportional to the lifetimes of the energy states under observation according to Heisenberg uncertainty principle [41]: Since linewidth is energy uncertainty ($h\Delta\nu$), Heisenberg's relation can be formed to:

$$\Delta E \Delta t \geq \frac{h}{2\pi} \quad (3.7)$$

$$h\Delta\nu \Delta t \geq \frac{h}{2\pi} \quad (3.8)$$

$$\nu_{1/2}/2 \geq \frac{1}{2\pi T} \quad (3.9)$$

$$\nu_{1/2} \geq \frac{1}{\pi T} \quad (3.10)$$

with T being the relaxation times, $\nu_{1/2}/2$ the half-width at half height and therefore $\nu_{1/2}$ width at half height [42].

„The effect is far less pronounced in nonlocalized spectra which contain larger fractions of resting tissue and have a larger linewidth due to stronger B_0 inhomogeneities across the large sensitive volume.“ [36]

Fundamentals of used Localization Methods

In most dynamic ^{31}P -MRS measurements a surface coil is used because of its simplicity, high sensitivity and favorable filling factor¹. „A small sample in a large coil produces a much lower signal-to-noise ratio than the same sample with a smaller RF coil. Surface coils are therefore useful *in vivo* MRS, as they limit the reception of noise and signal to the tissue region of interest. However, the depth of penetration in the sample is limited to approximately one radius of the surface coil. Larger coils are much less sensitive but provide a more uniform RF field for accurate RF pulse transmission. The combination of transmission with a large coil for RF excitation homogeneity and reception with a small surface coil for increased sensitivity makes use of the advantages of both types of coils.“ [19]

The whole sensitivity volume of the surface coil is used in many studies as the volume of interest, from where the signal is acquired. The fundamental disadvantage of the surface coil localization method (often referred to as non-localized method) is the poor resolution between different tissues or tissue structures. For improved localization, it is customary to use a technique that employs pulsed sequences. [43] With localization methods signal from a defined volume of interest is acquired, while signal contamination from surrounding tissue is minimized [44].

Two different localization methods that have been used in this master thesis for the signal localization from the gastrocnemius medialis muscle are described in this chapter.

¹„The filling factor is a measure of the geometric relationship between a magnetic resonance imaging coil and the body. This relationship affects the MR signal-to-noise ratio and, ultimately, image quality. Achieving a high filling factor requires fitting the coil closely to the body, thus potentially decreasing patient comfort.“ [28]

4.1 Slice-Selective Localization by Adiabatic Selective Refocusing (semi-LASER)

Before handling with semi-LASER localization, localization by adiabatic selective refocusing (LASER) shall be discussed first.

LASER is a single-scan 3D localization method executed with adiabatic multiple spin-echo scheme and refocusing RF pulses. Instead of using three 180° slice-selective pulses in three directions, three pairs of adiabatic full passage (AFP) pulses are used after a nonselective excitation by a 90° adiabatic B_1 -independent rotation (BIR)-4 pulse (see figure 4.1). [45]

„The B_1 produced by a surface coil varies throughout space, but the sensitivity gain provided by such coils is a major advantage for many *in vivo* NMR applications. Within the sensitive volume of a typical surface coil, the amplitude of B_1 varies by > 10 -fold, which means the flip angle also varies by > 10 -fold across the sample when conventional (constant frequency) pulses are transmitted with this coil. In many experiments, flip angle errors cause sensitivity losses, quantification errors, and artifacts (e.g. undesirable coherences).“ [15] Adiabatic pulses (see chapter 2.7) can excite, refocus or invert magnetization vectors uniformly, even in the presence of a spatially nonuniform B_1 field, and are therefore predicted for the use with surface coils.

A single AFP pulse (see figure 4.2) in the presence of a magnetic field gradient can achieve slice-selective refocusing. „However, the frequency modulation of the pulse induces a nonlinear B_1 and position dependent phase across the slice which will lead to severe signal cancellation. A second, identical AFP pulse can refocus the nonlinear phase such that perfect refocusing can be

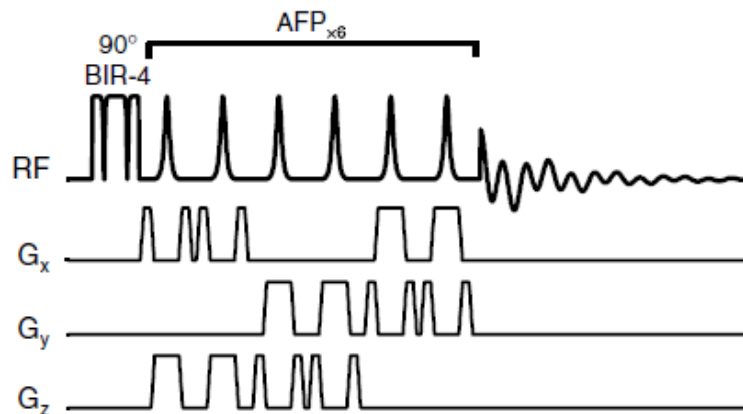


Figure 4.1: Pulse sequence for 3D LASER localization: A nonselective excitation is applied using the adiabatic pulse BIR-4, while refocusing is performed with three pairs of AFP pulses, each selecting an orthogonal spatial slice, thereby defining a 3D volume. Magnetic field crusher gradients surrounding the AFP pulses ensure removal of all unwanted coherences from outside the localized volume. The echo-time TE is defined from the end of the BIR-4 pulse to the beginning of acquisition. [5]

achieved. Since frequency-selective adiabatic excitation pulses remain elusive, the entire sample is excited with a nonselective adiabatic excitation pulse after which three pairs of AFP pulses achieve 3D localization by selectively refocusing three orthogonal slices.“ [5]

„Universal rotations can be accomplished with the class of composite adiabatic pulses known as B_1 -insensitive rotation (BIR, see figure 4.2). BIR pulses can uniformly rotate all components of magnetization lying in a plane perpendicular to the rotation axis which remains constant despite changes in B_1 amplitude.“ [15] BIR-4 consists of a double BIR-1, which is the first generation of plane rotation pulses and provides a constant rotation axis for moderate resonance offsets. The BIR-4 pulse achieves excitation while refocusing is performed with three pairs of AFP pulses. [5] [15]

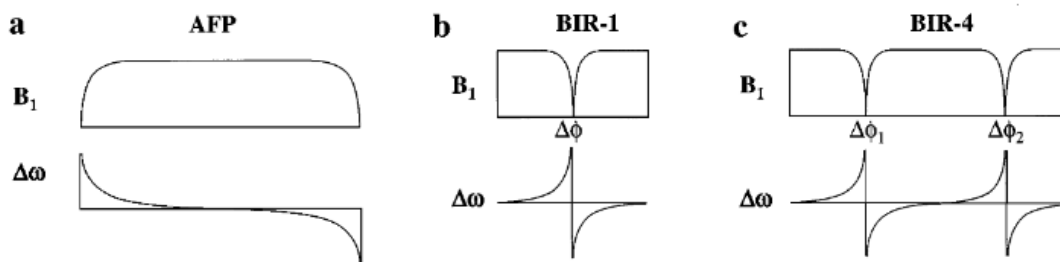


Figure 4.2: Examples of adiabatic pulses: (a) AFP (b) BIR-1 and (c) BIR-4. [15]

In slice-selective localization by adiabatic selective refocusing (semi-LASER), a non-adiabatic slice selective excitation module is applied instead of the BIR-4 pulse and one refocusing AFP in LASER. Therefore, a 3D localization scheme is accomplished with only two pairs of frequency-selective AFP refocusing pulses. This localization method is designed for use with a surface coil, as a surface coil produces a RF field, which is relatively homogeneous in the direction parallel to the plane of the coil. The slice-selective excitation is, therefore, applied along this direction. An advantage of the adiabatic refocusing RF pulses used in the semi-LASER sequence is the high bandwidth and the alleviation of the effects of the inhomogeneous amplitude of the B_1 field of a simple loop coil that is used for excitation and signal detection. [46] [45]

4.2 Depth-resolved Surface Coil Spectroscopy (DRESS) Localization

The depth-resolved surface coil spectroscopy (DRESS) technique was developed by Bottomley et al. [47] DRESS couples surface coil localization with a slice-selective gradient analogous to that used in imaging. A simultaneous application of a frequency-selective RF pulse (90°) and linear B_0 gradient excite the spins in a plane parallel to the surface coil (see figure 4.3). This is achieved by an B_0 gradient along the axis that is perpendicular to the plane of the surface coil. The combination of the narrow-bandwidth selective excitation pulse and applied gradient field excites a flat plane of nuclei parallel to the surface coil plane. To gain a rectangular profile of the selected slice, the amplitude of this RF pulse must not be constant but must have a SINC

($\sin(x)/x$) or similar shape. Position and thickness of the selected slice can be easily controlled by changing the strength of the magnetic field gradient, the frequency of the excitation pulse and/or its duration. The extent of the sensitive volume within the selected plane is determined only by the diameter of the receiving surface coil and the distance of the receiving surface coil from the selective plane.

„Due to the static gradient during the excitation, nuclei at various depths within the selected slice will have different phases after the selection, leading to loss in signal intensity. In order to correct for this, a rephasing gradient pulse is applied immediately after the selective RF excitation pulse. The free induction decay is acquired immediately after this rephasing gradient and the Fourier transform of the FID provides a localized spectrum from a disc-shaped volume“ [43]

The positioning of the selective slice can be easily done on a reference NMR image. The DRESS method substantially eliminates surface tissue contamination of the chemical shift spectra. However, it should be remembered that as one goes deeper into the tissue, the signal received will be weaker, in accordance with the B_1 distribution of the surface coil. Another disadvantage is that, as it is only a one-dimensional gradient selection technique, movement of the region of interest along the other two dimensions requires moving the surface coil. [43] [44] [48]

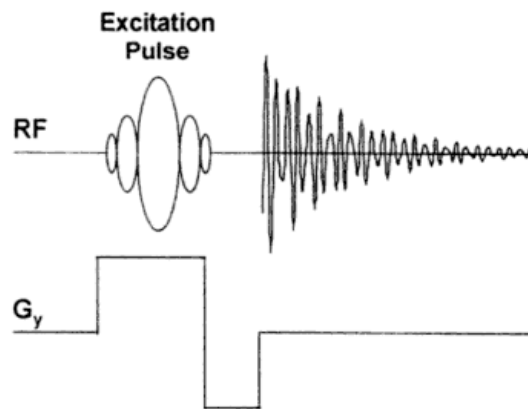


Figure 4.3: DRESS pulse sequence: A linear B_0 gradient, leading to excitation of spins in a plane parallel to the surface coil, followed by a frequency-selective RF pulse (90°). [43]

Aim of the Thesis

Dynamic ^{31}P -MRS during exercise allows non-invasive determination of mitochondrial capacity of the skeletal muscle *in vivo*. Although exercise-recovery ^{31}P -MRS experiments are used in many institutions for a range of applications, the published values in healthy volunteers often differ between the sites [49] [50] [51] [52]. This discrepancy is often referred to as caused by different subject pool, measurement protocol, data processing or equipment used. The individual differences can, of course, play a major role in small studies, but their importance tend to decrease in more populated studies. On the other hand, most of the experiments use surface RF coils with different geometry for signal localization, and there are, next to commercially available MR compatible ergometers, many home-built devices [53] [54] [55]. The study equipment used (e.g., the ergometer or the RF coil) counts then probably as the most likely source of differences of the whole experiment.

Another inaccuracy can arise from the rough signal localization by the sensitive volume of the surface RF coil. This is often used for dynamic ^{31}P -MRS measurements due to its high SNR, simplicity and robustness. However, accuracy of such localization is poor and therefore distinction between muscle groups, involved differently in muscle exercise [40] [56] [57], is not possible. Identifying the impact of small, spatially defined injuries, myopathies or functional deficits in peripheral arterial diseases is also not possible without more precise localization approach [58].

Therefore, aim of this master thesis is to investigate the impact of magnetic field strength, ergometer construction, RF coil diameter, workload and localization method on the metabolic parameters measured by dynamic ^{31}P -MRS in soleus and gastrocnemius muscle during plantar flexion. To address all of the risen questions, three individual studies were conducted:

1) **Impact of different magnetic field strength and experimental equipment on the measured metabolic parameters**

This multicenter study was conducted in two research institutes: MR-Unit, Dept. Diagnostic and Interventional Radiology, Institute for Clinical and Experimental Medicine, Prague, Czech Republic in the following chapters referred to as first institute and High-

Field MR Center of Excellence, Department of Biomedical Imaging and Image-guided Therapy, Medical University Vienna, Vienna, Austria in the following chapters referred to as second institute. Specific points:

- Impact of ergometer design (pneumatic and mechanic)
- Impact of surface coil diameter
- Impact of magnetic field strength (3 Tesla and 7 Tesla)
- Comparison of three different exercise workloads: low (7.5 kg ~1.2 bar), mild (11 kg ~1.8 bar) and heavy (2.4 bar)

2) Comparison of non-localized vs. DRESS localization method

This study was performed at the High-Field MR Center of Excellence in Vienna using a MR system with a magnetic field strength of 7 Tesla. Specific point:

- Comparison of two different localization methods: Non-localized and DRESS localized data (as explained in chapter 4)

3) Comparison of DRESS vs. semi-LASER localization and non-localized method

This study was also performed at the High-Field MR Center of Excellence in Vienna at 7 Tesla. Gastrocnemius medialis specific oxidative metabolism measured with semi-LASER and DRESS localization sequences was compared to each other and to non-localized acquisition.

Methods

6.1 Region of Interest: Posterior Leg

The posterior compartment of the leg is subdivided by a transverse septum into two parts, superficial and deep. The transverse septum is attached to the soleal line of tibia above, the medial border of tibia medially, the posterior border of fibula laterally and is continuous with the flexor retinaculum below. The superficial region, which is the region of interest for this master thesis, can be subdivided into three superficial muscles of the calf, two large ones, the gastrocnemius and soleus (figure 6.1), and one small muscle, plantaris, that lies between the other two.

The gastrocnemius muscle is the most superficial of the posterior leg muscles and is a bulky muscle with two heads. It forms the principal mass of the calf. The muscle arises by two heads from the posterior surface of the femoral condyles (lateral head from lateral condyle of femur; medial head from upper and posterior part of medial condyle). The tendinous origin of the medial head is separated from the capsule of knee joint by a bursa.

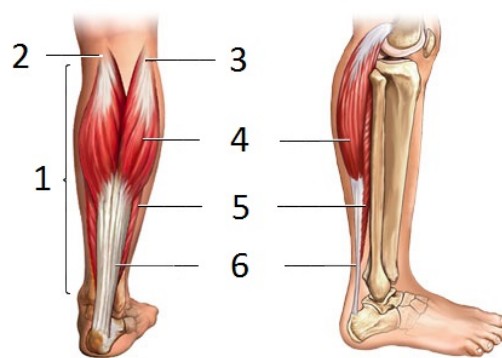


Figure 6.1: 1: Calf muscles, 2: Medial condyle of the femur, 3: Lateral condyle of the femur, 4: Gastrocnemius, 5: Soleus, 6: Achilles tendon [59]

The soleus muscle, on the other hand, is a very powerful muscle situated deep to the gastrocnemius that has a broad, horseshoe-shaped origin in the upper one-third of the posterior surface of the upper fibula and the soleal line of the tibia.

Planeris is a vestigial muscle with a small belly and long tendon, lying under cover of the lateral head of gastrocnemius.

The gastrocnemius, planeris and soleus join to form a tendon called tendocalcaneus (Achilles tendon) by which it is inserted into the middle one-third of the posterior surface of calcaneus.

The gastrocnemius and soleus together provide the main propulsive force in walking and running, though gastrocnemius is more active in these movements. More specifically, these two muscles are involved in the plantar flexion of the foot at the ankle joint. While gastrocnemius plays pivotal role in plantar flexion of a leg with extended knee, as it is the flexor of knee joint, in flexed position of the knee it cannot act on the ankle joint, so soleus alone is responsible for the plantar flexion in flexed knee. [60] [61] In this master thesis, the movement of plantar flexion of the foot with extended knee is examined, therefore, the medial head of the gastrocnemius is expected to be the most intensely working muscle. At the position selected for spectroscopy, its cross-sectional area occupies approximately 20% of the total cross-sectional area of calf muscles [36].

6.2 Study participants

In the multicenter study eleven healthy subjects (3f/8m, 36 ± 12 years, BMI: 23.5 ± 2.5 kg/m², no active sportsman or smoker) have participated (for detailed information see A.1).

Fourteen healthy subjects (4f/10m, 42 ± 6 years, BMI: 30.8 ± 4.1 kg/m², no active sportsman or smoker) were recruited for the non-loc/DRESS study (for detailed information see B.1).

Five healthy male subjects (27 ± 1 years, BMI: 22.0 ± 2.5 kg/m², no active sportsman or smoker) participated in the DRESS/semi-LASER/non-loc study (for detailed information see C.1).

The local ethics committee approved the study protocols and written informed consent was obtained from all subjects.

6.3 Used Equipment

Both institutes used MR-compatible ergometers suitable for plantar flexion exercise in supine position. In the first institute a home-built mechanical ergometer is available whereas the second institute uses a commercially available ergometer with a pneumatic piston and sensors for force and pedal angle („Trispect“ by Ergospect, Innsbruck, Austria) as can be seen in figure 6.2.

In the custom-built ergometer the pedal force was adjusted with the Professional Control Unit provided by Ergospect, Innsbruck, Austria (program software „ErgoSpectControl“ regulating the ergometer's pneumatic system). The workload in the home-built mechanical ergometer is defined by the weight of counterweights pulling the pedal into upright position.

To secure same workloads on the different ergometers in both institutes, the force for pressing the pedal was calibrated. The used workloads 7.5 kg and 11 kg in the first institute equals to 1.2 bar and 1.8 bar in the second institute due to the performed calibration.



Figure 6.2: Left: Home-built ergometer with mechanical system used in first institute. Right: Ergospect ergometer with pneumatic system used in second institute.

^{31}P -MRS acquisition was performed on three MR systems from the same manufacturer (Siemens Healthcare, Erlangen, Germany): 3T (TIM Trio) in the first institute and 3T (TIM Trio) and 7T (Magnetom) whole-body MR system in the second institute. The multicenter study contains data from all three systems, whereas the measurements of different localization methods (non-loc/DRESS and DRESS/semi-LASER/non-loc) were solely compared on the 7T system in the second institute.

For RF transmission and reception of NMR signals a flexi dual channel $^1\text{H}/^{31}\text{P}$ surface coil (\varnothing 11 cm, Rapid Biomedical, Rimpar, Germany) was used in the first institute, whereas the coils used in the second institute were inflexible dual channel $^1\text{H}/^{31}\text{P}$ surface coils (\varnothing 10 cm, Rapid Biomedical, Rimpar, Germany). Both coils in the second institute although built for different MR field strengths, have similar sensitivity volumes [35]. The coil was fixed to the medial head of the gastrocnemius muscle to minimize possible misplacement artifacts.

6.4 Coil map evaluation

To assess the impact of different sensitivity profiles of the RF coils used, maps of ^{31}P signal from calf muscle of five volunteers participating in the multicenter study were measured and compared.

Measurements were performed on 3T systems at both sites using a 3D MRS imaging sequence with $\text{VOI} = 200 \times 200 \times 200$ mm, matrix = $12 \times 12 \times 12$, 2 averages, and the rest of the parameters similar to the dynamic experiment to gain the best conditions for comparison ($\text{TE} = 1$ ms, $\text{TR} = 2$ s, flip angle = 42° , vector size = 1024, bandwidth = 3000 Hz and rectangular excitation pulse duration = $400 \mu\text{s}$).

The maps of PCr signal were calculated from the center slice of the 3D ^{31}P MRSI data using the fitting routine of the Syngo MR software (Siemens Healthcare, Erlangen, Germany). Regions of interest were manually drawn over soleus, gastrocnemius medialis and gastrocnemius lateralis muscles. The ratio of the signal within these muscles to the total PCr signal measured by the coil was calculated using a home-written software in MATLAB (Mathworks, Natick, Massachusetts, USA).

6.5 Exercise Protocol

The subjects were instructed to perform plantar flexions once every 2 seconds over the normal range of foot flexion in distal direction with the left leg in the multicenter study and with the right leg in the other two studies. To minimize motion-related artifacts, the subjects were trained to return their foot to the neutral position before each MR excitation and acquisition, which was triggered acoustically.

A standardized exercise protocol was performed according to [62]: 2 minutes rest - 6 minutes exercise and 6 minutes recovery (2 minutes of rest in the beginning serve as baseline measurement). For the multicenter study this dynamic measurement was carried out two times in the first institute with different workloads in the following order: low workload (7.5 kg) - 7 minutes break - mild workload (11 kg). In the second institute the dynamic measurement was done three times with different workloads: mild workload (1.8 bar) - 7 minutes break - low workload (1.2 bar) - 2 minutes break - heavy workload (2.4 bar). Due to the lower workload of the second measurement, the break between second and third measurements was decreased. Adding up the measured resting and recovering periods the physical inactivity duration for the muscles was 15 minutes and 10 minutes respectively (figure 6.3). The heavy workload was not performed in the first institute due to the limitation of the ergometer to a smaller workload.

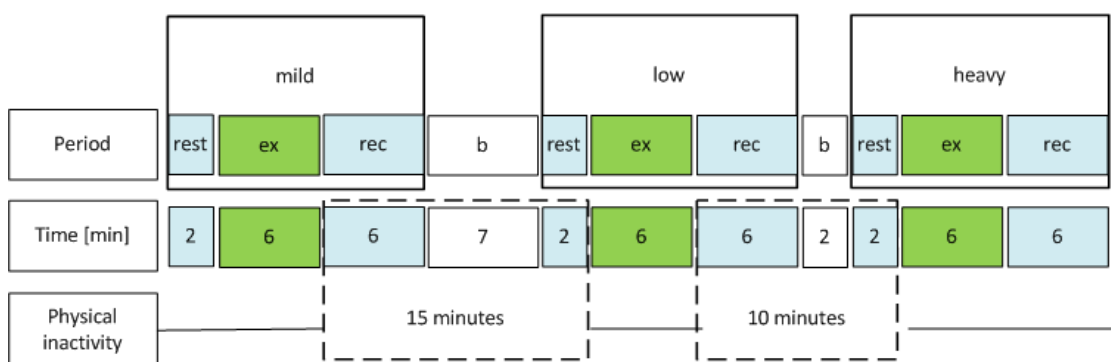


Figure 6.3: Exercise protocol in multicenter study at second institute: Three dynamic measurements with plantar flexion exercise, spaced by 10 and 15 minutes of physical inactivity. (ex = exercise, rec = recovery, b = break)

In the comparative measurements of DRESS and non-localized region of interest, the order of DRESS and non-localized dynamic measurement was randomized to avoid any possible influence of the order on results of the comparison. The protocol of each dynamic measurement was identical to the multicenter study. Physical inactivity of the muscles between the two exercises was 15 minutes (7 minutes break between measurements). The workload, equal for both exercises, was set to 25% of the maximum voluntary contraction (MVC) beforehand measured on a home-built device similar to [53] (for detailed settings see table B.1).

The comparative measurements with DRESS, semi-LASER and non-localized region of interest were also done in randomized order. The five subjects exercised three times with a force always

set to approximately 124.3 N (= 2 bar). The physical inactivity between the exercises was at least 15 minutes.

6.6 NMR Pulse Sequences

In the images obtained by the localizer sequence the adjustment volume was set to the region of interest (gastrocnemius and soleus) and the homogeneity of the local magnetic field was adjusted until the linewidth at half maximum of the water peak was at its minimum, approximately 40 and 50 Hz (magnitude mode).

The non-localized acquisition sequence in the multicenter study was identical for both 3T systems in both institutes (rectangular 400 μ s excitation, $TE^* = 0.4$ ms) and for the 7T system with the increase in acquisition bandwidth (5 kHz instead of 3 kHz). The global signal maximum was used to define a 90° pulse and consecutively the excitation flip angle was set to 42° and 48° for 3T and 7T respectively, to achieve the highest SNR per unit of time during the dynamic protocol based on the published relaxation times [22]. Table 6.1 shows calculated flip angle (formula 2.47) values for different T_1 relaxation times. It can be seen, that a flip angle with focus on PCr and Pi was chosen.

In the non-loc/DRESS study for the non-localized acquisition sequence identical adjustments as in the multicenter study were set (rectangular 400 μ s excitation, $TE^* = 0.4$ ms bandwidth 5 kHz), except for the flip angle (52°). A flip angle of 52° was chosen to focus on the PCr peak. DRESS localization was performed with a slice-selective sinc 600 μ s excitation and $TE^* = 0.4$ ms with no additional pulse adjustment.

Similar to non-loc/DRESS, in the DRESS/semi-LASER/non-loc comparative study, pulse adjustment was performed once in non-localized fashion, while the semi-LASER measurement had to be adjusted individually to the set single voxel volume. For DRESS and non-loc a flip angle of 52° was taken. For semi-LASER measurements the adjustment values were chosen according to [46] ($TE = 23$ ms, $TR = 6$ s and consequently 140 measurements instead of 420 due to the increased TR). The flip angle was set to 90° due to the longer TR. The performance of plantar flexion was nevertheless done every 2 seconds (three times during TR) to secure similar exercise intensity.

	PCr	Pi	γ -ATP	mean of PCr and Pi	mean of PCr, Pi and γ -ATP	mean of all
3T	42.1	41.6	46.0	41.8	43.1	43.7
7T	52.7	43.3	56.9	47.3	50.0	54.0

Table 6.1: Calculated flip angle for different T_1 relaxation times according to [22]: Flip angle according to the relaxation time T_1 of the metabolites PCr, Pi and γ -ATP, the mean value of PCr and Pi as well as PCr, Pi and γ -ATP and the mean value of the most prominent metabolites in the muscle (phosphomonoesters (PME), Pi, phosphodiester (PDE), PCr, α -ATP, β -ATP and γ -ATP).

TR and TE of semi-LASER is increased in comparison to the other measurements due to the duration of the refocusing pulses. With shorter repetition times it would not be adiabatic due to the lack of power within the specific absorption rate (SAR)¹limits. The minimum achievable TE of 23 ms can slightly increase when the refocusing RF pulse durations are adapted depending on the required RF power, with the maximum transmitter voltage applicable to the surface coil as the limiting factor.

For the assessment of metabolite concentrations, in all studies a partially relaxed static spectrum (TR = 15 s, 16 averages) was recorded. For the first two studies, a non-localized static spectrum with a flip angle of 90° and TE* = 0.4 ms was recorded. In the DRESS/semi-LASER/non-loc study the static spectrum for DRESS was done with TE* = 0.4 ms and a flip angle of 60°, because the coil was at its power limit. The static spectra of non-localized and semi-LASER localized were acquired with a flip angle of 90°.

Figure 6.4 shows the positioning of the region of interest (slice for DRESS localization and single voxel for semi-LASER localization) done in the gastrocnemius medialis muscle measured for this master thesis. The region of interest was placed in an oblique fashion over the muscle, avoiding overlap to adjacent muscle groups.

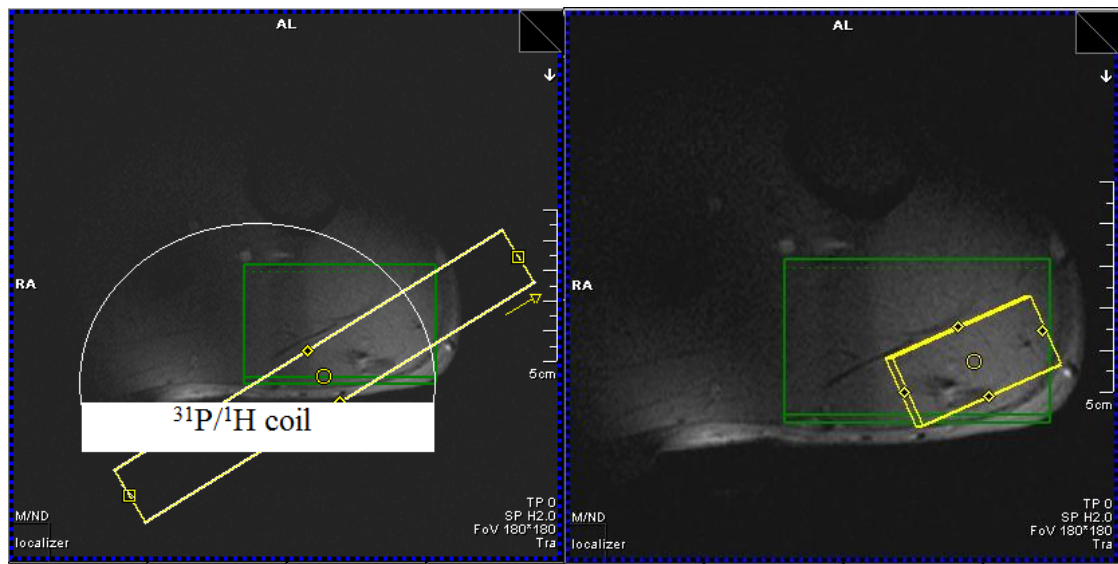


Figure 6.4: Non-localized region of interest of $^{31}\text{P}/^1\text{H}$ coil (white), 20 mm wide DRESS selection slab (yellow) (left picture) and semi-LASER localization (right picture) in the gastrocnemius medialis muscle (subject #1 from DRESS/semi-LASER/non-loc study). Size of the single voxel can slightly vary between subjects depending on the muscle mass. The green box depicts the adjustment volume for shimming.

¹The specific absorption rate is defined as the RF power absorbed per unit of mass of an object and is measured in watts per kilogram. It is a parameter that describes the potential for heating of the patient's tissue due to the application of the RF energy. It increases with field strength, radio frequency power, transmitter-coil type and body size. SAR can be reduced by lower flip angle and longer repetition times. [63]

6.7 Data Postprocessing in jMRUI

Quantification of the 420 spectra (14 minutes with TR = 2 s, non-localized and DRESS localization) and 140 spectra (14 minutes with TR = 6 s, semi-LASER localization) was done in jMRUI (5.0 software package) using the AMARES (Advanced Method for Accurate, Robust and Efficient Spectral fitting) time domain fitting routine [64]. Prior applying the AMARES algorithm, the spectra were phased, but no zero-filling or filtering was applied. The peaks were fitted as single Lorentzians, besides ATP signals where the α - and γ -ATP were modeled as Lorentzian doublets and β -ATP as a triplet. Intracellular pH was calculated according to [65] (Henderson-Hasselbalch equation, see also chapter 3.3), using the relative chemical shift difference δ between Pi and PCr in parts per million (δ):

$$pH = pK + \log \left[\frac{(\delta - \delta_{HA})}{(\delta_A - \delta)} \right] \quad (6.1)$$

with $pK = 6.75$, $\delta_{HA} = 3.27$ and $\delta_A = 5.69$.

Since several muscles are detected in non-localized data, the Pi peak can split up in two peaks when exercise changes the pH in the active muscle, but not in the less active muscles. The splitting up of the Pi peak cannot be seen in every subject, since the relative difficulty of the exercise and involvement of muscles in the performed exercise varies between subjects. For an untrained subject acidosis can occur faster and two Pi peaks are seen sooner. When two Pi resonances became discernible, they were fitted as two separate Lorentzian peaks (giving non-acidifying pH_1 and acidifying pH_2). For further calculations, only the pH_1 near 4.94 ppm, determined in all volunteers, was used.

The range of linewidth was soft constrained for the γ -ATP, Pi and PCr peak. Since γ -ATP stays constant during rest and exercise, the range of linewidth was set to just ± 1 Hz. In a few data sets from the first institute this range was too narrow leading to underestimation of the ATP signal and, therefore, in these special cases linewidth of ATP was not soft constrained at all.

The range of linewidth for Pi and PCr was set bigger than in γ -ATP due to the increase of linewidth during exercise. Exercise-induced linewidth increase of intramyocellular PCr can be explained with the effect on myoglobin deoxygenation as explained in chapter 3.6. Pi linewidth is known to change due to intracellular pH changes and has been attributed to compartmentation as explained in chapter 3.6 [36]. The increase of intracellular concentrations of hydrogen ions (pH) changes the magnetic field and, therefore, relaxation times as shown by Schmid et al [40] similarly to deoxygenated hemoglobin in the BOLD effect.

6.8 Further Calculations

The integrated signal intensities and calculated pH values for each of the 140 respectively 420 spectra gained from the processing in jMRUI were further evaluated in MATLAB.

The signal intensity has to be divided by a correction factor to gain the magnetization for the PCr, the Pi and the γ -ATP signal:

$$M = \frac{\text{signal}}{\text{correction factor}} \quad (6.2)$$

whereas the correction factor is deduced from the relaxation formulas $M_z(\alpha, T_1)$ and $M_{xy}(\alpha, T_2)$ given in [5]:

$$\text{correction factor} = \frac{\left(1 - e^{-\frac{TR}{T_1}}\right)}{1 - \cos(FA \cdot \pi/180^\circ) \cdot e^{-\frac{TR}{T_1}}} \cdot \sin(FA \cdot \pi/180^\circ) \cdot e^{-\frac{TE^*}{T_2}} \quad (6.3)$$

The used parameters used for formula 6.3 are given in table 6.2.

mag. field	study & localiz.	FA	TR	T ₁			T ₂			TE*/TE
				PCr	γ -ATP	Pi	PCr	γ -ATP	Pi	
3 T	1. nonloc	42°	2s	6.7s	5.5s	6.9s	354ms	61.9ms	153ms	0.4ms
7 T		48°		4s	3.3s	6.3s	217ms	29ms	109ms	
7 T	2. nonloc	52°								
	2. DRESS									
7T	3. nonloc		90°	6s	4s	3.3s	6.3s	217ms	29ms	109ms
	3. DRESS									
	3. sLAS.									

Table 6.2: Parameters (flip angle FA, repetition time TR, spin-lattice relaxation T₁, spin-spin relaxation T₂ according to [22] and acquisition delay time TE*/echo time TE) used in the formula of the correction factor. Study 1 = Multicenter study, study 2 = nonloc/DRESS, study 3 = DRESS/semiLASER/nonloc.

Then the absolute concentration of PCr for each spectrum is calculated with γ -ATP resonance as the internal reference, as the β -ATP resonance was influenced by the shape of the excitation pulse:

$$\text{conc_PCr} = \frac{M_{\text{PCr}}}{av_{\text{ATP}}} \cdot \text{conc_ATP} \quad (6.4)$$

whereas av_{ATP} is the averaged value of ATP over the last four minutes measurement time (last 120 data points) in the multicenter study and over the total measurement time in the other two studies. conc_ATP is the assumed constant concentration of ATP in the skeletal muscle [29]:

$$\text{conc_ATP} = 8.2 \text{ mM} \quad (6.5)$$

With averaging 40 seconds, the concentration of PCr at the end of exercise and at the end of recovery (conc_PCr_endex and conc_PCr_endrec respectively) are calculated. With these two values, the drop in concentration can be calculated in mM and %.

The initial rate of PCr synthesis V_{PCr} roughly represents ATP turnover at end of exercise and was calculated according to Schmid et al. [66] as follows:

$$V_{\text{PCr}} = k \cdot (\text{conc_PCr_endrec} - \text{conc_PCr_endex}) \quad (6.6)$$

whereas the rate constant $k = \frac{1}{\tau}$ and τ is obtained from the Curve Fitting Toolbox in MATLAB. The determination of τ in the Curve Fitting Toolbox was carried out with fitting of the PCr time-dependent changes during the recovery period (last 6 minutes of measurement time) to an exponential curve described by the equation [66]:

$$\text{PCr}(t) = \text{PCr_end} \cdot (1 - b \cdot \exp\frac{-t}{\tau}) \quad (6.7)$$

whereas t = time and PCr_end = averaged value of PCr signal intensity at end of measurement (calculated with last 40 seconds).

With the assumption of 15% of total Cr at resting state being not phosphorylated and concluding that 85% of total Cr is phosphorylated at resting state [67], the concentration of Cr can be calculated out of the concentration of PCr at resting state:

$$\text{conc_Cr} = \frac{100 \cdot \text{conc_PCr}}{85} \quad (6.8)$$

The maximum rate of oxidative ATP synthesis Q_{max} [mM/min] (oxidative capacity) of the mitochondrial pool in a muscle is a function of the density and capacity of working mitochondria and the supply of substrate and oxygen, but is independent of muscle mass. Therefore, it is a valuable parameter to evaluate the muscle function. [68] Q_{max} was calculated using the initial rate of PCr synthesis V_{PCr} during the recovery period and the concentration of ADP at the end of exercise conc_ADP_endex [69] [70]:

$$Q_{max} = V_{PCr} \cdot \left(1 + \frac{K_m}{\text{conc_ADP_endex}}\right) \quad (6.9)$$

with the Michaëlis-Menten constant K_m :

$$K_m = 0.03 \text{ mM} \quad (6.10)$$

The concentration of ADP at the end of exercise (conc_ADP_endex) can be calculated as follows [69]:

$$\text{conc_ADP_endex} = \frac{\text{conc_ATP} \cdot \text{conc_Cr_endex}}{\text{conc_PCr_endex}} \cdot H^+ \cdot K_{eq} \quad (6.11)$$

$$H^+ = 10^{-\text{pH_endex}} \quad (6.12)$$

with the apparent equilibrium constant of the CK reaction K_{eq} [71]:

$$K_{eq} = 1660000000 \quad (6.13)$$

and pH_endex as the averaged value of pH at the end of exercise (based on mean of 40 seconds).

The signal-to-noise ratio (SNR) of PCr and linewidth of PCr and Pi, defined as the full width at half maximum (FWHM), were both determined in the frequency domain. Temporal SNR is defined as mean of PCr signal divided by standard deviation of PCr signal, whereas static SNR was calculated with mean of PCr signal divided by standard deviation of noise gained from

residue in jMRUI.

Cramér-Rao lower bounds (CRLB) were determined for the PCr and Pi peak to assess the quality of the spectral fitting. In the multicenter and nonloc/DRESS study CRLB was deduced using the non-localized static spectrum (16 averages), for the DRESS/semi-LASER/nonloc study static spectra of all three localization methods were taken. The glycerophosphoethanolamine (GPE) and glycerophosphocholine (GPC) peaks, two muscular phosphodiesterases (PDE), are combined for calculation of the overall concentration of PDE. The Cramér-Rao lower bound was calculated with following formula:

$$CRLB = \frac{std.ampl.}{ampl.} \quad (6.14)$$

For examination of the existence of a statistical significant difference between two samples, a paired, two-tailed Student's t-test was performed. For a p-value < 0.05 there is a significant difference, whereas for a p-value > 0.05 there is no significant difference between two tested groups.

Results

7.1 Comparison between different magnetic field strengths and ergometers at two institutes

Information on the comparison of the measured dynamic parameters depicted as mean values of all volunteers is given in table 7.1 and 7.2 (for more detailed results see tables A.2, A.3, A.4, A.5, A.6 and A.7 in the appendix).

The comparison of dynamic parameters, when different equipment in two institutes was used, showed significantly higher values in PCr drop and concentration of PCr at the end of recovery ($p < 0.05$ in low and mild workload) in the first institute (see figure 7.1). This results in higher values of V_{PCr} and Q_{max} ($p < 0.05$) at low workload. The pH value at the end of exercise also differs significantly at low workload ($p < 0.05$), but no longer at mild workload ($p = 0.52$). Mitochondrial capacity was found to be increasing with workload in both institutes as seen in figure 7.1.

workload institute	low		mild	
	first	second	first	second
PCr drop [%]	20.38±13.72*	12.09±4.47	32.93±14.81*	22.21±9.96
τ [s]	34.18±8.54	30.51±6.46	41.11±9.89*	30.46±6.59
pH endex	7.05±0.03*	7.09±0.02	7.04±0.04	7.06±0.04
V_{PCr} [mM/s]	0.22±0.13*	0.13±0.05	0.31±0.14	0.24±0.11
Q_{max} [mM/s]	0.46±0.19*	0.32±0.09	0.53±0.17	0.48±0.16
PCr conc. [mM]	35.78±2.99*	33.46±3.52	36.94±3.12*	33.01±3.16

Table 7.1: Dynamic parameters measured in two institutes at 3T using mechanical and pneumatic ergometer. The data are given mean \pm standard deviation. Concentration of PCr measured at end of recovery (last 40 seconds). endex = end of exercise (last 40 seconds); *) $p < 0.05$

workload	low		mild		heavy	
field strength	3T	7T	3T	7T	3T	7T
PCr drop [%]	12.09±4.47	12.30±3.52	22.21±9.96	20.87±7.83	31.23±13.52	28.10±12.72
τ [s]	30.51±6.46	33.37±5.20	30.46±6.59	31.68±7.80	31.27±10.33	30.94±7.28
pH endex	7.09±0.02*	7.07±0.01	7.06±0.04	7.06±0.03	7.04±0.03	7.05±0.02
V_{PCr} [mM/s]	0.13±0.05	0.13±0.04	0.24±0.11	0.23±0.09	0.33±0.09	0.28±0.11
Q_{max} [mM/s]	0.32±0.09	0.31±0.09	0.48±0.16	0.48±0.17	0.58±0.11	0.52±0.11
PCr conc. [mM]	33.46±3.52	33.50±3.41	33.01±3.16	33.38±3.58	32.57±3.22	31.79±2.15

Table 7.2: Dynamic parameters measured in second institute using different magnetic field strenghts. The data are given mean \pm standard deviation. Concentration of PCr measured at end of recovery (last 40 seconds). endex = end of exercise (last 40 seconds); *) p < 0.05

No significant difference was found between 3T and 7T in the second institute in PCr drop ($p = 0.81$, $p = 0.55$ and $p = 0.71$ in low, mild and heavy workload, respectively), τ ($p = 0.08$, $p = 0.47$ and $p = 0.56$ in low, mild and heavy workload, respectively), pH at end of exercise ($p = 0.65$ and $p = 0.92$ in mild and heavy workload, respectively), V_{PCr} ($p = 0.49$, $p = 0.55$ and $p = 0.38$ in low, mild and heavy workload, respectively), Q_{max} ($p = 0.85$, $p = 0.96$ and $p = 0.27$ in low, mild and heavy workload, respectively) and concentration of PCr at end of recovery ($p = 0.97$, $p = 0.75$ and $p = 0.69$ in low, mild and heavy workload, respectively). The only significant difference between 3T and 7T found was the pH measured at the end of exercise with low workload ($p < 0.05$).

Typical time course of the PCr signal at different institutes and magnetic field strengths is shown in figure 7.1. The use of stronger magnetic field (7T against 3T) resulted in increased SNR (static: 655 ± 51 vs. 270 ± 41 , temporal: 111 ± 25 vs. 38 ± 10 , both at rest and mean of all three workloads) and fitting precision (92.9 ± 8.5 vs. 68.6 ± 20.8 , mean of all three workloads) as can also be seen in table 7.4. Temporal and static SNR show lower values at the end of exercise (for more detailed results see tables A.8, A.9, A.10, A.11 and A.12 in the appendix). Table 7.4 also depicts a lower CRLB for PCr than for Pi and a positive correlation of age and concentration of PDE (for more detailed results see table A.13 in the appendix).

Linewidth of PCr and Pi at rest, end of exercise, immediately after exercise and end of recovery, defined as FWHM, for the data sets with generously constrained PCr and Pi linewidths in jMRUI (meaning more than 1 Hz range of linewidth) is shown in table 7.3 (for more detailed results see tables A.15, A.16, A.14, A.18, A.19 and A.17 in the appendix). PCr linewidth shows a small increase from rest to end of exercise followed by a small decrease immediately after exercise and end of recovery. The same maximum at end of exercise can be seen in the linewidth of Pi.

		Rest	End of exercise	Post exercise	End of recovery
PCr	3T 1 st inst.	5.7±1.8	8.5±4.2	7.3±2.7	7.1±2.8
	3T 2 st inst.	9.3±0.8	10.0±0.8	9.7±0.8	9.2±0.7
	7T 2 st inst.	12.3±3.1	13.6±3.2	13.4±2.8	13.3±2.8
Pi	3T 1 st inst.	9.8±3.2	12.2±4.0	11.2±3.8	10.3±3.4
	3T 2 st inst.	13.3±1.5	13.6±3.9	13.6±3.9	13.4±2.5
	7T 2 st inst.	17.4±4.9	18.9±5.3	18.6±4.9	17.6±4.7

Table 7.3: FWHM of PCr and Pi in Hz at rest (mean of 1 minute), at end of exercise (last minute), immediately after exercise (mean of 20 seconds) and at end of recovery (last minute).

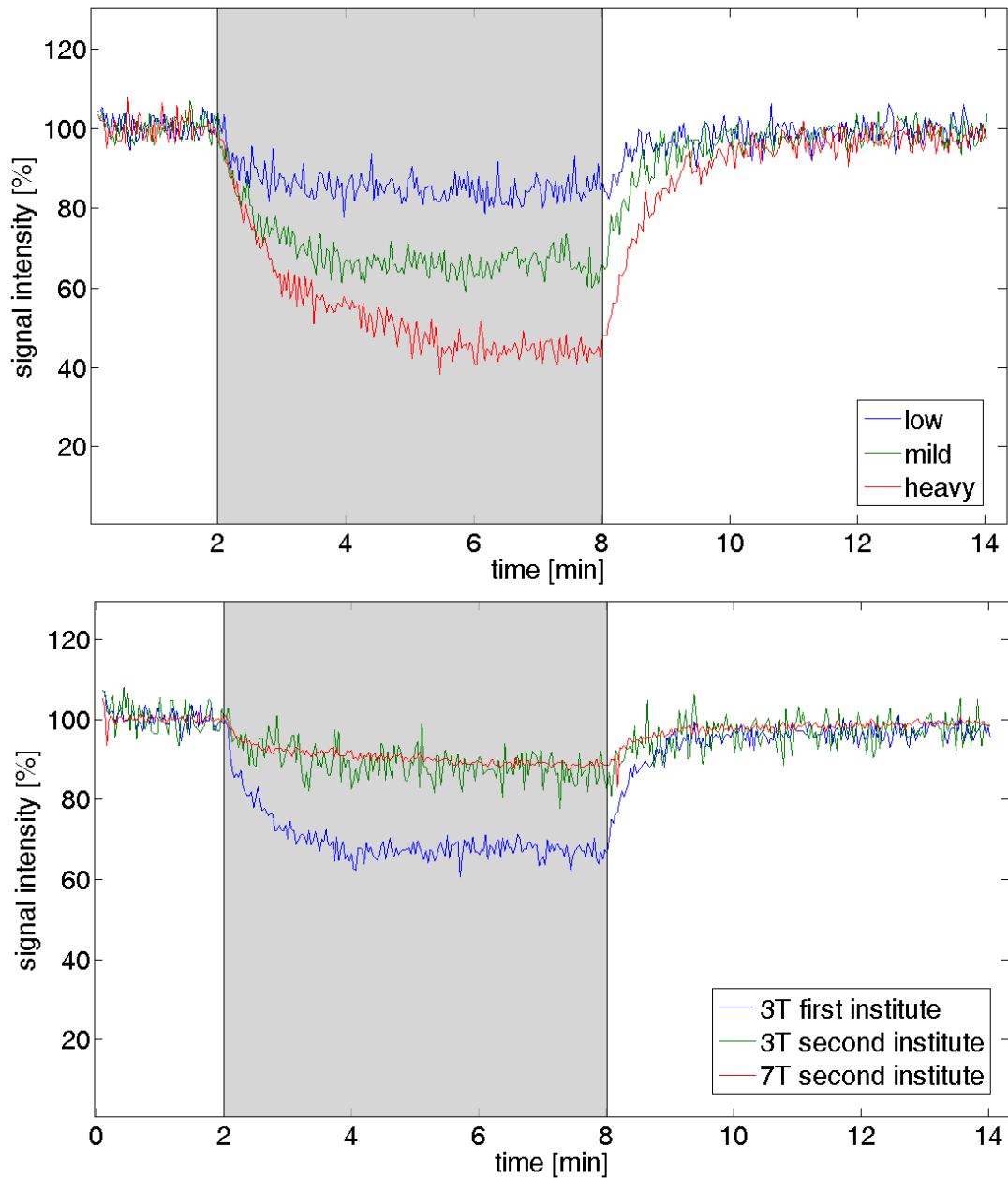


Figure 7.1: Time courses of the PCr signal intensity. The data are normalized to resting PCr signal intensity. The exercise period (6 min) is indicated in gray. Upper picture: PCr signal intensity measured with different workloads at 3T and second institute at the same subject #10. Lower picture: PCr signal intensity measured with 3T at both institutes and 7T in second institute with low workload at the same subject #11.

	3T first institute		3T second institute			7T second institute		
	low	mild	low	mild	heavy	low	mild	heavy
Temporal SNR endex	29±14	22±10	33±10	30±9	24±7	96±30	61±18	62±33
Temporal SNR endrec	47±15	44±13	39±9	36±8	39±12	107±21	117±30	110±24
Static SNR endex	290±52	232±49	245±50	218±44	175±43	559±74	546±60	431±102
Static SNR endrec	355±25	352±29	273±45	262±43	274±35	667±55	630±52	669±45
R-square	73.5±23.6	84.2±14.1	52.3±19.6	69.3±25.2	84.1±17.6	86.8±14.7	95.1±7.2	96.8±3.6
CRLB of PCr	1.07±0.59		1.22±0.38			1.06±0.44		
CRLB of Pi	13.72±7.74		13.92±5.63			15.44±6.86		
conc. of PDE*	1.36		2.84			1.86		
conc. of PDE**	1.80		3.80			2.69		

Table 7.4: Temporal and static SNR at end of recovery (last 4 minutes) and at end of exercise (last 2 minutes), goodness of fit (r-square of tau-fitted curve to original data in percentage), Cramér-Rao lower bounds of PCr and Pi in percentage and age-dependent concentration of PDE. The data are given as mean ± standard deviation. *) = age 20-30 (mean 25.6) **) = age > 30 (mean 47.3)

The sensitivity maps of the used coils are depicted in figure 7.2. The size of the manually selected muscle regions of gastrocnemius medialis, gastrocnemius lateralis and soleus are shown in table 7.5. The selected areas in the data of both institutes are similar in size, only gastrocnemius medialis is chosen slightly bigger in the second institute. The results of the sensitivity maps comparison denoted in table 7.6 show that the flexi coil (11 cm in diameter) of the first institute provides in average more signal from the gastrocnemius medialis.

	first institute			second institute		
	Gastro Lat.	Gastro Med.	Soleus	Gastro Lat.	Gastro Med.	Soleus
1	8.9	12.1	14.7	5.6	11.2	19.8
2	5.3	11.1	27.9	6.8	12.3	21.3
4	5.6	7.3	9.8	6.7	10.8	17.4
10	12.9	16.1	24.3	20.1	19.3	23.5
11	11.2	14.4	15.0	10.4	17.6	14.8
mean	8.8	12.2	18.3	9.9	14.1	19.4

Table 7.5: Size of manually selected muscle regions in cm² (total image size: 324 cm² in the first three data sets of the first institute, 400 cm² in the last two data sets of the first institute and in all data sets in the second institute).

	first institute			second institute		
	Gastro Lat.	Gastro Med.	Soleus	Gastro Lat.	Gastro Med.	Soleus
1	15	20	24	10	9	27
2	8	11	40	12	12	25
4	11	29	28	11	20	29
10	18	17	29	25	17	28
11	16	16	18	15	23	22
mean	14	19	28	15	16	26

Table 7.6: Coil sensitivity maps evaluation: Muscle signal/total signal.

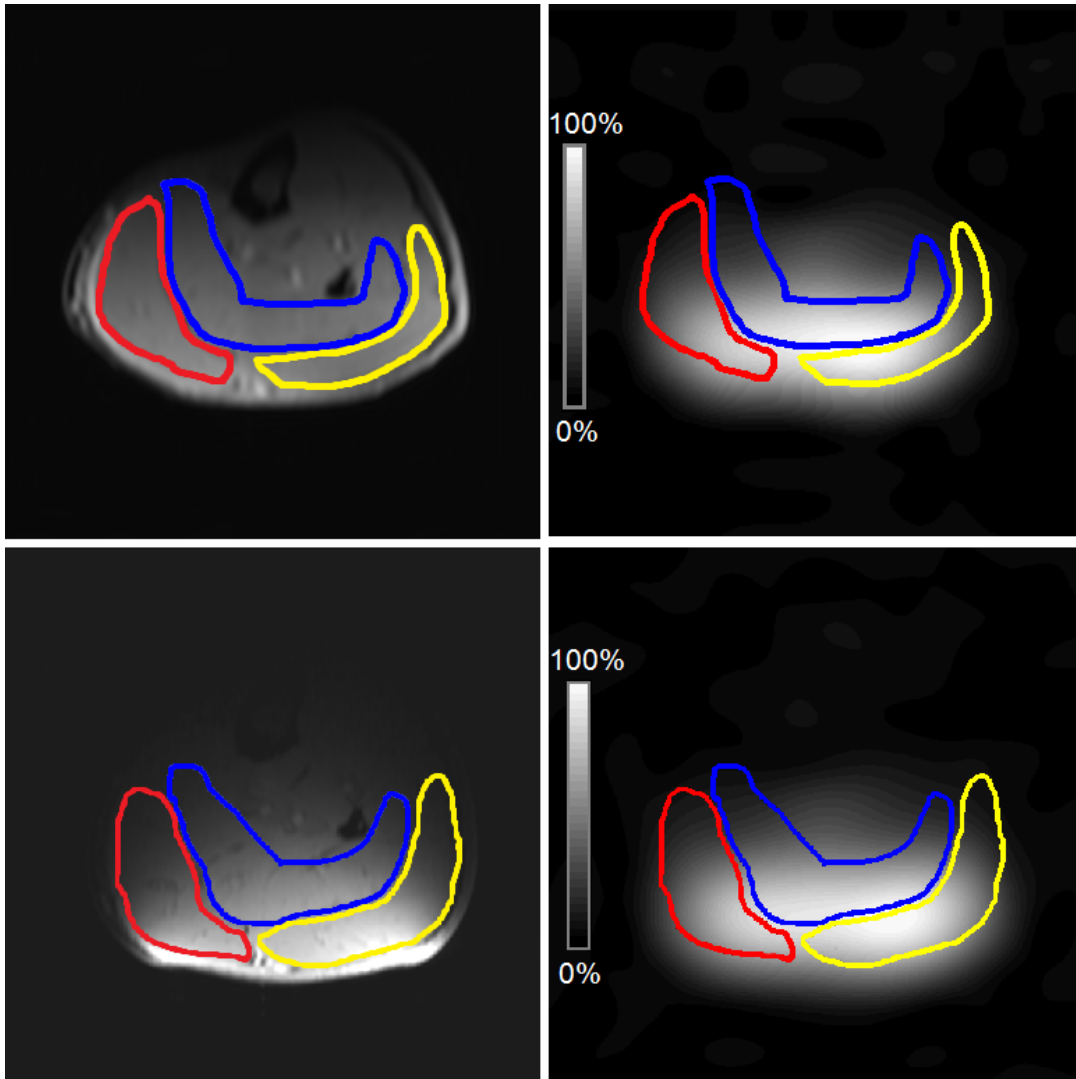


Figure 7.2: Sensitivity map evaluation of both coils used in the same subject (#4). Upper pictures: 11 cm flexi coil (first institute). Lower pictures: 10 cm rigid coil (second institute). Left: ^1H image with manually drawn mask (red: gastrocnemius medialis, yellow: gastrocnemius lateralis, blue: soleus). Right: Signal intensity map of the PCr signal calculated from the acquired 2D ^{31}P CSI.

Figure 7.3 shows the comparison between 1 Hz-constrained and non-constrained γ -ATP curve recorded in the first and second institute. For data of the second institute, non-constraining of the γ -ATP curve was not necessary.

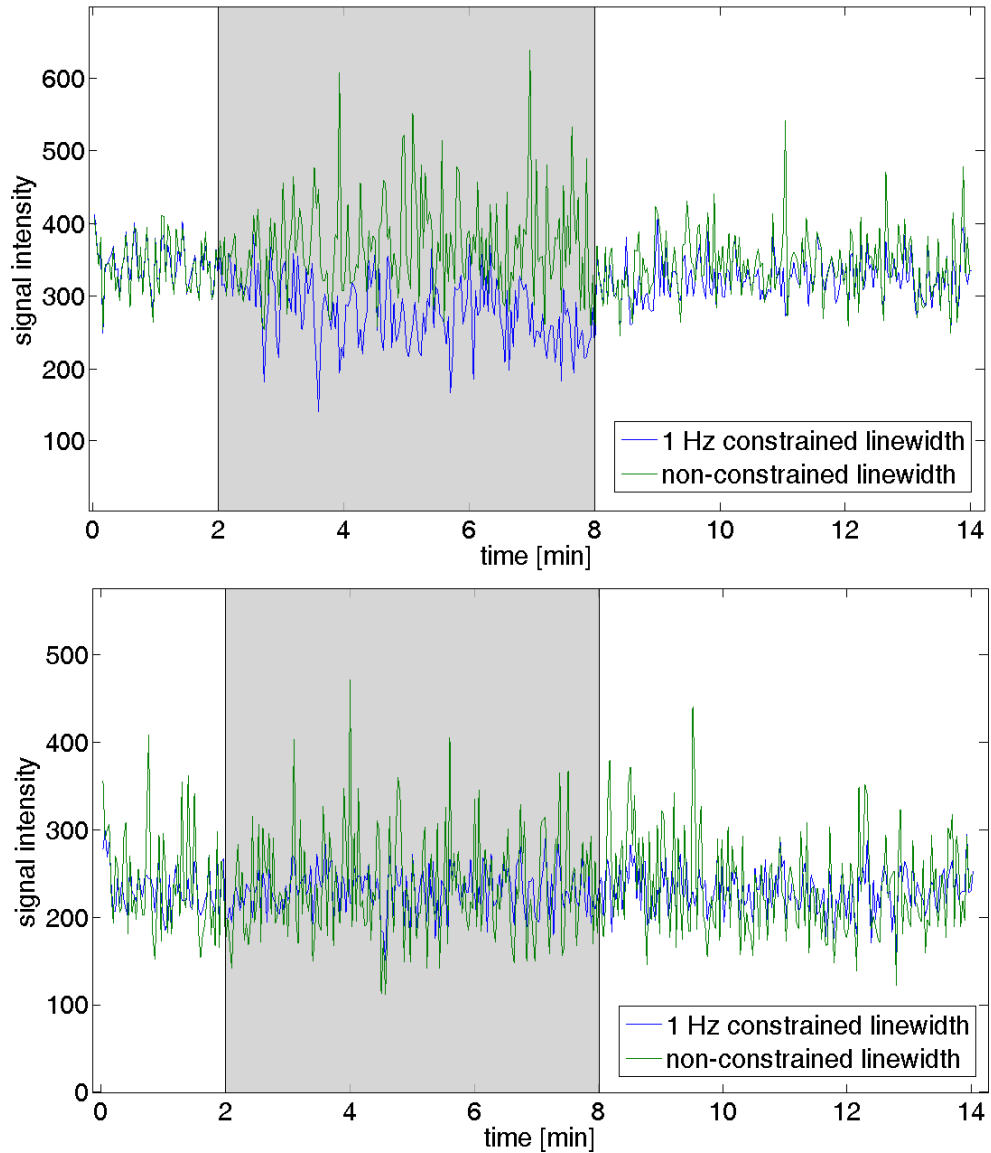


Figure 7.3: γ -ATP curve: The blue line shows the γ -ATP curve with 1 Hz constrained linewidth, the green line shows the γ -ATP curve with non-constrained linewidth. Time between spectra is TR = 2 s. Upper picture: Data from subject #8, first institute, 3T, low workload, first measurement. Lower picture: Data from subject #5, second institute, 3T, mild workload.

7.2 Comparison of non-localized vs. DRESS localization method

Information on the comparison of the measured dynamic parameters depicted as mean values of all volunteers is given in table 7.7 (for more detailed results see table B.2 in the appendix). The relative change in PCr signal intensity is significantly greater in DRESS-localized than non-localized ($p < 0.01$) resulting in significantly higher V_{PCr} ($p < 0.01$). The comparison of τ between non-localized and DRESS-localized does not show a difference. The end of exercise pH_1 shows a tendency to be lower in the localized experiment. The Q_{max} calculated for the DRESS-localized experiment (0.58 ± 0.18 mM/s) was significantly higher ($p < 0.05$) in comparison to non-localized experiment (0.45 ± 0.12 mM/s). There is a trend towards increased concentration of PCr at the end of recovery in the DRESS-localized measurements.

	Non-localized	DRESS-localized	T-Test
PCr drop [%]	34.89 ± 11.16	49.49 ± 21.09	0.01
τ [s]	47.84 ± 14.97	49.78 ± 17.96	0.49
pH endex	pH₁	7.03 ± 0.03	0.06
	pH₂	6.73 ± 0.09	
V_{PCr}[mM/s]	0.27 ± 0.08	0.39 ± 0.17	0.01
Q_{max}[mM/s]	0.45 ± 0.12	0.58 ± 0.18	0.05
PCr conc [mM]	35.12 ± 2.35	37.63 ± 4.56	0.12

Table 7.7: The comparison of the dynamic parameters in non-localized and DRESS-localized experiments: Concentration of PCr measured at end of recovery (last 40 seconds). Both pH values at end of exercise (last 40 seconds) are given for the non-localized experiment; the nonacidifying pH_1 ($n = 14$) and the acidifying pH_2 ($n = 6$); pH_1 is used in the t-test comparison depicted in the last column. The data are given as mean \pm standard deviation.

The time course of the ^{31}P signals during plantar flexion experiments for the non-localized and DRESS-localized measurements is depicted in figure 7.4. The signals of PCr, Pi and ATP were detectable already in single acquisitions and no time averaging was necessary for further analysis. The relative change in PCr signal intensity during non-localized and DRESS-localized experiment is shown in figure 7.5. Higher drop in PCr signal intensity can be seen in DRESS-localized data. Corresponding time course of Pi signal can also be seen. Splitting of the Pi signal was observed in six of the non-localized datasets, but in none of the DRESS-localized data sets.

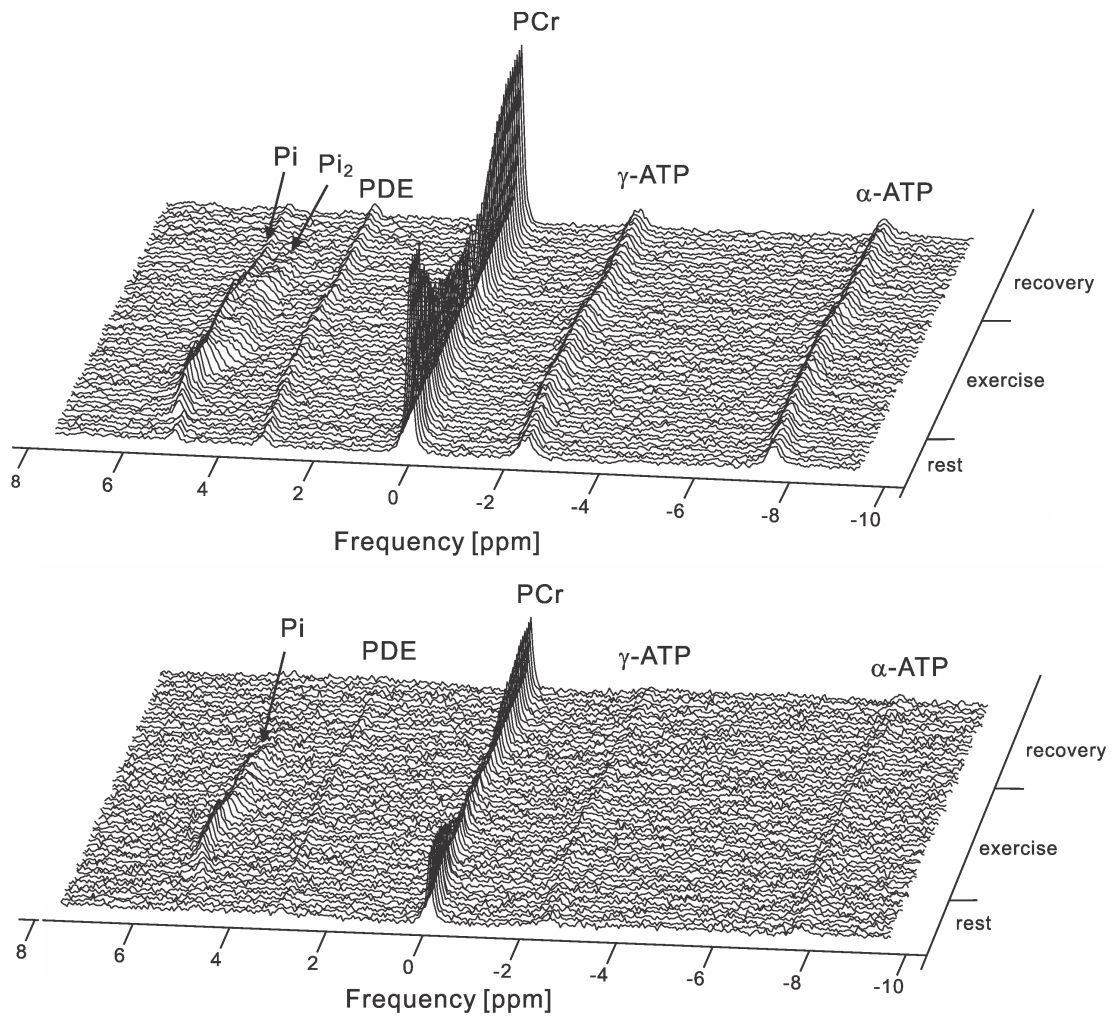


Figure 7.4: Stack plot of the ^{31}P spectra acquired during rest, exercise and subsequent recovery for the non-localized (upper picture) and DRESS-localized acquisition (lower picture). The spectra are scaled equally to show the lower signal intensity of the localized experiment. Note the Pi split in the non-localized data. [58]

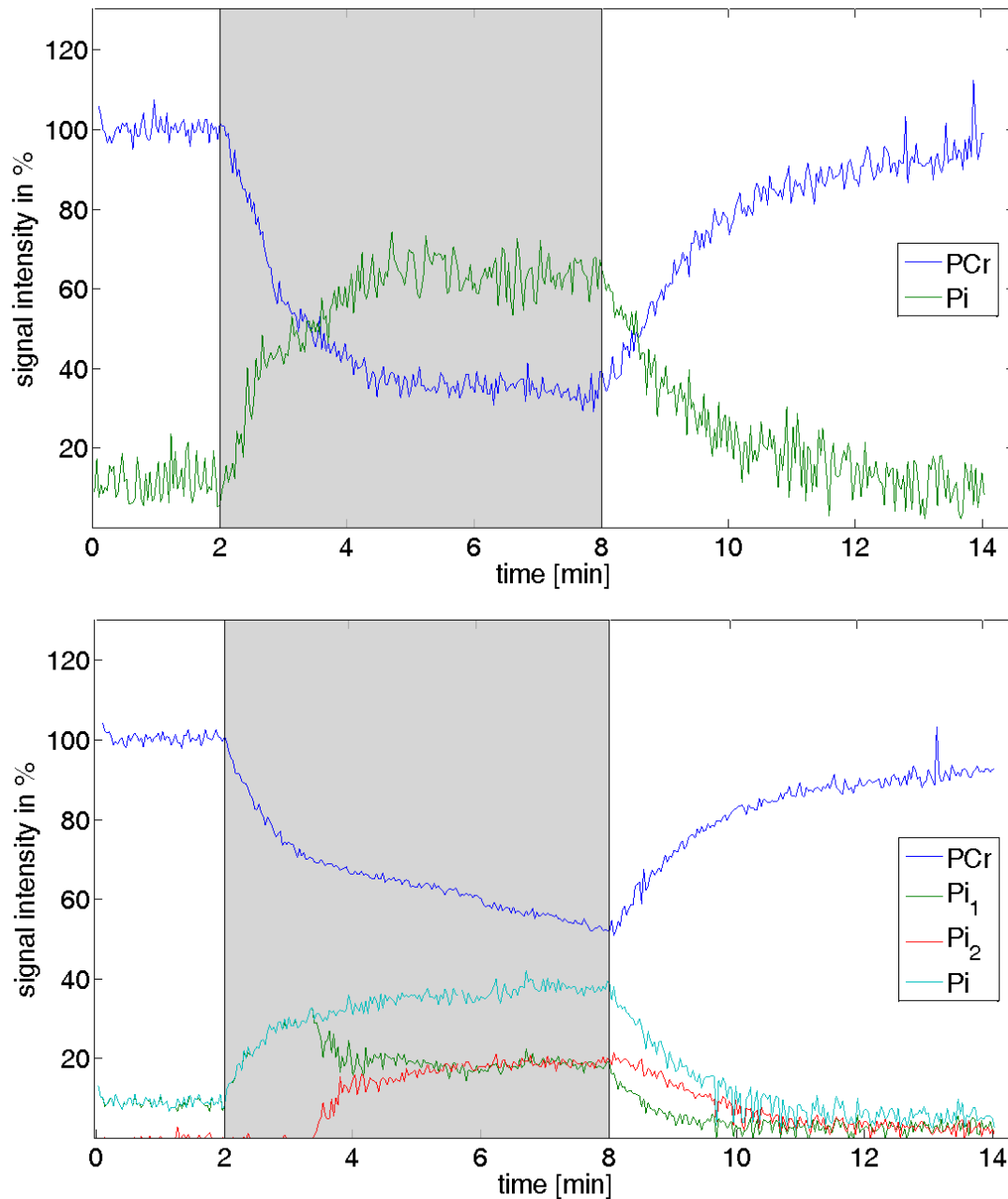


Figure 7.5: Time courses of the PCr and Pi signal intensity measured with DRESS-localization (upper picture) and without localization (lower picture) to the gastrocnemius medialis from the same subject #9. The data are normalized to resting PCr signal intensity. The exercise period (6 min) is indicated in gray. The Pi₂, not found in the DRESS-localized data, becomes distinguishable first after 1-3 minutes of active exercise. The sum of the two fitted Pi peaks is also depicted.

Temporal and static SNR at the end of exercise and end of recovery as well as goodness of fit (r-square) is depicted in table 7.8 (for more detailed results see table B.3 in the appendix). Temporal and static SNR of DRESS is approximately half the value of the non-localized data also seen in figure 7.5. The r-square value of the fitted curves is lower (but still high) for the DRESS-localized data as well. Table 7.8 depicts a reliable quality of the spectral fitting for PCr and Pi (for more detailed results see table B.3 in the appendix).

	non-localized	DRESS-localized
Temporal SNR at end exercise	38±13	17±8
Temporal SNR at end of recovery	66±27	29±10
Static SNR at end of exercise	434±99	172±83
Static SNR at end of recovery	616±69	287±90
R-square	94.3±7.4	90.1±9.5
CRLB of PCr	1.31±0.24	
CRLB of Pi	16.63±3.47	

Table 7.8: Temporal and static SNR at end of recovery (last 4 minutes) and at end of exercise (last 2 minutes), goodness of fit (r-square of tau-fitted curve to original data in percentage) and Cramér-Rao lower bounds of PCr and Pi in percentage. The data are given as mean ± standard deviation.

Linewidth of PCr and Pi at rest, end of exercise, immediately after exercise and end of recovery, defined as FWHM for the data sets with generously constrained PCr and Pi linewidths in jMRUI (meaning more than 1 Hz range of linewidth) is shown in table 7.9 (for more detailed results see table B.4 in the appendix). Linewidth of PCr increases after rest to a slightly bigger value at the end of exercise and immediately after exercise. Similar tendency can be seen in the linewidth of Pi: There is a big change of linewidth at the end of exercise and immediately after exercise compared to rest. In the non-localized data, the linewidth of Pi decreases faster again to its original value at rest than in the DRESS data.

		Rest	Endexercise	Postexercise	Endrecovery
PCr	DRESS	13.2±5.0	14.1±5.2	14.1±5.2	13.8±5.1
	non-loc	16.5±3.2	17.5±3.8	16.8±3.3	15.8±2.5
Pi	DRESS	23.3±4.9	30.±17.0	31.7±16.4	27.8±9.8
	non-loc	22.6±4.5	27.6±7.1	26.5±5.8	22.9±5.3

Table 7.9: FWHM of PCr and Pi in Hz at rest (mean of 1 minute), at end of exercise (last minute), immediately after exercise (mean of 20 seconds) and at end of recovery (last minute).

7.3 Comparison of DRESS vs. semi-LASER localization vs. non-localized method

The size of the voxel of interest (VOI) for semi-LASER was adjusted so as to be constrained to the muscle. VOI dimensions ranged from 31 to 47 cm³, with average dimensions of 3.9 x 1.8 x 5.3 cm = 36.3 cm³ (for more detailed results see table C.2 in the appendix).

Information on the comparison of the measured dynamic parameters depicted as mean values of all volunteers is given in table 7.10 (for more detailed results see table C.3 in the appendix). The relative change in PCr signal intensity is greater in DRESS and semi-LASER localized than non-localized (see figure 7.6). A trend towards lower τ and pH was found in the localized measurement.

	Non-localized	DRESS	semi-LASER
PCr drop [%]	31.23±8.33	43.80±18.29	43.47±21.81
τ[s]	45.18±12.36	44.95±17.17	40.91±9.12
pH endex	7.05±0.04	6.92±0.17	7.00±0.06

Table 7.10: The comparison of the dynamic parameters in non-localized, DRESS and semi-LASER-localized experiments. Mean pH value measured at the end of exercise (last 40 seconds). The data are given as mean \pm standard deviation.

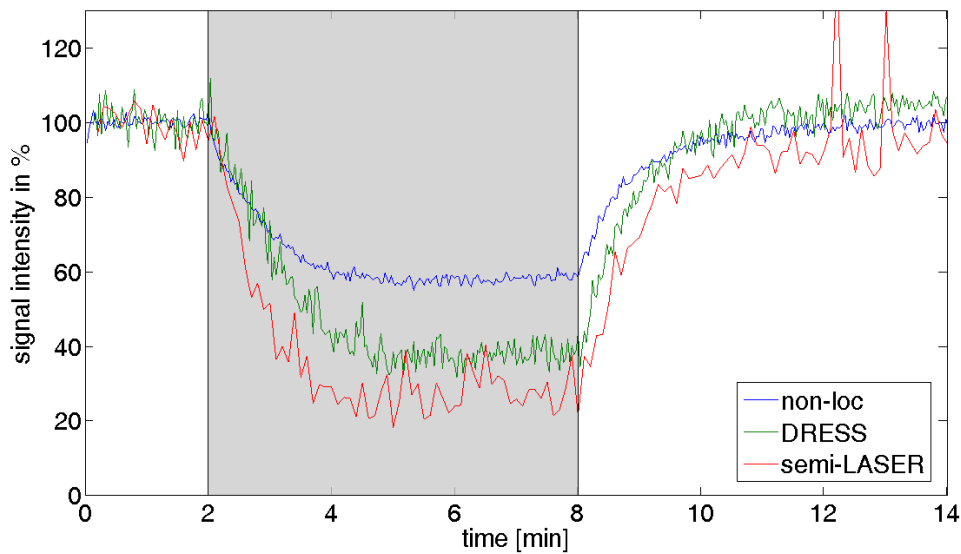


Figure 7.6: Time courses of the PCr signal intensity measured without, DRESS and semi-LASER localization to the gastrocnemius medialis from the same subject #5. The data are normalized to resting PCr signal intensity. The exercise period (6 min) is indicated in gray.

Linewidth of PCr and Pi at rest, end of exercise, immediately after exercise and end of recovery, defined as FWHM is shown in table 7.11 (for more detailed results see table C.4 in the appendix). Linewidth of PCr increases after rest to a slightly bigger value at the end of exercise and immediately after exercise. Similar tendency can be seen in the linewidth of Pi: There is a big change of linewidth at the end of exercise and immediately after exercise compared to rest.

Temporal and static SNR at the end of exercise and end of recovery as well as goodness of fit (r-square) is depicted in table 7.12 (for more detailed results see table C.5 in the appendix). SNR and r-square value is decreased in localized acquisition as can also be seen in figure 7.6.

Table 7.12 depicts a reliable quality of the spectral fitting for PCr in all acquisitions and for Pi in non-localized and DRESS acquisition. The quality of the spectral fitting of the Pi peak for semi-LASER localization is above the reliable border of 25% (for more detailed results see table C.6 in the appendix).

		Rest	Endexercise	Postexercise	Endrecovery
PCr	non-loc	13.9±2.4	15.2±2.1	14.5±2.2	14.1±3.0
	DRESS	15.6±3.7	14.8±2.4	14.6±2.7	13.9±3.2
	semi-LASER	8.4±1.1	8.7±1.3	8.8±1.1	8.4±1.2
Pi	non-loc	24.8±3.1	31.0±12.5	31.6±12.6	23.9±2.5
	DRESS	27.8±7.0	38.9±21.3	38.7±20.0	32.0±13.5
	semi-LASER	17.4±5.6	29.8±15.1	30.6±16.8	22.8±9.6

Table 7.11: FWHM of PCr and Pi in Hz at rest (mean of 1 minute), at end of exercise (last minute), immediately after exercise (mean of 20 seconds) and at end of recovery (last minute).

	Non-localized	DRESS	sLASER
Temporal SNR at end of exercise	50±15	17±8	13±6
Temporal SNR at end of recovery	61±8	37±17	27±11
Static SNR at end of exercise	443±19	187±82	194±139
Static SNR at end of recovery	618±91	317±50	297±90
R-square	93.7±5.9	89.1±14.7	78.1±21.5
CRLB of PCr	1.22±0.12	1.92±0.53	1.11±0.51
CRLB of Pi	20.63±1.81	25.62±4.86	21.84±9.12

Table 7.12: Temporal and static SNR at end of exercise (last 2 minutes) and at end of recovery (last 4 minutes), goodness of fit (r-square of tau-fitted curve to original data in percentage) and Cramér-Rao lower bounds of PCr and Pi in percentage. The data are given as mean ± standard deviation.

Discussion

8.1 Comparative multicenter study between different magnetic field strengths and ergometers

In this study, parameters of muscle metabolism measured by dynamic ^{31}P -MRS under different experimental conditions were compared. Measurements were performed using two ergometers, two coils and three MR systems (2x3T & 1x7T) in the same study population at three different workloads.

It has been shown, that the first exercise bout potentially alters the parameters measured in the following bouts if strong acidification is present and too short time between bouts for relaxation is provided [72]. The chosen workloads at 0.5 Hz frequency used in our study are not that strenuous what can be seen also on the relatively high end exercise pHs of 7.07 ± 0.02 , 7.05 ± 0.04 and 7.05 ± 0.03 in low, mild and heavy workload respectively. Forbes et al. [73] showed that the influence of previous exercise on intracellular H^+ became undetectable after 15 min of rest, used also in this study for the muscle recovery period between mild and low workload. For the period between low and heavy workload 10 min of rest was sufficient.

Mechanical and pneumatic ergometer in combination with different coils were compared at 3T and the influence of magnetic field strength (3T vs. 7T) was tested with the same ergometer and similar coil. As the same healthy volunteers were measured in a short time without life-style interactions, physiological changes in metabolism were unlikely and our study reflects the influence of used experimental equipment and exercise intensity on the calculated metabolic parameters. Non-localized acquisition was used for its simplicity, robustness and wide-spread use. Higher magnetic field strength improves the data quality, increasing the reliability, but no significant differences between metabolic parameters were found in this respect. On the other hand, different equipment used was found to have significant influence on the results, especially in exercise at low workloads.

In general, the values achieved can be compared to previous studies: Kemp et al. [74] state that their results of PCr concentration at rest of 33 ± 2 mM are close to the overall mean values of

ten published studies on calf muscle. These results are in agreement with ours (36 ± 2 mM and 33 ± 3 mM in first and second institute, respectively).

Trends in metabolic parameters in relation to workload observed in the study are in good agreement with literature [75] [76]. Previous reports on repeated knee-extension exercise [77] show a PCr depletion of $20 \pm 8\%$ and $30 \pm 8\%$, time constant τ of 36.1 ± 13.5 s and 33.9 ± 12.7 s, V_{PCr} of 0.19 ± 0.09 mM/s and 0.26 ± 0.06 mM/s and Q_{max} of 0.35 ± 0.18 mM/s and 0.46 ± 0.13 mM/s at mild and heavy workload, respectively, which shows good agreement with the results of this study, involving calf muscle exercise (PCr depletion $22 \pm 9\%$ and $30 \pm 13\%$, time constant τ 31.1 ± 7.2 s and 31.1 ± 8.8 s, V_{PCr} 0.24 ± 0.10 mM/s and 0.31 ± 0.10 mM/s and Q_{max} 0.48 ± 0.17 mM/s and 0.55 ± 0.11 mM/s at mild and heavy workload in second institute). Layec et al. [77] stated also high reproducibility of the non-localized ^{31}P -MRS even in examination one year apart, justifying the time delay (one month) between measurements performed in this study at the two institutions. Small intra-subject variability can be explained by low relative reliability obtained from Layec et al. at rest from surface-coil-localized ^{31}P -MRS spectra. ^{31}P -MRS cannot be considered to be sensitive enough to detect changes at rest in a homogenous population. Furthermore, Layec et al. observed increase in PCr depletion, V_{PCr} and Q_{max} between mild and heavy exercise with higher reliability of the results at heavy workload. This is in consistence with our data where mean values of PCr drop, V_{PCr} and Q_{max} measured on all three MR systems also differ between workloads. Exercises with moderate work rates, used in this study, are characterized by a linear relationship between PCr breakdown and workload as well as steady-state conditions for PCr hydrolysis (oxidative phosphorylation can supply all ATP needs), whereas exercises with heavy work rates show a non linear relationship. The beginning of constant-load exercises bases on PCr and anaerobic glycolysis covering the initial period of muscle activity until the blood supply and the mitochondrial metabolism are adapted. This initial period is regarded as oxygen deficit which magnitude is directly related to the exercise workload. It is primarily reflected in the extent of PCr hydrolysis and the accumulation of lactate. The blood flow increases at onset of the exercises and reaches a plateau level during constant dynamic exercise, that is dependent on the workload. These results are in line with the findings of PCr drop, as the extend of workload corresponds to the plateau level of PCr hydrolysis. [75] But for maximum exercise oxidative phosphorylation will be stimulated to its maximum limit although PCr can partially buffer significant declines in ATP. At the maximum limit of oxidative phosphorylation, the higher drop of PCr and the slower return of PCr (resulting in a greater τ) to the rest values should cancel each other out in the ideal case, so that V_{PCr} and Q_{max} are equal with different workloads. Once the limit of oxidative phosphorylation is exceeded far beyond what could possibly be supported by even maximal oxidative phosphorylation, anaerobic glycolysis provides the ATP needs, resulting in a decrease of pH due to the lactating character of this reaction. [78] The extent of intracellular acidosis reached at the end of exercise determines the rate of PCr resynthesis [77] [79] [80] [81]. In the data of this master thesis the difference in Q_{max} between low and mild workload is even more pronounced in comparison to the difference between mild and heavy workload, showing that the use of higher workload better reveals the real mitochondrial capacity. As the pH tends to decrease at high workloads, special care was taken not to allow the muscle acidification and the assumption can be made that the exercise was performed under aerobic conditions.

Cramér-Rao lower bounds for PCr and Pi were determined to assess the quality of the spectral fitting which is widely used in magnetic resonance spectroscopy [82]. Reliable results are obtained with $CRLB < 20\%$ [83] which could be achieved for the PCr and Pi peak. The CRLB values are in the range of published data of the calf muscle [18].

Table 7.4 shows a positive correlation of PDE concentrations and age of the subjects. This is in agreement with [84] [85]. Szendroedi et al. [84] investigated the relationship of muscular PDE in middle-aged patients with or without type 2 diabetes mellitus and in young non-diabetic humans. Szendroedi et al. stated that body mass and glycemia mainly determine the positive correlation of PDE with resting mitochondrial activity, insulin resistance and age.

The calculated temporal SNR depicts the change of SNR over time, that increases after exercise, since the PCr signal decreases during exercise. Static SNR is defined as mean PCr signal divided by standard deviation of noise, i.e., depicting information about the overall noise character of the coil. After exercise, static SNR logically increases as well.

Temporal and static SNR show approximately twice to three times the values for 7T in comparison to 3T. This is in accordance to Bogner et al. [22] who measured a doubling in SNR of PCr when jumping from 3T to 7T. The decrease of T_1 , with which the paper deals, leads to an additional increase in SNR per unit time. Together, this translates to a possible increase in SNR per unit time of up to +150%. This improvement in SNR resulted into better data fitting and therefore more reliable calculation of mitochondrial capacity. However, lower accuracy of the 3T MR system did not cause any differences in calculated τ (31 ± 6 s, 30 ± 7 s and 31 ± 10 s vs. 33 ± 5 s, 32 ± 8 s and 31 ± 7 s), V_{PCr} (0.13 ± 0.05 mM/s, 0.24 ± 0.11 mM/s and 0.33 ± 0.09 mM/s vs. 0.13 ± 0.04 mM/s, 0.23 ± 0.09 mM/s and 0.28 ± 0.11 mM/s) and Q_{max} (0.32 ± 0.09 mM/s, 0.48 ± 0.16 mM/s and 0.58 ± 0.11 mM/s vs. 0.31 ± 0.09 mM/s, 0.48 ± 0.17 mM/s and 0.52 ± 0.11 mM/s) between 3T and 7T (low, mild and heavy workload) respectively. PCr concentration has been estimated with the popular approach of using the concentration ratio PCr/ATP with ATP concentration as an internal standard. The justification for this is the relatively small variation in ATP concentration between individuals and the lack of difference among different muscle fibre types (e.g., soleus has 80% slow twitch fibres whereas gastrocnemius muscle has 50% slow twitch fibres) [74]. This was a good choice since there is no variation of PCr concentration between the data of the second institute. However, significantly higher values of PCr concentration were found in the first institute compared to the results from the second institute. In combination with significantly increased PCr depletion, these differences caused also significantly higher values of V_{PCr} and Q_{max} , however only at the lowest workload, where the reproducibility is lower [77].

The increased concentration of PCr in the first institute is probably caused by difference in the used surface coil. Although both coils were from the same manufacturer, the flexible construction and 1 cm extra in diameter (11 cm vs. 10 cm) of the phosphorus channel can cause a difference in the sensitivity volume of the coil from the first institute. The measured sensitivity maps confirm the assumption of different detection volumes between the coils. Even though the size of the manually selected muscle regions do not differ between the facilities for gastrocnemius lateralis and soleus and is even greater for gastrocnemius medialis in the second institute (inflexi coil), the sensitivity maps show that the flexi coil provides better coverage of the calf and therefore in average more signal from the gastrocnemius medialis and soleus muscles. The concentration

of PCr is higher in gastrocnemius medialis [86] [87] and as it is the most active muscle during plantar flexion [36], this difference in sensitivity can be at least partly responsible for the differences in measured PCr concentration and depletion. However, also imperfectly reproduced measurement position can contribute to these differences and has to be considered as a limitation of the current study.

The mentioned higher PCr depletion in the first institution could have been caused also by different construction of the pedal. Although care was taken to set similar pedal resistance in both institutes, greater range of pedal movement of the mechanical ergometer possible probably caused higher overall work done. While the pneumatic ergometer enables rotation in the ankle axis, resulting in a more natural pressing of the pedal and less motion artifacts, the home-made ergometer has its axis of rotation underneath the ankle inducing a more complex motion, possibly leading to higher PCr depletion. Due to the different rotation axis to the ankle, the physical work and, therefore, the PCr drop is greater in the ergometer of the first institute.

PCr drop is directly related to V_{PCr} and Q_{max} which can be seen in the significant difference between both institutes with low workload (no significant difference with mild workload due to the dependence of pH). The significant difference in PCr drop may also have an impact on τ , as can be seen in the significant difference with mild workload.

Due to the constant concentration of ATP in the skeletal muscle in accordance to literature [29], the jMRUI evaluation of the spectra took place with a ± 1 Hz constrained linewidth of the ATP peak. In a few data sets from the first institute it could be found that this limitation influences the results. The underestimation of ATP resulted in an overestimation of the concentration of PCr and, therefore, also in an overestimation of V_{PCr} and Q_{max} . The changes in measured ATP signal intensity during exercise are caused by motion artefacts during exercise and could be found only in the first institute's but not in the second institute's data. An explanation for this could be the differences in both ergometers and overall leg movement described above. The change in signal intensity of ATP is the reason why average ATP signal is calculated with the averaged value of ATP signal over the last four minutes measurement time in the multicenter study but with the total measurement time in the other two studies. Also for the few data sets of the first institute, where a motion artifact could be found in the ATP signal, the jMRUI evaluation of the spectra was done with non-constrained linewidth of the ATP peak.

Linewidth of PCr and Pi defined as FWHM was calculated at rest (first minute), at end of exercise (last minute), immediately after exercise (mean of 20 seconds) and at end of recovery (last minute). The time period for mean calculation are chosen according to Meyerspeer et al. [36]. In general, the data shows a greater value of linewidth in 7T than in 3T. This is in accordance with literature (see chapter 2.10). PCr and Pi linewidth increases during exercise, decreases slightly immediately after exercise and stays approximately at the same or a slightly smaller value until end of recovery. Even though PCr linewidth during exercise has a big variability due to motion, the mean values of the PCr linewidth still shows a maximum at the end of exercise. This can be explained with the myoglobin oxygenation as explained in chapter 3.6. Exercise-induced linewidth decrease of intramyocellular PCr on cessation of exercise can only be seen tententially in the data. This is in agreement with [36]: The difference between the postexercise linewidth and recovery is far less pronounced in nonlocalized spectra (than localized data) which contain larger fractions of resting tissue and have a larger linewidth due to stronger B_0

inhomogeneities across the large sensitive volume. The increase of Pi linewidth during exercise can be explained with the change of intracellular pH according to [40]. Schmid et al. found a strong link between mitochondrial function, cellular energy metabolism, acid-base equilibrium and T_2^* during exercise and recovery (see chapter 3.6).

Besides the already mentioned imperfect repositioning of the surface coil, there are other subject-related limitations. Fixed values of workload were taken instead of setting the workload levels according to individual's MVC, leading to intra-subject differences in PCr depletion. However, the differences in metabolic parameters in dependence of workload are analysed and intra-subject variability was not subject of this study. Another anatomical limitation of our study includes the working muscles in plantar flexion, which can differ between subjects. Since similar data from other literature measured with non-localized acquisition have identical limitation, it can be neglected.

8.2 Comparative study of non-localized vs. DRESS localization method

In this study, the usability of a DRESS sequence for *in vivo* determination of localized mitochondrial capacity in gastrocnemius medialis muscle by dynamic ^{31}P -MRS at 7T was investigated. The DRESS-localized data were compared with non-localized MRS with the same time resolution (2 s) and same workload. Significant differences in PCr depletion, end exercise pH, as well as initial PCr resynthesis were found. In addition, exercise-induced splitting of the Pi peak was observed only in the non-localized data. The FID acquisition of the slice-selective DRESS localization method allowed for quantification of ATP resonances and, therefore, calculation of the maximal oxidative flux in gastrocnemius medialis muscle, which was found significantly higher when compared to the non-localized acquisition.

The comparison of the two acquisition strategies was performed within one session of repeated plantar flexion exercise. To eliminate the influence of previous exercise on intracellular H^+ , 15 min of muscle recovery period was chosen, even though the workload of 25% MVC at 0.5 Hz frequency used in our study is not that strenuous, what can be seen also on the relatively high end exercise pHs of 7.03 ± 0.03 (6.73 ± 0.09) and 6.95 ± 0.12 , in non-localized (pH_2) and localized experiment respectively. Nevertheless, even though the workload was relatively low and the 15 min of rest should provide enough time for full recovery, the order of DRESS-localized and non-localized exercise bouts in the present study was randomized, avoiding any residual influence of examination order on the comparison of the results.

Dynamic ^{31}P -MRS has been often used without localization, but recent studies have shown that muscle recruitment during plantar flexion exercise is not uniform [40] and may even vary between subjects [88]. Investigations of the heterogeneity of PCr dynamic in the calf muscles, either by spectrally selective MRI [89] [90] or gated MRSI protocol [91] reported higher PCr signal drops in the medial gastrocnemius in comparison to soleus. The results of this study are in good agreement with these reports as the data from gastrocnemius medialis muscle, as acquired by DRESS-localization, show significantly higher PCr depletion ($49.5\% \pm 21.1\%$) to the non-localized acquisition data ($34.9\% \pm 11.1\%$) which consist of a mixture of signals from several muscles (i.e., gastrocnemius medialis, gastrocnemius lateralis and soleus). Moreover, a signifi-

cantly higher initial recovery rate of PCr (0.39 ± 0.17 mM/s vs. 0.27 ± 0.08 mM/s) in localized acquisition can be reported. This is in good agreement with the recent study by Meyerspeer et al. [36], where data acquisition by a single-voxel, semi-LASER sequence were compared to a non-localized data acquisition.

A trend towards shorter recovery rate time constants in the localized measurements (only active muscles contribute to τ) as found by Meyerspeer et al. [36] could not be found in this study.

FID-acquisition of the DRESS sequence allows measurement and quantification of fast relaxing metabolites and spin systems undergoing J modulation (e.g., ATP), what is not possible with refocusing techniques (semi-LASER) requiring relatively long TE [46]. Therefore, the ATP signal can be directly used for absolute quantification of the metabolite concentrations and no additional external reference standards measurements are needed. According to Takahashi et al. [92] PCr and Pi concentration of muscles show a strong positive correlation with the content of type II fibers. Rzanny et al. [93] observed higher PCr and Pi concentrations for the medial part of gastrocnemius compared to the lateral part possibly caused by fiber distribution. Commonly, both parts of gastrocnemius exhibit nearly the same content of type I and II fibers, whereas soleus is predominantly composed of type I fibers. This should amount to only a 5% difference in PCr concentration and no difference in ATP concentration. [74] The trend towards increased PCr concentration in the localized acquisition, where gastrocnemius medialis solely was measured, could be caused by this effect. Nevertheless, this trend is not significant as in non-localized acquisition soleus is not measured alone but together with gastrocnemius medialis. The trend towards increased PCr concentration in gastrocnemius medialis (35.1 ± 2.4 mM in soleus and 37.6 ± 4.6 mM in gastrocnemius medialis) can also be explained with the paper of Valkovič et al. [87]. In the paper gradient offset independent adiabaticity-based 1D-ISIS¹ localization was tested comparing soleus with gastrocnemius medialis. A significant difference of PCr concentration was found between the muscle groups (31.2 ± 2.2 mM in soleus and 33.9 ± 1.2 mM in gastrocnemius medialis).

The information about metabolite concentrations can be consecutively used for calculation of maximal oxidative flux. This was found to be significantly higher in the localized experiment (0.58 ± 0.18 mM/s) when compared to the non-localized data (0.45 ± 0.12 mM/s). This is caused by the already mentioned increased initial recovery rate of PCr and due to the decreased pH at end of exercise in the localized data. Due to the pH-dependence of various processes contributing to net H⁺ efflux in muscle, higher rates are seen for the localized data, where pH changes during exercise are larger than for pH₁, the nonacidifying pH in the nonlocalized data as described by Meyerspeer et al. [36]. The active gastrocnemius medialis muscle contributes to the pH signal gained from the localized data, whereas also soleus and gastrocnemius lateralis, less active muscles, contribute to the pH₁ signal gained from the non-localized data. The pH for the more acidic moiety of the non-localized acquisition (pH₂) is smaller than the pH of the DRESS-localized acquisition in agreement with the results from Meyerspeer et al. [36].

The high temporal resolution of the current study (2 s) is higher than previous reports using semi-LASER approach (6 s) [46] [36] because the DRESS sequence is less demanding on the SAR and, therefore, shorter TR can be used at 7T. The gated MRSI protocol also allows high temporal resolution [91], but for acquisition of larger matrix sizes, long measurement time would be

¹one-dimensional image-selected in vivo spectroscopy

needed. The reduction in TR results in an optimal excitation angle lower than 90° , what can be also beneficial in the presence of inhomogeneous B_1 field, as the variability of the flip angles is lower for smaller excitation angles [94].

Cramér-Rao lower bounds for PCr and Pi were determined to assess the quality of the spectral fitting which is widely used in magnetic resonance spectroscopy [82]. Reliable results are obtained with $CRLB < 20\%$ [83] which could be achieved for the PCr and Pi peak. The CRLB values are in the range of published data of the calf muscle [18].

As a consequence of the smaller volume in DRESS-localized acquisition, lower SNR is expected for localized measurements. In this study, approximately half as much SNR with localized spectroscopy could be observed in comparison with non-localized spectroscopy. Consequently, the goodness of fit is also smaller in DRESS-localized acquisition.

With localized ^{31}P -MRS, a distinct decrease of PCr and Pi linewidth from an elevated value at the end and immediately after exercise toward the resting value is observed. This can be explained with the myoglobin oxygenation as explained in chapter 3.6. The statement of Meyerspeer et al. [36] that the difference between the postexercise and recovery linewidth of PCr is far less pronounced in nonlocalized spectra, could not be found in this study, probably caused by the large intersubject variability and low workload. The increase of Pi linewidth during exercise can be explained with the change of intracellular pH according to [40] (see chapter 3.6). The faster decline of Pi linewidth in the non-localized data can be explained by the contribution of passive muscle parts to the signal in which the intracellular pH has not changed during exercise. Meyerspeer et al. [36] observed splitting of the Pi resonance in the non-localized data only. Similar observation could be done in the present study, when only one Pi peak was observed in the DRESS-localized data while in six non-localized datasets two Pi peaks were visible, proving good localization performance of the DRESS sequence. No Pi compartmentation within one muscle group, as suggested in the literature [56] [95], was observed in this study. Although spatial selection only in one direction is used, this is sufficient for superficial muscles (e.g., gastrocnemius). For spatial selection of deeper muscle groups (e.g., soleus), the semi-LASER approach would be still beneficial. Slab selective localization was previously suggested and successfully tested at 2T by Walter et al. [96] using 1D-ISIS. This approach allows also FID acquisition and has low chemical shift displacement error (CSDE), however the ISIS subtraction scheme is prone to motion artifacts and the need of two acquisitions decreases the time resolution. In addition, the use of narrow selection slabs and short excitation pulse in our DRESS approach decreases the CSDE to a comparable level [18].

8.3 Comparative study of DRESS vs. semi-LASER localization vs. non-localized method

In this study, semi-LASER sequence for *in vivo* determination of localized mitochondrial capacity in gastrocnemius medialis muscle was compared with DRESS sequence and non-localized acquisition by dynamic ^{31}P -MRS at 7T. A trend towards greater PCr depletion, smaller τ and smaller pH could be found in both localized acquisition. The FID acquisition of the slice-selective DRESS localization method allowed for quantification of ATP resonances whereas single-voxel semi-LASER localization does not allow adequate quantification of ATP reso-

nances. Therefore, no comparison of maximal oxidative flux in gastrocnemius medialis muscle was done.

The acquisition of the three localization methods was performed within one session of repeated plantar flexion exercise in random order. Similar to the other studies performed in this master thesis, 15 min of muscle recovery period were chosen, to eliminate the influence of previous exercise on intracellular H^+ .

The application of semi-LASER has the advantage of alleviating the effects of the inhomogeneous amplitude of the radio frequency field B_1 of a simple loop coil. A second advantage is the better defined (3D) volume of interest detected in semi-LASER compared to DRESS-localization. However, the applicable RF power is restricted due to technical limitations of the coil as well as due to SAR limits which results in a temporal resolution of 6 sec instead of 2 sec used in DRESS and non-localization. The consequence of increased TE is smaller signal intensity, already lowered by the small region of interest. The relatively long TE of semi-LASER is mainly a disadvantage for the detection of metabolites with short T_2 or spin systems undergoing J modulation, such as ATP. Meyerspeer et al. [46] calculated the losses due to T_1 and T_2 relaxation measured with semi-LASER (TR = 6 s and minimum TE = 23 ms): The γ -ATP signal is decreased by 45% due to T_2 relaxation in addition to T_1 saturation to a level of 84%. The main source of signal loss is J-evolution, a decrease of signal amplitude to 27%, which adds up to a total of only 10% of visible ATP signal. In accordance to Meyerspeer et al. the calculated values for the initial rate of PCr resynthesis and maximal oxidative flux include a large systematic error due to the assumption of ATP sustaining a constant concentration and large random error resulting from ATP quantification from low SNR data acquired by accumulating spectra. Therefore, the focus is on PCr and Pi quantification, where reliable results could be found.

Heterogeneity of PCr dynamic in the calf muscle could be investigated, as the signal from gastrocnemius medialis muscle acquired by DRESS and semi-LASER localization shows higher PCr depletion than non-localized acquisition. This is in accordance with literature [89] [90] [91] where higher PCr signal drop is reported in the medial gastrocnemius in comparison to soleus. Small variation in PCr drop between DRESS and semi-LASER localized data is caused by the different size and location of volume of interest and the signal consisting of different amounts of muscle fibres. In subject #5 even the DRESS-localized acquisition shows two Pi peaks. This measurement was therefore repeated with a great care taken on the slab positioning. As the two Pi peaks were reproductively visible, the possibility of wrong slab positioning was excluded. The explanation for this phenomenon is probably the different muscle fibre composition within gastrocnemius medialis causing two different intracellular pH values and Pi peaks.

Similar to the data from Meyerspeer et al. [36] a trend towards lower τ value as well as a decreased value of pH at end of exercise could be found in the localized data. Since the working muscle gastrocnemius is the only muscle contributing to the signal in DRESS and semi-LASER, the recovery is faster and pH changes during exercise are larger than for pH_1 , the nonacidifying pH in the non-localized data. The change of pH in semi-LASER compared to non-localized data is less discernible due to the worse spectral fitting of the Pi peak in the dynamic measurements. Reliable results of CRLB of the static spectra (CLRB < 25% [97] [98]) could be obtained for Pi and PCr peak with all three localization methods. For one subject, in the semi-LASER data no detection of the Pi peak was possible.

Linewidth of PCr shows smaller values for semi-LASER results than for DRESS or non-localized data which is in agreement with literature [36]. However, there is only a trend towards a distinct decrease of PCr linewidth from an elevated value immediately after exercise toward the resting value in semi-LASER data, as described by Meyerspeer et al. This is caused by larger inter-subject variability and low number of subjects for this study. Linewidth of Pi is also slightly decreased for semi-LASER data. The elevated values at the end of exercise and immediately after exercise can be seen more clearly in the case of Pi. As already described in chapter 3.6, this is known to change due to intracellular pH changes.

Even though the signal intensity is always bigger in DRESS than semi-LASER, static SNR is smaller in DRESS acquisition in some cases due to the increased standard deviation of noise. This is caused by the positioning of the slice, being outside of the muscle for some parts of the slice. In general, the increased specificity of localized MRS comes at the cost of lower SNR per unit time, which may in turn necessitate temporal averaging, thus resulting in low temporal resolution. At lower field strengths a comparison of localized vs. non-localized acquisition is difficult due to the limited SNR per unit time. The increased SNR and reduction of the T_1 relaxation times of ^{31}P metabolites at 7T [22] provide the conditions to record reliable data with a temporal resolution higher than the typical changes to be observed. A temporal resolution on the order of seconds are required, since the dynamics in MR signals during exercise and recovery occur with half times on the order of minutes and below. This gap between temporal resolution and dynamic, localized MRS has narrowed nowadays with the introduction of ultra-high field whole-body MR scanners. [36] [46]

Conclusion

In this master thesis, the impact of magnetic field strength, ergometer construction, RF coil diameter, workload and localization method on the metabolic parameters measured by dynamic ^{31}P -MRS in soleus and gastrocnemius muscle during plantar flexion was investigated. To address all of the risen questions, three individual studies were conducted.

The first study was dedicated to define the impact of ergometer design, surface coil diameter, magnetic field strength and different exercise workloads on measured parameters of muscle metabolism. The results show that several factors have to be considered in determination of mitochondrial capacity. It was shown that there is an influence of ergometer construction and surface coil type on metabolic parameters measured by ^{31}P -MRS. For multicenter studies it is also important to set the same workload and use similar measurement and evaluation protocols. It was shown that more intensive exercise provides more reliable results which are directly comparable between research sites. Furthermore, it was found that the strength of the magnetic field, although increasing data quality, does not significantly affect the determination of Q_{\max} .

Slab-selective localization of DRESS sequence was compared to non-localized acquisition in the second study. DRESS showed good spatial selection and provided muscle specific insight into oxidative metabolism even at relatively low exercise load (25% of MVC). Significant differences in PCr depletion, end of exercise pH, initial rate of PCr resynthesis and maximal oxidative flux as well as a trend towards shorter recovery rate time constants in the localized measurements was found. A splitting of the Pi resonance was observed only in the non-localized data, as they consist of a mixture of signals from several muscles.

The third study compared DRESS vs. semi-LASER localization in relation to non-localized acquisition. Heterogeneity of PCr dynamic in the calf muscle could be investigated, as the signal from gastrocnemius medialis muscle acquired by DRESS and semi-LASER localization shows higher PCr depletion, smaller τ and smaller pH than in non-localized acquisition. However, unlike the DRESS sequence, the semi-LASER does not allow adequate quantification of ATP resonances and, therefore, no comparison of the specific maximal oxidative flux in gastrocnemius medialis could be carried out. The lower SNR, that comes with the increased specificity of localized MRS, was still acceptable due to the use of an ultra-high MR system.

Bibliography

- [1] D. E. Kelley et al. Dysfunction of mitochondria in human skeletal muscle in type 2 diabetes. *Diabetes*, 51:2944–2950, 2002.
- [2] M.F. Schocke et al. High-energy phosphate metabolism during calf ergometry in patients with isolated aorto-iliac artery stenoses. *Invest Radiol*, 41(12):874–882, 2006.
- [3] R. Esterhammer. Phosphocreatine kinetics in the calf muscle of patients with bilateral symptomatic peripheral arterial disease during exhaustive incremental exercise. *Mol Imaging Biol*, 10(19):30–39, 2008.
- [4] B. Quistorff et al. Some quantitative aspects of ³¹P magnetic resonance spectroscopy *in vivo* in an exercise physiology context. *Proceedings of the 2nd WSEAS International Conference on BIOMEDICAL ELECTRONICS and BIOMEDICAL INFORMATICS*, pages 154–160, 2009.
- [5] de Graaf Robin A. *in vivo NMR Spectroscopy - 2nd Edition Principles and Techniques*. John Wiley & Sons, Ltd, 2007.
- [6] Deyle Gail Dean et al. The role of MRI in musculoskeletal practice: a clinical perspective. *Journal of Manual & Manipulative Therapy*, 19(3):152–161, 2011.
- [7] Constantine Godwin et al. Role of MRI in clinical cardiology. *The Lancet*, 363 Issue 9427:2162–2171, 2004.
- [8] Reddy J. Jagan Mohan et al. *Step by Step MRI*. Jaypee Brothers Medical Publishers (P) Ltd., 2005.
- [9] Weishaupt D. *Wie funktioniert MRI?* Springer, 2009.
- [10] Schneider Frank. *Funktionelle MRT in Psychiatrie und Neurologie*. Springer, 2007.
- [11] Scheffel Hans et al. *Praxisbuch MRT Abdomen und Becken*. Springer, 2012.
- [12] Adamek Henning E. *MRT in der Gastroenterologie: MRT und bildgebende Differenzialdiagnose*. Georg Thieme Verlag, 2010.
- [13] Moore James et al. *Biomedical Technology and Devices Handbook*. CRC Press LLC, 2004.

- [14] Bernstein Matt A. *Handbook of MRI: Pulse Sequences*. Elsevier, 2004.
- [15] Alberto Tannus et al. Adiabatic Pulses. *NMR in Biomedicine*, 10:423–434, 1997.
- [16] Richard Bitar et al. MR Pulse Sequences: What Every Radiologist Wants to Know but Is Afraid to Ask. *RadioGraphics*, 26(2):513–537, 2006.
- [17] Magnetic Resonance Technology Information Portal. *Pulse Sequence*. <http://www.mr-tip.com/serv1.php>.
- [18] Marek Chmelik et al. Fully Adiabatic 31P 2D-CSI with Reduced Chemical Shift Displacement Error at 7 T - GOIA-1D-ISIS/2D-CSI. *Magnetic Resonance in Medicine*, 69(5):1233–1244, 2013.
- [19] Jeffrey Brown et al. MR Spectroscopy of the Heart. *American Journal of Roentgenology*, 155:1–11, July 1990.
- [20] Mudry Karen M. et al. *Principles and Applications in Engineering Series: Biomedical Imaging*. CRC Press, 200.
- [21] Kuperman Vadim. *Magnetic Resonance Imaging: Physical Principles and Applications*. Academic Press, Inc, 2000.
- [22] Wolfgang Bogner et al. Assessment of 31P Relaxation Times in the Human Calf Muscle: A Comparison between 3 T and 7 T *in Vivo*. *Magnetic Resonance in Medicine*, 62:574–582, 2009.
- [23] Rolf Gruetter. *Neural Metabolism In Vivo*. Springer, 2012.
- [24] Bronzino Joseph Daniel. *The Biomedical Engineering Handbook. Volume 2. The Electrical Engineering Handbook Series*. CRC Press, 2000 New York, Boca Raton.
- [25] Chris Boesch et al. Magnetresonanz-Spektroskopie *in vivo*. *Labor und Medizin*, 24:245–253, 1997.
- [26] Webb S. *The Physics of Medical Imaging*. Taylor & Francis Group, 1988.
- [27] Reed Rob. *Practical Skills in Biomolecular Sciences*. Pearson Education Limited, 2007.
- [28] Mosby. *Mosby's Medical Dictionary, 8th edition*. Elsevier, 2009.
- [29] DJ Taylor et al. Energetics of human muscle: exercise-induced ATP depletion. *Magnetic Resonance in Medicine*, 3(1):44–54, 1986.
- [30] Nabors Murray W. *Botanik*. Pearson Studium, 2007.
- [31] Klinke Rainer et al. *Physiologie*. Thieme, 2009.
- [32] Koolman Jan et al. *Taschenatlas der Biochemie*. Thieme, 2003.

- [33] Luzi Livio. *Cellular Physiology and Metabolism of Physical Exercise*. Springer, 2012.
- [34] Hideyuki Takahashi et al. Control of the rate of phosphocreatine resynthesis after exercise in trained and untrained human quadriceps muscles. *European Journal of Applied Physiology*, 71:396–404, 1995.
- [35] Ladislav Valkovič et al. Interrelation of 31P-MRS metabolism measurements in resting and exercised quadriceps muscle of overweight-to-obese sedentary individuals. *NMR in Biomedicine*, 26:1714–1722, 2013.
- [36] Martin Meyerspeer et al. Comparing Localized and Nonlocalized Dynamic 31P Magnetic Resonance Spectroscopy in Exercising Muscle at 7 T. *Magnetic Resonance in Medicine*, 68:1713–1723, 2012.
- [37] Patrick W. Stroman. *Essentials of Function MRI*. CRC Press, 2011.
- [38] Gustav Andreisek et al. T2*-Weighted and Arterial Spin Labeling MRI of Calf Muscle in Healthy Volunteers and Patients with Chronic Exertional Compartment Syndrome: Preliminary Experience. *American Journal of Roentgenology*, 193(4):327–333, 2009.
- [39] Juliet Varghese et al. Exercise induced changes in T1, T2 relaxation times and blood flow in the lower extremities in healthy subjects. *Journal of Cardiovascular Magnetic Resonance*, 15(1):108, 2013.
- [40] Albert Ingo Schmid et al. Exercising calf muscle T2* changes correlate with pH, PCr recovery and maximum oxidative phosphorylation. *NMR in Biomedicine*, Early View (Online Version of Record published before inclusion in an issue), 2014.
- [41] R. Garth Kidd. *NMR of Newly Accessible Nuclei, Volume 1 Chemical and Biochemical Applications*. Academic Press, Inc, 1983.
- [42] Reich Hans J. *Relaxation in NMR Spectroscopy*. <http://www.chem.wisc.edu/areas/reich/nmr/08-tech-01-relax.htm>. University of Wisconsin.
- [43] Bruch Martha D. *Practical Spectroscopy Series: NMR spectroscopy techniques/ edited by MarSpectroscopy*, volume 21. Marcel Dekker, Inc., 1996.
- [44] Pohost Gerald M. *Handbook of Cardiovascular Magnetic Resonance Imaging*. Informa Healthcare USA, 2007.
- [45] Stagg J. Charlotte et al. *Magnetic Resonance Spectroscopy-Tools for Neuroscience Research and Emerging Clinical Applications*. Elsevier Inc., 2014.
- [46] Martin Meyerspeer et al. Semi-LASER Localized Dynamic 31P Magnetic Resonance Spectroscopy in Exercising Muscle at Ultra-High Magnetic Field. *Magnetic Resonance in Medicine*, 65:1207–1215, 2011.
- [47] Paul A. Bottomley et al. Depth-resolved surface-coil spectroscopy (DRESS) for *in Vivo* 1H, 31P, and 13C NMR. *Journal of Magnetic Resonance*, 59(2):338–342, 1984.

- [48] Bottomley. Method of Imaging by Depth-Resolved Surface Coil Spectroscopy, 1986.
- [49] Jean-Pierre Mattei et al. A tool for diagnostic purposes and pathophysiological insights in muscle. *Reumatismo*, 56(1):9–14, 2004.
- [50] T. Yoshida et al. Phosphocreatine resynthesis during recovery in different muscles of the exercising leg by 31P-MRS. *Scandinavian Journal of Medicine and Science in Sports*, 23:313–319, 2013.
- [51] Jean-Pierre Mattei et al. New parameters reducing the interindividual variability of metabolic changes during muscle contraction in human: A 31P MRS study with physiological and clinical implications. *Biochimica et Biophysica Acta*, 1554:129–136, 2002.
- [52] KK McCully et al. Relationships between *in vivo* and *in vitro* measurements of metabolism in young and old human calf muscles. *Journal of Applied Physiology*, 75(2):813–819, 1993.
- [53] Martin Meyerspeer et al. Dynamic interleaved 1H/31P STEAM MRS at 3 Tesla using a pneumatic force-controlled plantar flexion exercise rig. *MAGMA*, 18(5):257–262, 2005.
- [54] A. Gussew et al. Improved reproducibility of dynamic 31P-MRS in the calf muscle during exercise by self-adjusted muscle activity. *Biomed Tech*, 57(1), 2012.
- [55] Maria Pia Francescato et al. Two-Pedal Ergometer for *In Vivo* MRS Studies of Human Calf Muscles. *Magnetic Resonance Medicine*, 46:1000–1005, 2001.
- [56] K. Vandeborne et al. Metabolic heterogeneity in human calf muscle during maximal exercise. *Proc Natl Acad Sci U S A*, 88(13):5714–5718, 1991.
- [57] R. Bottinelli et al. Human skeletal muscle fibres: molecular and function diversity. *Prog Biophys Mol Biol*, 73(2-4):195–262, 2000.
- [58] Ladislav Valkovič et al. DRESS-localized dynamic 31P-MRS of the exercising human gastrocnemius muscle at 7T. *Conference Abstract for the International Society for Magnetic Resonance in Medicine*, 2014.
- [59] Floota Fighting Chronic Pain. Calf Muscles. http://www.floota.com/muscles_of_the_calf.html, 2011.
- [60] Carmine D. Clemente. *Clemente's Anatomy Dissector: Guides to Individual Dissections in Human Anatomy with Brief Relevant Clinical Notes*. Lippincott Williams & Wilkins, 2010.
- [61] Neeta V. Kulkarni. *Clinical Anatomy (A Problem Solving Approach)*. Jaypee Brothers Medical Publishers (P) Ltd., 2012.
- [62] G. Layec. Accurate work-rate measurements during *in vivo* MRS studies of exercising human quadriceps. *Magn. Reson. Mater. Phys. Biol. Med.*, 21(3):227–235, 2008.

- [63] Magnetic Resonance Technology Information Portal. *Specific Absorption Rate*. <http://www.mr-tip.com/serv1.php>.
- [64] L. Vanhamme et al. Improved method for accurate and efficient quantification of MRS data with use of prior knowledge. *Journal of Magnetic Resonance*, 129:35–43, 1997.
- [65] Richard B. Moon et al. Determination of intracellular pH by 31P Magnetic Resonance. *The Journal of Biological Chemistry*, 248:7276–7278, 1973.
- [66] Albrecht I. Schmid. Comparison of Measuring Energy Metabolism by Different 31P-Magnetic Resonance Spectroscopy Techniques in Resting, Ischemic, and Exercising Muscle. *Magnetic Resonance in Medicine*, 67:898–905, 2012.
- [67] M. Boska et al. ATP Production-Rates as a Function of Force Level in Human Gastrocnemius Soleus Using 31-P MRS. *Magnetic Resonance in Medicine*, 32(1):1–10, 1994.
- [68] Jeanine J. Prompers et al. Dynamic MRS and MRI of skeletal muscle function and biomechanics. *NMR in Biomedicine*, 19:927–953, 2006.
- [69] Teresa M Sinnwell. et al. Metabolic Abnormalities in Skeletal Muscle of Patients Receiving Zidovudine Therapy Observed by 31P *In Vivo* Magnetic Resonance Spectroscopy. *The Journal of Clinical Investigations*, 96:126–131, 1995.
- [70] G.J. Kemp et al. Quantitative Analysis by 31P Magnetic Resonance Spectroscopy of Abnormal Mitochondrial Oxidation in Skeletal Muscle during Recovery from Exercise. *NMR in Biomedicine*, 6:302–310, 1993.
- [71] J.W. Randolph Lawson et al. Effects of pH and Free Mg²⁺ on the Keq of the Creatine Kinase Reaction and Other Phosphate Hydrolyses and Phosphate Transfer Reactions. *The Journal of Biological Chemistry*, 254, No.14, Issue of July 25:6528–6537, 1979.
- [72] T. Yoshida et al. Changes in intracellular pH during repeated exercise. *Eur J Appl Physiol Occup Physiol*, 67(3):274–278, 1993.
- [73] S.C. Forbes et al. Effects of recovery time on phosphocreatine kinetics during repeated bouts of heavy-intensity exercise. *Eur J Appl Physiol*, 103(6):65–675, 2008.
- [74] Graham J. Kemp et al. Review Article: Absolute quantification of phosphorus metabolite concentrations in human muscle *in vivo* by 31P MRS: a quantitative review. *NMR in Biomedicine*, 20:555–565, 2007.
- [75] Michael F.H. Schocke et al. High-energy phosphate metabolism during incremental calf exercise in human measured by 31 phosphorus magnetic resonance spectroscopy (31P MRS). *Magnetic Resonance Imaging*, 22:109–115, 2004.
- [76] T. Binzoni et al. Phosphocreatine hydrolysis by 31P-NMR at the onset of constant-load exercise in humans. *J. Appl Physiol.*, 73(4):1644–1649, 1992.

- [77] Gwenael Layec. Reproducibility Assessment of Metabolic Variables Characterizing Muscle Energetics *In Vivo*: A 31P-MRS Study. *Magnetic Resonance in Medicine*, 62:840–854, 2009.
- [78] 136-139. *Biochemistry Primer for Exercise Science. Human Kinetics*. Tiidus M. Peter et al., 2012.
- [79] David Bendahan et al. Heterogeneity of metabolic response to muscular exercise in humans: New criteria of invariance defined by *in vivo* phosphorus-31 NMR spectroscopy. *FEBS Journal*, 272, number 1,2:155–158, 1990.
- [80] S. Iotti et al. *In Vivo* Assessment of Mitochondrial Function in Human Gastrocnemius Muscle by 31P MRS. *NMR in Biomedicine*, 6:248–253, 1993.
- [81] Nicole M.A. van den Broek et a. Intersubject differences in the effect of acidosis on phosphocreatine recovery kinetics in muscle after exercise are due to differences in proton efflux rates. *American Journal of Physiology: Cell Physiology*, 293:C228–C237, 2007.
- [82] S. Cavassila et al. Cramer-Rao bounds: an evaluation tool for quantitation. *NMR in Biomedicine*, 14:278–283, 2001.
- [83] E. Malucelli et al. The role of pH on the thermodynamics and kinetics of muscle biochemistry: An *in vivo* study by 31P-MRS in patients with myo-phosphorylase deficiency. *Biochimica et Biophysica Acta*, 1807:1244–1249, 2011.
- [84] Julia Szendroedi. Skeletal Muscle Phosphodiester Content Relates to Body Mass and Glycemic Control. *PLOS ONE*, 2011.
- [85] J. Satrustegui et al. An *in vivo* phosphorus nuclear magnetic resonance study of the variations with age in the phosphodiester content of human muscle. *Mechanisms of Ageing and Development*, 42(2):105–114, 1988.
- [86] R. Rzanny et al. 31P-MRS investigations of training effects on resting state concentrations of phosphor metabolite in the m. gastrocnemicus. *Proc. Intl. Soc. Mag. Reson. Med.*, 17:2395, 2009.
- [87] Ladislav Valkovič et al. One-Dimensional Image-Selected *In Vivo* Spectroscopy Localized Phosphorus Saturation Transfer at 7T. *Magnetic Resonance in Medicine*, DOI 10.1002/nmrm.25058, 2014.
- [88] F. Kogan et al. Method for high-resolution imaging of creatine *in vivo* using chemical exchange saturation transfer. *Magn. Reson. Med.*, 72(1):164–172, 2014.
- [89] P. Parasoglou et al. Dynamic three-dimensional imaging of phosphocreatine recovery kinetics in the human lower leg muscles at 3T and 7T: a preliminary study. *NMR in Biomedicine*, 26(3):348–356, 2013.

- [90] P. Parasoglou et al. Rapid 3D-imaging of phosphocreatine recovery kinetics in the human lower leg muscles with compressed sensing. *Magn. Reson. Med.*, 68(6):1738–1746, 2012.
- [91] S.C. Forbes et al. Comparison of oxidative capacity among leg muscles in humans using gated 31P 2-D chemical shift imaging. *NMR in Biomedicine*, 22(10):1063–1071, 2009.
- [92] H. Takahashi et al. Relationships between fiber composition and NMR measurements in human skeletal muscle. *NMR in Biomedicine*, 9(1):8–12, 1996.
- [93] R. Rzanny et al. Monitoring training-induced metabolic adaptations in the M. gastrocnemius of volleyball players by 31P-MRS. *Intl Federation for Medical and Biological Engineering*, Proceedings 25/IV:453–456, 2009.
- [94] M. Chmelik et al. Flip-angle mapping of 31P coils by steady-state MR spectroscopy imaging. *J Magn Reson Imaging*, DOI 10.1002/jmri.24401, 2014.
- [95] H.E. Kan et al. *In vivo* 31P MRS detection of an alkaline inorganic phosphate pool with short T1 in human resting skeletal muscle. *NMR in Biomedicine*, 23(8):995–1000, 2010.
- [96] G. Walter et al. Noninvasive measurement of phosphocreatine recovery kinetics in single human muscles. *Am J Physiol*, 272(2 Pt 1):C525–534, 1997.
- [97] Da Shi et al. Longitudinal *in vivo* development changes of metabolite in the hippocampus of *Fmr1* knockout mice. *Journal of Neurochemistry*, 123:971–981, 2012.
- [98] A. Hock et al. Extended metabolite profile of the human spinal cord. *21st Annual Meeting and Exhibition of the International Society for Magnetic Resonance in medicine (ISMRS2013)*, Salt Lake City, UT, USA, 2013.

List of Figures

2.1	(A) The nuclear spin energy for a spin-1/2 nucleus as a function of the external magnetic field strength B_0 . (B) The lower energy level (α spin state) corresponds to magnetic moments parallel with B_0 , while spins in the higher energy level (β spin state) have an antiparallel alignment with B_0 . [5]	6
2.2	(A) A nuclear spin precessing in an external magnetic field B_0 . The spin magnetic moment μ precesses about B_0 , in which the orientation θ and the amplitude (along z) μ_z are quantized. (B) In a macroscopic ensemble of nuclear spin-1/2, the spins distribute themselves among two possible orientations according to the Boltzmann equation. [5]	7
2.3	(A) After a RF pulse M_0 rotates back in its thermal equilibrium. The magnetization vector can be described by a helix. The transverse component M_{xy} produces measurable electromagnetic radiation. (B) Gray bar represents the RF-pulse; the so generated MR-signal (measurable with a coil perpendicular to the z axis) is called “free induction decay“ (FID) and is an exponential damped oscillation. [10]	9
2.4	Decomposition of a linear oscillating magnetic field (A) into two rotating magnetic fields (B) with frequencies $-\omega$ and ω , respectively. [5]	10
2.5	Magnetic field vectors encountered in the rotating frame of reference $x'y'z'$ during excitation. (A) On-resonance: The effective, external magnetic field vector equals the magnetic field vector B_1 along x' . The longitudinal magnetization experiences a torque and will rotate towards the transverse plane through an angle θ . (B) Off-resonance: the frequency of the magnetic field B_1 no longer equals the Larmor frequency, resulting in an additional magnetic field vector $\Delta\omega/\gamma$ along z' . The effective magnetic field B_e then equals the vector sum of B_1 and $\Delta\omega/\gamma$. The longitudinal magnetization will experience a torque from this effective field, resulting in a more complex rotation about B_e . [5]	12
2.6	Relation between optimal Ernst angle (in degrees) and the ratio of repetition time TR to the T_1 relaxation time. [5]	16
2.7	Inversion recovery method for determination of T_1 relaxation time: (A) After 180° excitation, longitudinal magnetization relaxes back to its thermal equilibrium value with a T_1 relaxation time constant. Excitation of this signal at different time points results in spectra representing a discrete sampling of the T_1 recovery curve. (B) Fitting of the results of (A) with equation 2.48. Zero-crossing of the longitudinal magnetization at time t_{null} , given by $T_1 \ln 2$, provides a crude estimate of T_1 . [5]	17

2.8	The free induction decay occurring after the initial 90° excitation exhibits rapid signal loss via T_2^* dephasing. The 180° pulse leads to a formation of the spin-echo whose amplitude is restored. The amplitude at echo time TE is attenuated by T_2 decay mechanism. [13]	18
2.9	(A) After the excitation, (B) the spins dephase in the transverse plane during the first half of TE due to B_0 magnetic field inhomogeneity and frequency offsets. (C) The refocusing 180° pulse mirrors all magnetization vectors along the y axis and the spins rephase during the second half of TE due to the same B_0 magnetic field inhomogeneity and frequency offsets. (D) At the echo time TE the rephasing is complete and a spin-echo is formed. The signal has decayed due to T_2 relaxation. [5]	19
2.10	Spin echo method for determination of T_2 relaxation: (A) NMR spectra obtained at different echo times. (B) Fitting of the results of (A) with equation 2.50. [5]	19
3.1	Spin-spin interactions involved with scalar coupling. (A) Isolated atoms: The Fermi contact energetically favors antiparallel orientation between nuclear and electronic spins. (B) Chemical bonds: The Pauli principle demands that the electron spin are in an antiparallel orientation thereby potentially forcing nuclear and electron spins in an energetically higher parallel orientation (depending on the nuclear spin state). [5]	25
3.2	(A) Energy level diagram for two isolated carbon-13 and proton nuclei: Two carbon-13 transitions with the same frequency ν_C and two proton transitions with the same frequency ν_H giving rise to singlet resonances in the carbon-13 and proton NMR spectra, respectively. (B) Energy level diagram for a $^{13}C - ^1H$ 'molecule' with a covalent bond between the carbon-13 and proton nuclei (nuclear spins affect each other through the bonding electrons). The $\alpha\alpha$ and $\beta\beta$ spin state (i.e. the nuclear spin for both ^{13}C and 1H is in the α and β state, respectively) becomes energetically less favorable as one of the two nuclear-electronic spin orientations is forced to be parallel, whereas in the $\alpha\beta$ and $\beta\alpha$ spin states all spin orientations can be antiparallel. The same energy-level perturbations now give rise to two carbon-13 transitions with different frequencies $\nu_C + J/2$ and $\nu_C - J/2$ and two protons transitions with different frequencies $\nu_H + J/2$ and $\nu_H - J/2$. [5]	26
3.3	Scalar coupling between carbon-13 and proton nuclei leads to a splitting of the singlet resonances into so-called doublet resonances. The resonances at the lower and higher frequencies are associated with energy level transitions, in which the nuclear spin of the scalar-coupling partner is in the α and β spin-state, respectively. [5]	27

3.4	Typical <i>in vivo</i> ^{31}P NMR spectrum from a skeletal muscle at 1.5 Tesla (PME = phosphomonoester, Pi = anorganic phosphate, PDE = phosphodiester, PCr = phosphocreatine, ATP = adenosine triphosphate). Intracellular pH can be calculated with the difference of frequency between PCr and Pi. The ATP molecule consists of atoms with three different chemical environments resulting in three different chemical shifts α , β and γ . The γ -ATP peak may also include contribution from β -adenosine diphosphate (ADP) nuclei, and the α -ATP peak may include contributions from α -ADP nuclei together with nicotinamide adenine dinucleotide (NAD) and nicotinamide adenine dinucleotide phosphate (NADP). The three ATP peaks are sometimes referred to as nucleotide triphosphates (NTP). In this spectrum, the spin-spin splitting of the γ and α ATP peaks into doublets and the β ATP peak into a triplet can be seen. [25] [26]	29
3.5	Chemical structure of ATP. [5]	30
3.6	Time course of the ^{31}P spectra during rest, exercise and subsequent recovery. [35] .	32
4.1	Pulse sequence for 3D LASER localization: A nonselective excitation is applied using the adiabatic pulse BIR-4, while refocusing is performed with three pairs of AFP pulses, each selecting an orthogonal spatial slice, thereby defining a 3D volume. Magnetic field crusher gradients surrounding the AFP pulses ensure removal of all unwanted coherences from outside the localized volume. The echo-time TE is defined from the end of the BIR-4 pulse to the beginning of acquisition. [5]	36
4.2	Examples of adiabatic pulses: (a) AFP (b) BIR-1 and (c) BIR-4. [15]	37
4.3	DRESS pulse sequence: A linear B_0 gradient, leading to excitation of spins in a plane parallel to the surface coil, followed by a frequency-selective RF pulse (90°). [43] 38	38
6.1	1: Calf muscles, 2: Medial condyle of the femur, 3: Lateral condyle of the femur, 4: Gastrocnemius, 5: Soleus, 6: Achilles tendon [59]	41
6.2	Left: Home-built ergometer with mechanical system used in first institute. Right: Ergospect ergometer with pneumatic system used in second institute.	43
6.3	Exercise protocol in multicenter study at second institute: Three dynamic measurements with plantar flexion exercise, spaced by 10 and 15 minutes of physical inactivity. (ex = exercise, rec = recovery, b = break)	44
6.4	Non-localized region of interest of $^{31}\text{P}/^1\text{H}$ coil (white), 20 mm wide DRESS selection slab (yellow) (left picture) and semi-LASER localization (right picture) in the gastrocnemius medialis muscle (subject #1 from DRESS/semi-LASER/non-local study). Size of the single voxel can slightly vary between subjects depending on the muscle mass. The green box depicts the adjustment volume for shimming.	46
7.1	Time courses of the PCr signal intensity. The data are normalized to resting PCr signal intensity. The exercise period (6 min) is indicated in gray. Upper picture: PCr signal intensity measured with different workloads at 3T and second institute at the same subject #10. Lower picture: PCr signal intensity measured with 3T at both institutes and 7T in second institute with low workload at the same subject #11. . .	54

7.2	Sensitivity map evaluation of both coils used in the same subject (#4). Upper pictures: 11 cm flexi coil (first institute). Lower pictures: 10 cm rigid coil (second institute). Left: ^1H image with manually drawn mask (red: gastrocnemius medialis, yellow: gastrocnemius lateralis, blue: soleus). Right: Signal intensity map of the PCr signal calculated from the acquired 2D ^{31}P CSI.	57
7.3	γ -ATP curve: The blue line shows the γ -ATP curve with 1 Hz constrained linewidth, the green line shows the γ -ATP curve with non-constrained linewidth. Time between spectra is TR = 2 s. Upper picture: Data from subject #8, first institute, 3T, low workload, first measurement. Lower picture: Data from subject #5, second institute, 3T, mild workload.	58
7.4	Stack plot of the ^{31}P spectra acquired during rest, exercise and subsequent recovery for the non-localized (upper picture) and DRESS-localized acquisition (lower picture). The spectra are scaled equally to show the lower signal intensity of the localized experiment. Note the Pi split in the non-localized data. [58]	60
7.5	Time courses of the PCr and Pi signal intensity measured with DRESS-localization (upper picture) and without localization (lower picture) to the gastrocnemius medialis from the same subject #9. The data are normalized to resting PCr signal intensity. The exercise period (6 min) is indicated in gray. The Pi ₂ , not found in the DRESS-localized data, becomes distinguishable first after 1-3 minutes of active exercise. The sum of the two fitted Pi peaks is also depicted.	61
7.6	Time courses of the PCr signal intensity measured without, DRESS and semi-LASER localization to the gastrocnemius medialis from the same subject #5. The data are normalized to resting PCr signal intensity. The exercise period (6 min) is indicated in gray.	63

List of Tables

6.1	Calculated flip angle for different T_1 relaxation times according to [22]: Flip angle according to the relaxation time T_1 of the metabolites PCr, Pi and γ -ATP, the mean value of PCr and Pi as well as PCr, Pi and γ -ATP and the mean value of the most prominent metabolites in the muscle (phosphomonoesters (PME), Pi, phosphodi-esters (PDE), PCr, α -ATP, β -ATP and γ -ATP).	45
6.2	Parameters (flip angle FA, repetition time TR, spin-lattice relaxation T_1 , spin-spin relaxation T_2 according to [22] and acquisition delay time TE^* /echo time TE) used in the formula of the correction factor. Study 1 = Multicenter study, study 2 = nonloc/DRESS, study 3 = DRESS/semiLASER/nonloc.	48
7.1	Dynamic parameters measured in two institutes at 3T using mechanical and pneu-matic ergometer. The data are given mean \pm standard deviation. Concentration of PCr measured at end of recovery (last 40 seconds). endex = end of exercise (last 40 seconds); *) $p < 0.05$	51
7.2	Dynamic parameters measured in second institute using different magnetic field strenghts. The data are given mean \pm standard deviation. Concentration of PCr measured at end of recovery (last 40 seconds). endex = end of exercise (last 40 seconds); *) $p < 0.05$	52
7.3	FWHM of PCr and Pi in Hz at rest (mean of 1 minute), at end of exercise (last minute), immediately after exercise (mean of 20 seconds) and at end of recovery (last minute).	53
7.4	Temporal and static SNR at end of recovery (last 4 minutes) and at end of exercise (last 2 minutes), goodness of fit (r-square of tau-fitted curve to original data in per-centage), Cramér-Rao lower bounds of PCr and Pi in percentage and age-dependent concentration of PDE. The data are given as mean \pm standard deviation. *) = age 20-30 (mean 25.6) **) = age > 30 (mean 47.3)	55
7.5	Size of manually selected muscle regions in cm^2 (total image size: $324 cm^2$ in the first three data sets of the first institute, $400 cm^2$ in the last two data sets of the first institute and in all data sets in the second institute).	56
7.6	Coil sensitivity maps evaluation: Muscle signal/total signal.	56

7.7	The comparison of the dynamic parameters in non-localized and DRESS-localized experiments: Concentration of PCr measured at end of recovery (last 40 seconds). Both pH values at end of exercise (last 40 seconds) are given for the non-localized experiment; the nonacidifying pH ₁ (n = 14) and the acidifying pH ₂ (n = 6); pH ₁ is used in the t-test comparison depicted in the last column. The data are given as mean ± standard deviation.	59
7.8	Temporal and static SNR at end of recovery (last 4 minutes) and at end of exercise (last 2 minutes), goodness of fit (r-square of tau-fitted curve to original data in percentage) and Cramér-Rao lower bounds of PCr and Pi in percentage. The data are given as mean ± standard deviation.	62
7.9	FWHM of PCr and Pi in Hz at rest (mean of 1 minute), at end of exercise (last minute), immediately after exercise (mean of 20 seconds) and at end of recovery (last minute).	62
7.10	The comparison of the dynamic parameters in non-localized, DRESS and semi-LASER-localized experiments. Mean pH value measured at the end of exercise (last 40 seconds). The data are given as mean ± standard deviation.	63
7.11	FWHM of PCr and Pi in Hz at rest (mean of 1 minute), at end of exercise (last minute), immediately after exercise (mean of 20 seconds) and at end of recovery (last minute).	64
7.12	Temporal and static SNR at end of exercise (last 2 minutes) and at end of recovery (last 4 minutes), goodness of fit (r-square of tau-fitted curve to original data in percentage) and Cramér-Rao lower bounds of PCr and Pi in percentage. The data are given as mean ± standard deviation.	64
A.1	Physical characteristics of the subjects participating in the multicenter study.	91
A.2	Calculated PCr drop in percentage.	92
A.3	In Curve Fitting Toolbox evaluated τ in seconds.	93
A.4	Calculated mean pH value at end of exercise (last 40 seconds).	94
A.5	Calculated initial rate of PCr synthesis V_{PCr} in mM/s.	95
A.6	Calculated maximum rate of oxidative ATP synthesis Q_{max} in mM/s.	96
A.7	Calculated concentration of PCr at end of recovery (last 40 seconds) in mM.	97
A.8	Temporal SNR at end of exercise (last 2 minutes).	98
A.9	Temporal SNR at end of recovery (last 4 minutes).	98
A.10	Static SNR at end of exercise (last 2 minutes).	99
A.11	Static SNR at end of recovery (last 4 minutes).	99
A.12	Goodness of fit: R-square of tau-fitted curve to original data in percentage.	100
A.13	Cramér-Rao lower bounds of PCr and Pi peak in percentage, age and concentration of muscular phosphodiesterases (PDE) of all subjects. Subject #1 performed the exercises in two measurement bouts, therefore static spectrum was done twice. *) = age 20-30 (mean 25.6), **) = age > 30 (mean 47.3)	101
A.14	Linewidth of PCr in Hz at rest (mean of 1 minute), at end of exercise (last minute), immediately after exercise (mean of 20 seconds) and at end of recovery (last minute) at 3T, first institute. Subject #6 and #8 performed the exercises twice.	102

A.15	Linewidth of PCr in Hz at rest (mean of 1 minute), at end of exercise (last minute), immediately after exercise (mean of 20 seconds) and at end of recovery (last minute) at 3T, second institute.	102
A.16	Linewidth of PCr in Hz at rest (mean of 1 minute), at end of exercise (last minute), immediately after exercise (mean of 20 seconds) and at end of recovery (last minute) at 7T, second institute.	103
A.17	Linewidth of Pi in Hz at rest (mean of 1 minute), at end of exercise (last minute), immediately after exercise (mean of 20 seconds) and at end of recovery (last minute) at 3T, first institute. Subject #6 and #8 performed the exercises twice.	103
A.18	Linewidth of Pi in Hz at rest (mean of 1 minute), at end of exercise (last minute), immediately after exercise (mean of 20 seconds) and at end of recovery (last minute) at 3T, second institute.	104
A.19	Linewidth of Pi in Hz at rest (mean of 1 minute), at end of exercise (last minute), immediately after exercise (mean of 20 seconds) and at end of recovery (last minute) at 7T, second institute.	104
B.1	Physical characteristics of the subjects participating in the non-localized vs. DRESS localized study. The shown pressure indicates the set pressure at the commercial, pneumatic ergometer calculated from the desired force.	105
B.2	Dynamic parameters in non-localized and DRESS-localized experiments: Concentration of PCr measured at end of recovery (last 40 seconds). pH at end of exercise (last 40 seconds) is splitted in pH ₁ and pH ₂ in the non-localized data. Last column depicts student's T-test between non-localized and localized data.	106
B.3	Temporal and static SNR at end of exercise (endex, last 2 minutes) and at end of recovery (endrec = last 4 minutes), goodness of fit (r-square of tau-fitted curve to original data in percentage) and Cramér-Rao lower bounds of PCr and Pi in percentage.	107
B.4	Linewidth of PCr and Pi in Hz at rest (mean of 1 minute), at end of exercise (last minute), immediately after exercise (mean of 20 seconds) and at end of recovery (last minute).	108
C.1	Physical characteristics of the subjects participating in the DRESS vs. semi-LASER vs. non-localized study.	109
C.2	Single voxel size and set TE in the semi-LASER localization.	109
C.3	Dynamic parameters in non-localized, DRESS- and semi-LASER-localized experiments: pH value measured at the end of exercise (last 40 seconds). Last three column depicts student's T-test.	110
C.4	FWHM of PCr and Pi in Hz at rest (mean of 1 minute), at end of exercise (last minute), immediately after exercise (mean of 20 seconds) and at end of recovery (last minute).	111
C.5	Temporal static SNR at end of exercise (last 2 minutes) and end of recovery (last 4 minutes) and goodness of fit (r-square of fitted curve to original data in percentage).	112
C.6	Cramér-Rao lower bounds in percentage. There was no detection of Pi peak for semi-LASER data of subject #1 possible.	112

Detailed results - Multicenter Study

	Gender	Age	Height [cm]	Weight [kg]	BMI [kg/m ²]
1	m	66	183	85	25.4
2	f	43	155	50	20.8
3	f	27	162	55	21.0
4	m	25	173	74	24.7
5	m	25	190	90	24.9
6	m	27	196	75	19.5
7	m	44	188	102	28.9
8	m	33	177	74	23.6
9	m	46	170	65	22.5
10	m	33	180	80	24.7
11	f	24	171	67	22.9
mean± std		36±12	177±12	74±14	23.5±2.5

Table A.1: Physical characteristics of the subjects participating in the multicenter study.

	low			mild			heavy	
	3T 1 st inst.	3T 2 st inst.	7T 2 st inst.	3T 1 st inst.	3T 2 st inst.	7T 2 st inst.	3T 2 st inst.	7T 2 st inst.
1	13.64	9.57	12.99	23.79	15.42	13.85	23.98	20.48
2	50.50	19.56	15.95	56.38	37.34	18.56	24.52	
3	13.32	17.12	16.26	22.34	34.76	35.00	49.90	44.20
4	5.74	6.11	9.00	11.58	10.46	18.13	20.23	20.55
5	9.68	6.88	6.13	21.07	8.10	13.00	13.94	8.92
6	24.23	11.49	16.63	42.59	27.97	20.56		
7	7.24	5.97	6.74		10.22	6.69		
8	38.77	17.00	13.45	54.23	24.87	26.22	34.81	31.33
9	11.05	12.86	13.37	20.86	19.18	22.00	19.15	24.03
10	18.50	14.68	14.11	31.01	33.49	31.27	54.58	
11	31.48	11.79	10.64	45.42	22.49	24.28	39.92	47.17
mean	20.38	12.09	12.30	32.93	22.21	20.87	31.23	28.10
std	13.72	4.47	3.52	14.81	9.96	7.83	13.52	12.72
T-Test 3T-3T	0.04			0.04				
T-Test 3T-7T	0.81			0.55			0.71	

Table A.2: Calculated PCr drop in percentage.

	low			mild			heavy	
	3T 1 st inst.	3T 2 st inst.	7T 2 st inst.	3T 1 st inst.	3T 2 st inst.	7T 2 st inst.	3T 2 st inst.	7T 2 st inst.
1	48.26	37.25	42.25	60.38	37.63	37.65	38.79	38.30
2	46.39	38.13	35.47	41.29	31.00	33.83	33.70	
3	22.45	24.34	32.74	30.91	41.60	42.47	43.77	40.36
4	41.04	25.44	29.61	38.87	25.88	35.04	22.34	25.58
5	34.55	17.66	24.58	41.84	26.43	21.28	17.75	19.22
6	30.91	33.70	27.53	47.16	34.25	43.90		
7	30.43	26.41	32.19		20.31	20.84		
8	42.41	35.42	32.59	54.75	32.16	33.74	35.21	34.52
9	26.32	36.87	42.63	28.73	20.48	21.45	12.53	24.63
10	26.13	26.05	33.53	31.56	28.50	30.72	39.95	
11	27.07	34.33	33.96	35.60	36.84	27.59	37.39	33.99
mean	34.18	30.51	33.37	41.11	30.46	31.68	31.27	30.94
std	8.54	6.46	5.20	9.89	6.59	7.80	10.33	7.28
T-Test 3T-3T	0.21			0.02				
T-Test 3T-7T	0.08			0.47			0.56	

Table A.3: In Curve Fitting Toolbox evaluated τ in seconds.

	low			mild			heavy	
	3T 1 st inst.	3T 2 st inst.	7T 2 st inst.	3T 1 st inst.	3T 2 st inst.	7T 2 st inst.	3T 2 st inst.	7T 2 st inst.
1	7.04	7.10	7.07	7.05	7.04	7.06	7.05	7.08
2	6.98	7.11	7.08	6.99	7.08	7.07	7.05	
3	7.01	7.07	7.07	7.04	6.97	7.10	7.01	7.07
4	7.08	7.08	7.09	7.07	7.08	7.07	7.08	7.08
5	7.06	7.08	7.06	7.06	7.07	7.07	7.08	7.04
6	7.06	7.08	7.04	7.05	6.99	7.11		
7	7.09	7.09	7.09		7.09	7.07		
8	7.09	7.09	7.06	7.08	7.07	7.01	7.03	7.01
9	7.07	7.05	7.07	7.06	7.06	7.07	7.07	7.05
10	7.02	7.13	7.08	6.95	7.07	7.03	6.98	
11	7.04	7.10	7.05	7.04	7.07	7.04	7.05	7.03
mean	7.05	7.09	7.07	7.04	7.06	7.06	7.04	7.05
std	0.03	0.02	0.01	0.04	0.04	0.03	0.03	0.02
T-Test 3T-3T	0.02			0.52				
T-Test 3T-7T	0.01			0.65			0.92	

Table A.4: Calculated mean pH value at end of exercise (last 40 seconds).

	low			mild			heavy	
	3T 1 st inst.	3T 2 st inst.	7T 2 st inst.	3T 1 st inst.	3T 2 st inst.	7T 2 st inst.	3T 2 st inst.	7T 2 st inst.
1	0.11	0.09	0.10	0.15	0.15	0.12	0.21	0.17
2	0.38	0.19	0.16	0.55	0.41	0.19	0.27	
3	0.20	0.21	0.16	0.24	0.25	0.27	0.35	0.36
4	0.05	0.078	0.11	0.11	0.13	0.16	0.29	0.24
5	0.09	0.10	0.08	0.16	0.08	0.19	0.22	0.14
6	0.29	0.11	0.20	0.37	0.28	0.18		
7	0.07	0.08	0.06		0.17	0.09		
8	0.32	0.15	0.12	0.33	0.26	0.21	0.31	0.26
9	0.16	0.12	0.11	0.28	0.33	0.36	0.43	0.33
10	0.30	0.22	0.17	0.40	0.45	0.40	0.51	
11	0.43	0.11	0.11	0.47	0.19	0.31	0.36	0.48
mean	0.22	0.13	0.13	0.31	0.24	0.23	0.33	0.28
std	0.13	0.05	0.04	0.14	0.11	0.09	0.09	0.11
T-Test 3T-3T	0.03			0.02				
T-Test 3T-7T	0.49			0.55			0.38	

Table A.5: Calculated initial rate of PCr synthesis V_{PCr} in mM/s.

	low			mild			heavy	
	3T 1 st inst.	3T 2 st inst.	7T 2 st inst.	3T 1 st inst.	3T 2 st inst.	7T 2 st inst.	3T 2 st inst.	7T 2 st inst.
1	0.28	0.20	0.26	0.31	0.34	0.30	0.41	0.36
2	0.56	0.38	0.36	0.75	0.63	0.42	0.53	
3	0.67	0.48	0.39	0.52	0.45	0.42	0.50	0.54
4	0.20	0.22	0.26	0.33	0.33	0.36	0.62	0.49
5	0.24	0.29	0.24	0.33	0.23	0.46	0.53	0.40
6	0.58	0.29	0.49	0.56	0.54	0.40		
7	0.21	0.25	0.18		0.46	0.31		
8	0.47	0.32	0.28	0.42	0.48	0.43	0.54	0.47
9	0.44	0.30	0.25	0.62	0.72	0.84	0.80	0.64
10	0.66	0.49	0.41	0.80	0.75	0.72	0.71	
11	0.74	0.26	0.29	0.69	0.37	0.64	0.56	0.71
mean	0.46	0.32	0.31	0.53	0.48	0.48	0.58	0.52
std	0.19	0.09	0.09	0.17	0.16	0.17	0.11	0.11
T-Test 3T-3T	0.01			0.23				
T-Test 3T-7T	0.85			0.96			0.27	

Table A.6: Calculated maximum rate of oxidative ATP synthesis Q_{\max} in mM/s.

	low			mild			heavy	
	3T 1 st inst.	3T 2 st inst.	7T 2 st inst.	3T 1 st inst.	3T 2 st inst.	7T 2 st inst.	3T 2 st inst.	7T 2 st inst.
1	38.57	36.33	33.66	39.00	36.19	33.88	34.67	32.26
2	34.72	37.02	35.75	39.97	34.23	34.95	36.64	
3	33.93	30.50	32.66	32.79	29.42	32.39	30.77	33.25
4	35.75	32.25	34.55	37.73	31.08	30.46	32.19	29.78
5	31.29	26.08	31.27	31.80	26.79	31.24	28.21	30.71
6	37.27	33.61	33.43	38.79	33.78	38.3		
7	31.49	35.05	28.34		34.45	28.52		
8	33.97	30.64	28.24	32.87	33.09	27.65	31.71	28.18
9	37.72	33.97	34.36	38.12	35.20	35.56	27.85	33.67
10	41.84	39.78	41.17	41.19	38.40	39.08	37.68	
11	37.99	32.87	35.06	37.19	30.49	34.67	33.43	34.66
mean	35.78	33.46	33.50	36.94	33.01	33.38	32.57	31.79
std	2.99	3.52	3.41	3.12	3.16	3.58	3.22	2.15
T-Test 3T-3T	0.02			0.00				
T-Test 3T-7T	0.97			0.75			0.69	

Table A.7: Calculated concentration of PCr at end of recovery (last 40 seconds) in mM.

	3T 1 st institute		3T 2 nd institute			7T 2 nd institute		
	low	mild	low	mild	heavy	low	mild	heavy
1	11	9	22	29	19	42	83	21
2	21	17	16	12	41	99	92	
3	22	13	30	26	15	118	38	66
4	24	30	44	38	28	84	41	53
5	39	22	36	39	31	130	72	131
6	24	20	42	44		62	65	
7	55		49	33		58	64	
8	9	10	30	34	23	114	36	56
9	34	37	38	29	18	114	42	74
10	49	35	27	22	20	94	75	
11	35	31	27	22	24	141	62	35
mean±std	29±14	22±10	33±10	30±9	24±7	96±30	61±18	62±33

Table A.8: Temporal SNR at end of exercise (last 2 minutes).

	3T 1 st institute		3T 2 nd institute			7T 2 nd institute		
	low	mild	low	mild	heavy	low	mild	heavy
1	47	41	40	34	37	99	122	105
2	42	47	24	18	46	123	144	
3	36	32	35	29	27	112	44	82
4	24	46	44	42	70	110	135	96
5	33	26	36	46	42	150	146	160
6	76	45	51	46		95	82	
7	52		58	34		68	125	
8	46	26	33	35	36	99	114	128
9	74	69	35	43	28	103	102	97
10	39	47	36	38	36	87	137	
11	52	62	31	27	32	133	137	98
mean±std	47±15	44±13	39±9	36±8	39±12	107±21	117±30	110±24

Table A.9: Temporal SNR at end of recovery (last 4 minutes).

	3T 1 st institute		3T 2 nd institute			7T 2 nd institute		
	low	mild	low	mild	heavy	low	mild	heavy
1	235	251	197	245	171	564	712	286
2	223	164	139	126	182	449	602	
3	279	193	210	176	111	497	499	418
4	326	265	307	246	266	499	522	491
5	320	249	266	245	199	699	556	636
6	299	276	322	268		573	553	
7	367		282	255		472	502	
8	219	141	271	165	152	568	524	361
9	378	298	215	188	181	557	509	431
10	285	263	238	232	123	663	522	
11	264	222	248	245	194	610	506	391
mean±std	290±52	232±49	245±50	218±44	175±43	559±74	546±60	431±102

Table A.10: Static SNR at end of exercise (last 2 minutes).

	3T 1 st institute		3T 2 nd institute			7T 2 nd institute		
	low	mild	low	mild	heavy	low	mild	heavy
1	316	376	245	228	244	691	639	733
2	326	364	175	172	270	659	581	
3	327	292	283	262	249	619	560	678
4	372	375	308	289	361	743	601	655
5	347	369	301	282	254	593	657	582
6	410	383	316	341		662	663	
7	369		337	280		591	534	
8	358	309	251	238	268	647	648	641
9	368	350	224	224	259	704	669	687
10	357	367	306	273	263	655	721	
11	356	332	263	298	303	773	652	704
mean±std	355±25	352±29	273±45	262±43	274±35	667±55	630±52	669±45

Table A.11: Static SNR at end of recovery (last 4 minutes).

	3T 1st institute		3T 2nd institute			7T 2nd institute		
	low	mild	low	mild	heavy	low	mild	heavy
1	54.3	73.5	33.3	61.3	87.1	91.3	96.0	95.3
2	98.4	98.4	51.7	78.4	88.5	97.8	97.7	
3	67.0	62.0	79.9	94.3	95.5	95.8	99.4	99.7
4	44.6	74.0	29.1	71.1	93.7	87.3	93.2	97.0
5	26.7	64.6	39.4	34.2	64.1	84.2	96.9	89.5
6	93.3	94.1	73.6	94.4		90.8	95.6	
7	65.9		45.1	36.5		44.0	74.2	
8	90.1	89.8	74.2	88.4	92.8	92.3	99.1	99.4
9	90.0	94.1	60.3	29.1	45.4	92.2	95.8	97.3
10	83.9	94.9	77.3	87.9	97.7	89.1	99.3	
11	94.1	96.3	33.0	87.2	92.2	90.6	98.8	99.3
mean	73.5	84.2	52.3	69.3	84.1	86.8	95.1	96.8
std	23.6	14.1	19.6	25.2	17.6	14.7	7.2	3.6

Table A.12: Goodness of fit: R-square of tau-fitted curve to original data in percentage.

	Age	CRLB						concentration		
		PCr			Pi			PDE		
		3T 1 st inst.	3T 2 nd inst.	7T 2 nd inst.	3T 1 st inst.	3T 2 nd inst.	7T 2 nd inst.	3T 1 st inst.	3T 2 nd inst.	7T 2 nd inst.
1(1)	66	0.99	1.44	1.26	13.23	15.30	18.76	4.47	4.18	3.55
1(2)	66		1.30	1.03		16.58	16.86		4.22	3.06
2	43	1.14	1.44	1.20	15.14	18.26	19.30	2.82	3.44	2.60
3	27	1.75	1.43	0.99	20.42	13.90	14.73	9.38	2.42	1.52
4	25	1.11	1.19	1.02	13.61	13.12	15.01	3.34	3.00	2.41
5	25	1.71	1.65	0.89	24.81	14.65	13.54	2.10	2.85	1.92
6	27		1.16	1.40		15.52	18.54		3.11	1.94
7	44		1.33	1.56		15.64	26.32		4.42	3.40
8	33		1.17	1.15		16.20	10.85		3.57	2.99
9	46	1.04	1.05	1.15	10.64	9.94	12.91	1.89	2.46	0.90
10	33	0.85	1.27	1.30	11.93	16.69	18.15	3.44	4.27	2.33
11	24		1.32	0.97		16.08	16.78		8.91	1.52
mean		1.07	1.22	1.06	13.72	13.92	15.44			
std		0.59	0.38	0.44	7.74	5.63	6.86			
mean*								1.36	2.84	1.86
mean**								1.80	3.80	2.69

Table A.13: Cramér-Rao lower bounds of PCr and Pi peak in percentage, age and concentration of muscular phosphodiester (PDE) of all subjects. Subject #1 performed the exercises in two measurement bouts, therefore static spectrum was done twice. *) = age 20-30 (mean 25.6), **) = age > 30 (mean 47.3)

	Workload	Rest	Endexercise	Postexercise	Endrecovery
1	low	4.7	5.1	4.8	4.4
2	low	5.8	5.2	5.5	5.7
3	low	8.1	15.9	10.7	10.6
3	mild	9.4	18.1	12.6	12.0
4	mild	5.4	5.5	5.6	10.7
4	mild	4.9	5.9	8.9	8.7
5	mild	8.6	9.4	9.7	9.3
6(2)	mild	4.4	6.8	6.5	4.3
7	low	4.2	4.1	4.2	4.2
8(1)	low	4.3	9.9	4.8	4.4
8(1)	mild	5.1	8.6	5.7	5.4
8(2)	low	4.3	6.8	6.1	5.2
8(2)	mild	4.6	9.0	9.7	7.0
mean±std		5.7±1.8	8.5±4.2	7.3±2.7	7.1±2.8

Table A.14: Linewidth of PCr in Hz at rest (mean of 1 minute), at end of exercise (last minute), immediately after exercise (mean of 20 seconds) and at end of recovery (last minute) at 3T, first institute. Subject #6 and #8 performed the exercises twice.

	Workload	Rest	Endexercise	Postexercise	Endrecovery
2	low	8.6	9.6	9.2	9.3
2	mild	10.0	10.7	9.9	9.4
3	heavy	9.6	10.5	10.0	9.7
10	low	9.9	10.3	10.1	10.0
10	mild	10.0	10.3	10.4	9.8
10	heavy	10.1	11.3	11.2	9.9
11	low	8.5	8.9	8.7	8.3
11	mild	8.6	9.5	9.3	8.3
11	heavy	8.3	9.0	8.9	8.3
mean±std		9.3±0.8	10.0±0.8	9.7±0.8	9.2±0.7

Table A.15: Linewidth of PCr in Hz at rest (mean of 1 minute), at end of exercise (last minute), immediately after exercise (mean of 20 seconds) and at end of recovery (last minute) at 3T, second institute.

	Workload	Rest	Endexercise	Postexercise	Endrecovery
3	heavy	8.9	11.5	11.5	11.0
4	mild	9.2	11.5	11.5	11.5
4	heavy	11.9	13.0	13.0	12.8
6	mild	15.9	18.8	17.8	16.5
7	low	15.2	14.2	14.3	15.2
9	mild	12.0	13.5	13.2	14.0
10	low	17.1	18.8	18.0	17.8
11	mild	9.9	10.5	10.5	10.5
11	heavy	10.5	11.0	10.8	10.2
mean±std		12.3±3.1	13.6±3.2	13.4±2.8	13.3±2.8

Table A.16: Linewidth of PCr in Hz at rest (mean of 1 minute), at end of exercise (last minute), immediately after exercise (mean of 20 seconds) and at end of recovery (last minute) at 7T, second institute.

	Workload	Rest	Endexercise	Postexercise	Endrecovery
1	low	6.5	7.7	6.0	6.4
1	mild	8.0	8.0	7.7	7.9
2	low	10.3	14.2	12.7	9.6
2	mild	8.2	12.7	11.9	8.4
3	low	14.0	20.0	18.9	14.7
3	mild	16.8	20.6	17.3	18.1
4	low	9.3	9.3	9.6	9.9
4	mild	8.6	9.6	10.0	9.5
5	low	15.2	15.9	14.2	15.3
5	mild	12.3	14.0	13.9	12.2
6(1)	mild	12.3	11.4	12.9	12.5
6(2)	mild	7.2	9.9	10.0	7.9
8(1)	low	7.4	12.0	10.5	8.1
8(1)	mild	7.7	11.0	5.6	7.6
8(2)	low	6.8	8.9	8.2	7.7
8(2)	mild	8.6	14.5	13.9	12.2
11	mild	6.8	7.0	7.0	6.6
mean±std		9.8±3.2	12.2±4.0	11.2±3.8	10.3±3.4

Table A.17: Linewidth of Pi in Hz at rest (mean of 1 minute), at end of exercise (last minute), immediately after exercise (mean of 20 seconds) and at end of recovery (last minute) at 3T, first institute. Subject #6 and #8 performed the exercises twice.

	Workload	Rest	Endexercise	Postexercise	Endrecovery
3	heavy	10.9	11.4	11.4	11.0
9	heavy	13.2	9.5	9.7	11.2
10	low	14.6	13.8	13.4	14.4
10	heavy	14.4	20.0	20.0	17.1
11	mild	13.6	13.2	13.7	13.3
mean±std		13.3±1.5	13.6±3.9	13.6±3.9	13.4±2.5

Table A.18: Linewidth of Pi in Hz at rest (mean of 1 minute), at end of exercise (last minute), immediately after exercise (mean of 20 seconds) and at end of recovery (last minute) at 3T, second institute.

	Workload	Rest	Endexercise	Postexercise	Endrecovery
3	mild	14.3	15.6	15.8	14.7
3	heavy	11.9	12.0	12.0	12.0
4	mild	13.6	15.0	14.8	14.4
4	heavy	16.8	20.0	20.0	16.4
6	mild	15.7	16.0	15.7	15.5
7	low	27.2	30.0	27.9	26.9
9	mild	18.0	21.7	20.4	19.4
10	mild	24.9	25.0	25.0	24.8
11	mild	17.0	17.0	17.0	16.9
11	heavy	15.0	17.0	17.0	15.3
mean±std		17.4±4.9	18.9±5.3	18.6±4.9	17.6±4.7

Table A.19: Linewidth of Pi in Hz at rest (mean of 1 minute), at end of exercise (last minute), immediately after exercise (mean of 20 seconds) and at end of recovery (last minute) at 7T, second institute.

Detailed results - Nonloc/DRESS Study

	Gender	Age	Height [cm]	Weight [kg]	BMI [kg/m ²]	Pressure [bar]	Force [N]
1	f	41	165	75	27.5	1.6	450
2	f	42	166	71	25.8	1.7	500
3	m	40	180	108	33.3	3.2	1000
4	m	30	176	90	29.1	3.2	1000
5	m	36	185	108	31.6	2.9	900
6	m	52	176	78	25.2	3.0	950
7	m	50	182	115	34.7	2.25	700
8	m	35	182	105	31.7	2.9	900
9	m	33	175	95	31.0	2.75	860
10	m	40	183	116	34.6	2.75	860
11	f	43	158	78	31.2	2.4	750
12	m	48	178	92	29.0	2.75	800
13	m	47	183	88	26.3	1.9	600
14	f	48	162	107	40.8	1.7	500
mean±std		42±6	175±8	95±15	30.8±4.1		

Table B.1: Physical characteristics of the subjects participating in the non-localized vs. DRESS localized study. The shown pressure indicates the set pressure at the commercial, pneumatic ergometer calculated from the desired force.

	PCr-drop [%]		τ [s]		pH endex			V_{PCr} [mM/s]		Q_{max} [mM/s]		conc_PCcr endrec [mM]	
	non-loc	DRESS	non-loc	DRESS	Pi ₁	Pi ₂	DRESS	non-loc	DRESS	non	DRESS	non-loc	DRESS
1	26.15	31.23	46.35	30.34	7.02	6.82	7.03	0.20	0.38	0.38	0.68	34.72	36.75
2	12.73	30.90	20.51	34.79	7.06		7.04	0.20	0.23	0.50	0.39	32.73	26.10
3	39.69	45.23	55.69	53.30	7.05		6.94	0.25	0.34	0.40	0.56	35.33	39.84
4	60.09	67.94	66.09	74.85	7.04	6.56	6.94	0.33	0.39	0.42	0.49	36.42	42.61
5	43.26	24.04	52.78	56.13	7.00	6.70	7.11	0.31	0.16	0.47	0.29	37.82	38.06
6	36.72	69.65	37.09	35.72	7.05		6.91	0.31	0.65	0.50	0.79	31.78	33.18
7	18.47	32.70	30.64	49.72	7.05		7.00	0.21	0.23	0.49	0.41	34.93	34.93
8	30.49	81.73	38.83	78.69	7.06	6.82	6.69	0.29	0.42	0.49	0.51	36.49	40.49
9	42.06	64.77	83.65	79.46	6.98		6.70	0.18	0.32	0.27	0.48	35.11	39.67
10	24.07	28.72	46.90	28.03	7.02		7.06	0.18	0.36	0.36	0.64	34.24	34.79
11	39.37	59.77	31.84	34.22	7.03	6.76	6.97	0.41	0.71	0.65	0.96	33.53	40.85
12	44.96	81.41	56.25	55.76	7.06	6.70	6.92	0.32	0.68	0.48	0.78	40.11	46.71
13	23.19	30.47	47.65	40.71	7.05		7.01	0.32	0.24	0.30	0.45	30.50	31.77
14	25.09	25.70	28.14	30.15	6.97		7.07	0.15	0.25	0.68	46	35.56	29.54
mean	34.89	49.49	47.84	49.78	7.03	6.73	6.95	0.27	0.39	0.45	0.58	35.12	37.63
std	11.16	21.09	14.97	17.96	0.03	0.09	0.012	0.08	0.17	0.12	0.18	2.35	4.56
T-Test	0.01		0.49		0.06			0.01		0.05		0.12	

Table B.2: Dynamic parameters in non-localized and DRESS-localized experiments: Concentration of PCr measured at end of recovery (last 40 seconds). pH at end of exercise (last 40 seconds) is splitted in pH₁ and pH₂ in the non-localized data. Last column depicts student's T-test between non-localized and localized data.

	Temporal SNR				Static SNR				R-square		CRLB	
	endex		endrec		endex		endrec		non-loc	DRESS	PCr	Pi
	non-loc	DRESS	non-loc	DRESS	non-loc	DRESS	non-loc	DRESS				
1	40	28	82	42	442	332	689	370	96.0	90.6	1.09	12.24
2	36	17	47	31	545	193	583	278	92.2	69.2	1.00	12.15
3	34	31	54	39	415	263	677	386	98.4	98.4	1.37	17.26
4	20	10	31	19	252	154	542	350	98.4	98.4	1.83	22.10
5	29	24	72	35	428	224	693	35	98.8	90.6	1.57	20.32
6	34	6	48	19		422	49	534	213 95.0	87.5	1.39	14.74
7	53	12	90	15	563	145	562	203	90.7	73.8	1.13	13.80
8	33	7	124	16	563	58	726	289	95.9	98.4	1.23	18.03
9	28	14	30	16	394	140	567	270	98.6	97.0	1.54	18.14
10	46	20	78	37	458	225	618	321	93.0	87.0	1.24	17.06
11	47	16	91	40	370	118	681	340	99.1	97.7	1.04	15.95
12	39	7	44	30	275	74	548	336	97.5	98.5	1.14	13.24
13	73	24	79	35	554	256	662	307	95.1	91.9	1.22	14.76
14	26	19	47	35	399	176	538	321	70.5	82.5	1.55	23.11
mean	38	17	66	29	434	172	616	287	94.3	90.1	1.32	16.57
std	13	8	27	10	99	83	69	90	7.4	9.5	0.23	3.50

Table B.3: Temporal and static SNR at end of exercise (endex, last 2 minutes) and at end of recovery (endrec = last 4 minutes), goodness of fit (r-square of tau-fitted curve to original data in percentage) and Cramér-Rao lower bounds of PCr and Pi in percentage.

		DRESS				Non-Localized			
		Rest	Endexercise	Postexercise	Endrecovery	Rest	Endexercise	Postexercise	Endrecovery
PCr	1	11.8	13.8	13.3	12.9	(1 Hz constrained linewidth)			
	2	7.9	8.0	8.3	9.3	11.8	20.4	16.2	12.7
	3	(1 Hz constrained linewidth)				14.2	15.0	15.0	14.1
	4	26.0	27.9	27.8	27.5	21.3	15.0	15.9	18.0
	5	11.7	12.7	12.5	11.7	17.3	16.6	16.8	16.1
	6	11.7	14.5	14.1	13.6	20.7	23.0	22.7	20.6
	7	14.4	14.8	15.1	14.1	15.3	14.7	14.8	14.5
	8	13.4	14.0	14.3	13.7	(1 Hz constrained linewidth)			
	9	18.9	18.8	19.0	18.4	19.2	14.0	14.1	15.1
	10	10.6	11.7	11.9	10.9	13.0	13.9	13.6	12.8
	12	13.0	12.7	13.7	13.6	14.7	18.5	16.6	16.4
	13	11.7	11.1	11.1	12.0	(1 Hz constrained linewidth)			
	14	7.7	9.3	8.6	7.5	17.5	24.0	22.7	17.4
		mean	13.2	14.1	14.1	13.8	16.5	17.5	16.8
	std	5.0	5.2	5.2	5.1	3.2	3.8	3.3	2.5
Pi	1	18.2	19.9	20.0	18.6	14.5	19.8	19.9	15.8
	2	19.8	12.7	18.6	18.8	20.0	20.0	20.0	20.0
	3	24.0	30.0	30.0	26.4	26.1	28.0	28.0	27.7
	4	24.8	35.0	35.0	26.9	28.6	41.3	34.4	26.7
	5	14.9	17.8	19.1	16.1	22.8	30.0	30.0	23.5
	6	30.0	67.1	69.4	45.9	31.0	33.0	33.0	31.7
	7	22.7	23.5	25.0	23.6	20.2	18.8	19.6	19.2
	8	26.2	58.6	60.0	35.5	17.3	19.7	20.0	18.2
	9	32.4	46.3	42.2	46.5	23.2	30.0	30.0	17.8
	10	27.5	17.3	19.1	32.4	21.1	25.0	25.0	22.0
	12	19.4	30.0	29.9	21.4	19.9	34.9	27.2	19.6
	13	21.5	25.0	25.0	23.6	23.3	23.9	22.4	22.9
	14	21.1	15.2	18.9	25.9	26.1	34.6	35.0	32.4
		mean	23.3	30.6	31.7	27.8	22.6	27.6	26.5
	std	4.9	17.0	16.4	9.8	4.5	7.1	5.8	5.3

Table B.4: Linewidth of PCr and Pi in Hz at rest (mean of 1 minute), at end of exercise (last minute), immediately after exercise (mean of 20 seconds) and at end of recovery (last minute).

Detailed results - DRESS/semi-LASER/nonloc Study

	Gender	Age	Height [cm]	Weight [kg]	BMI [kg/m ²]
1	m	24	190	90	24.9
2	m	27	196	75	19.5
3	m	28	185	76	22.2
4	m	26	172	76	25.7
5	m	27	180	66	20.4
mean±std		27±1	187±9	76±7	22.0±2.5

Table C.1: Physical characteristics of the subjects participating in the DRESS vs. semi-LASER vs. non-localized study.

	Length [cm]	Width [cm]	Height [cm]	Volume [cm ³]	TE [ms]
1	4.0	1.8	5.0	36.0	23
2	3.6	1.8	4.8	31.1	23
3	4.5	1.8	5.8	47.0	25
4	4.0	1.8	5.0	36.0	25
5	3.4	1.6	5.8	31.6	24
mean	3.9	1.8	5.3	36.3	24

Table C.2: Single voxel size and set TE in the semi-LASER localization.

	PCr-drop [%]			τ [s]			pH endex		
	non-loc	DRESS	sLASER	non-loc	DRESS	sLASER	non-loc	DRESS	sLASER
1	21.58	34.70	32.91	38.36	33.70	36.37	7.08	7.02	7.08
2	28.10	34.37	25.92	31.19	36.30	38.29	7.06	6.98	6.99
3		17.34	26.50		29.71	30.31		7.02	7.05
4	34.19	69.28	55.39	55.51	70.55	53.97	7.00	6.62	6.95
5	41.06	63.32	71.73	55.65	54.48	45.62	7.06	6.95	6.95
mean	31.23	43.80	43.47	45.18	44.95	40.91	7.05	6.92	7.00
std	8.33	18.29	21.81	12.36	17.17	9.12	0.04	0.17	0.06
DRESS-sLASER	0.79			0.34			0.23		
DRESS-nonloc	0.05			0.47			0.13		
sLASER-nonloc	0.12			0.68			0.08		

Table C.3: Dynamic parameters in non-localized, DRESS- and semi-LASER-localized experiments: pH value measured at the end of exercise (last 40 seconds). Last three column depicts student's T-test.

		PCr				Pi			
		Rest	Endexercise	Postexercise	Endrecovery	Rest	Endexercise	Postexercise	Endrecovery
non-loc	1	14.3	14.7	14.4	13.8	28.7	22.2	23.5	27.2
	2	12.1	18.1	17.6	18.2	23.4	23.4	23.5	23.8
	4	11.5	14.8	13.3	11.1	25.6	49.1	50.0	23.5
	5	12.6	13.2	12.6	13.1	21.4	29.2	29.5	21.1
	mean	13.9	15.2	14.5	14.1	24.8	31.0	31.6	23.9
	std	2.4	2.1	2.2	3.0	3.1	12.5	12.6	2.5
DRESS	1	17.8	16.0	15.8	15.1	20.9	20.2	20.6	22.7
	2	13.6	14.0	13.6	12.0	25.8	29.2	29.7	25.3
	3	15.8	14.7	14.7	14.8	21.9	21.9	22.6	19.3
	4	10.6	11.5	10.8	9.6	35.6	66.5	60.6	49.7
	5	20.1	18.0	18.0	18.0	34.8	56.6	60.0	43.2
	mean	15.6	14.8	14.6	13.9	27.8	38.9	38.7	32.0
	std	3.7	2.4	2.7	3.2	7.0	21.3	20.0	13.5
sLASER	1	8.6	9.8	9.8	9.6	12.0	16.0	12.4	16.3
	2	6.5	9.5	8.6	7.3	13.3	24.7	27.0	19.7
	3	9.5	9.6	9.3	9.4	17.8	17.7	18.6	14.9
	4	8.7	6.8	7.0	8.5	17.9	39.3	41.9	24.4
	5	8.7	7.9	9.1	7.0	26.3	51.1	53.1	38.8
	mean	8.4	8.7	8.8	8.4	17.4	29.8	30.6	22.8
	std	1.1	1.3	1.1	1.2	5.6	15.1	16.8	9.6

Table C.4: FWHM of PCr and Pi in Hz at rest (mean of 1 minute), at end of exercise (last minute), immediately after exercise (mean of 20 seconds) and at end of recovery (last minute).

		1	2	3	4	5	mean±std
Temporal SNR at end of exercise	nonloc	60	54		27	58	50±15
	DRESS	15	24	25	5	14	17±8
	sLASER	8	15	20	16	5	13±6
Temporal SNR at end of recovery	nonloc	68	59		67	52	61±8
	DRESS	33	63	42	18	29	37±17
	sLASER	10	37	34	30	22	27±11
Static SNR at end of exercise	nonloc	434	460		457	421	443±19
	DRESS	189	274	264	99	112	187±82
	sLASER	84	272	397	153	65	194±139
Static SNR at end of exercise	nonloc	553	748		615	558	618±91
	DRESS	301	395	315	256	316	317±50
	sLASER	179	345	398	332	231	297±90
R-square	nonloc	90.9	86.7		98.9	98.2	93.7±5.9
	DRESS	89.9	96.5	63.6	98.0	97.8	89.1±14.7
	sLASER	43.4	85.9	71.7	94.9	94.4	78.1±21.5

Table C.5: Temporal static SNR at end of exercise (last 2 minutes) and end of recovery (last 4 minutes) and goodness of fit (r-square of fitted curve to original data in percentage).

	non-localized		DRESS-localized		semi-LASER	
	PCr	Pi	PCr	Pi	PCr	Pi
1	1.29	21.01	2.07	21.54	1.94	
2	1.35	18.88	1.50	28.17	0.84	18.11
3			1.85	23.64	0.78	11.99
4	1.09	23.00	1.43	21.85	0.73	33.45
5	1.15	19.62	2.74	32.91	1.28	23.81
mean±std	1.22±0.12	20.63±1.81	1.92±0.53	25.62±4.86	1.11±0.51	21.84±9.12

Table C.6: Cramér-Rao lower bounds in percentage. There was no detection of Pi peak for semi-LASER data of subject #1 possible.